

A *b*-baryon sonata

Habilitation à diriger des recherches de l'Université Paris-Saclay
présentée et soutenue à IJCLab, le 20 Mai 2020, par

Yasmine Sara Amhis

Composition du Jury :

Prof Tulika Bose

University of Wisconsin-Madison

Rapportrice

Prof Gino Isidori

University of Zürich

Examineur

Prof François Le Diberder

Université de Paris, IJCLab Orsay

Examineur

Prof Achille Stocchi

Université Paris-Saclay, IJCLab Orsay

Examineur

Prof Guy Wilkinson

University of Oxford

Rapporteur

Dr Isabelle Wingerter-Seez

Laboratoire d'Annecy de Physique des Particules

Rapportrice

Contents

Prélude	4
1 Allegro non troppo	5
1.1 A powerful yet incomplete theory	5
1.2 Handling multi-scale problems	7
1.3 What can we learn from mass measurements?	9
1.4 What can we learn from lifetime measurements?	10
1.5 What can we learn from Lepton Universality tests?	11
1.6 What is emerging in the Loch Ness?	15
2 Allegretto	17
2.1 The LHCb detector	17
2.2 Pattern recognition	19
2.3 Calorimeters	24
3 Allegro	27
3.1 Dear b -baryons	27
3.2 Mass measurements	28

3.3	Lifetime measurements	32
3.4	Lepton universality test	37
4	Conclusion	44
	Bibliography	103
	Acknowledgements	109

Abstract

This manuscript summarises a selection of my research activities from the past ten years. I obtained my PhD in 2009 at LAL under the supervision of Marie-Hélène Schune and Jacques Lefrançois. Afterwards I moved to EPFL as a postdoctoral researcher, where I worked for three years in the group of Olivier Schneider. In 2012, I obtained a CNRS position at LAL now IJCLab. Three physics analyses based on the LHCb data, focusing on properties of b -baryons such as masses, lifetimes and a lepton universality test are discussed in this manuscript. For each topic, I cherry picked key experimental points that will be developed in the text. The papers corresponding to these analyses can be found at the end of the document. Specific contributions to the scintillator fibre tracker and the calorimeters of the LHCb detector are also described. The object that you are holding in your hands is not meant to be pedagogical nor an exhaustive review, however, I hope that it contains enough information and references to guide any curiosity that it triggers.

Pour un kilo de Loulou

Orsay, August 30th 2019

I am writing this foreword from an odd place. R_{pK}^{-1} is still blind and hopefully will be unblinded in a few weeks. The expected statistical uncertainty is quite large, about 16%. However, this measurement will say “something” about the $b \rightarrow s\ell^+\ell^-$ anomalies. I am lucky to witness a peculiar time, where saying that we might have signs, indications or hints of New Physics in our LHCb data is not a complete fantasy. Some of the global flavour fits to the Wilson coefficients do report up to five standard deviations with respect to the Standard Model predictions. How exciting is that? Can these anomalies be only a misunderstanding of hadronic uncertainties? That would be rubbish. What do we think of the Leptoquarks? What about the somewhat resilient $U_1 \equiv (\mathbf{3}, \mathbf{1})_{2/3}$?

It goes without saying that flavour physics analyses are not just about New Physics searches, far from it, and this humble document aims at demonstrating so. Part of me though, always envied my peers who were “there” when new or unexpected particles were discovered. Without further ado, let us dive in.

Trois, quatre...

Chapter 1

Allegro non troppo

*A Bird, came down the Walk -
He did not know I saw -
He bit an Angle Worm in halves
And ate the fellow, raw*

Emily Dickinson

1.1 A powerful yet incomplete theory

The Standard Model (SM) of particle physics was invented in the late 60's, it is a quantum gauge theory. Similarly to a lego game, there are only a few different kinds of fundamental particles describing visible matter as we know it. The SM is structured in three families or generations of fermions named quarks and leptons. There are six types of quarks *up, down, charm, strange, top* and *bottom*. The *bottom* quark (*b*), is also referred to as *beauty*-quark. There are three charged leptons e^-, μ^-, τ^- and three associated neutral leptons ν_e, ν_μ, ν_τ [1]. By construction in the SM, three interactions *i.e.*: the electromagnetic, weak and strong interactions are responsible for the transitions between these particles. These interactions are mediated by particles called gauge bosons, γ, Z and W , the gluons, they are described by a gauge group $SU(3)_c \times SU(2)_L \times U(1)_Y$. This group is spontaneously broken down to $SU(3)_c \times U(1)_{em}$, *i.e.*: QCD and QED, through the non-vanishing vacuum expectation value of the Higgs field. Depending on the properties of the fermions and bosons at play, such as electric charge and other quantum numbers, particles will be affected by the interactions in different ways. For example, given that they carry a charge of “colour” only quarks are affected by the strong interaction. The SM of particles physics has often been described as an elegant theory; this is partly due to its precise predictive power. The SM is also appealing since it

offers a wide class of physics observables that can be confronted with experimental measurements, a few examples of which will be discussed in this habilitation. This being said, the SM fails to describe some fairly fundamental aspects of nature. The SM does not accommodate gravity, nor can it explain the mass hierarchy of many orders of magnitude observed between particles. For instance, the mass of an electron is $0.511 \text{ MeV}/c^2$ and the mass of the top quark is $173 \text{ GeV}/c^2$ [1]. Furthermore, satellite experiments such as Planck show that visible matter only comprises 5 % of the universe, the rest is attributed to dark energy (68%) and dark matter (27 %) [2]. In other words, the SM is excellent at describing what seems to be the tip of an iceberg. Both the theory and experimental physics communities share the viewpoint that there must exist sources of New Physics (NP), new theories able to propose a more complete description of nature.

One of the main purposes of the experiments located at the Large Hadron Collider at CERN, is to search for new particles. Experimentally, there are two strategies to search for these unknown particles. The first approach is to “hunt” directly for new particles in the decay products of the proton-proton collisions. This is how the Higgs boson was discovered in 2012 by the ATLAS and CMS collaborations [3]. A second approach is to demonstrate the presence of new particles in an indirect way. The heart of indirect searches relies on a class of physics observables that may differ from SM predictions in the presence of NP. This method is heavily exploited by the LHCb experiment. If one assumes that NP lies at a scale Λ_{NP} higher than the mass of the weak interaction bosons, then one can write a Lagrangian as follows:

$$\mathcal{L}_{\text{NP}} = \mathcal{L}_{\text{SM}} + \sum_{d>4} \sum_{n=1}^{N_d} \frac{c_n^{(d)}}{\Lambda_{\text{NP}}^{d-4}} \mathcal{O}_n^{(d)}, \quad (1.1)$$

where the NP is described by higher order operators suppressed by a scale Λ_{NP} . The rule of the game of flavour physics is twofold. On the one hand it is essential to understand and constrain as precisely as possible SM processes, where no NP is expected. These class of processes are sometimes called “standard candles”, they can be probed using dedicated observables such as mass or lifetime measurements. The second aspect is to search for deviations from SM predictions using “theoretically clean” probes, for instance angular observables, lepton universality tests, *etc.*

This chapter is organised as follow, after a discussion of the theoretical framework employed to make predictions, three observables, namely, masses, lifetimes, and lepton universality tests be will described. They serve as illustrations of how one can poke at different aspects of the physics that we care about. As

will be later discussed in Chapter 2 and 3, the LHCb detector is specialised in the analysis of decays of hadrons containing a b -quark. Following the hadronisation which occurs after the production of pairs of b -quarks (for instance in gluon-gluon fusion processes) all types of b -hadrons are produced and in particular b -baryons. Their organisation within a quark model is shown in Figure 1.1. b -baryons have emerged as a pattern in the research that I have conducted in the past years. Their properties and the observables that they allow to reach are used as a “fil conducteur” throughout the work documented in this habilitation.

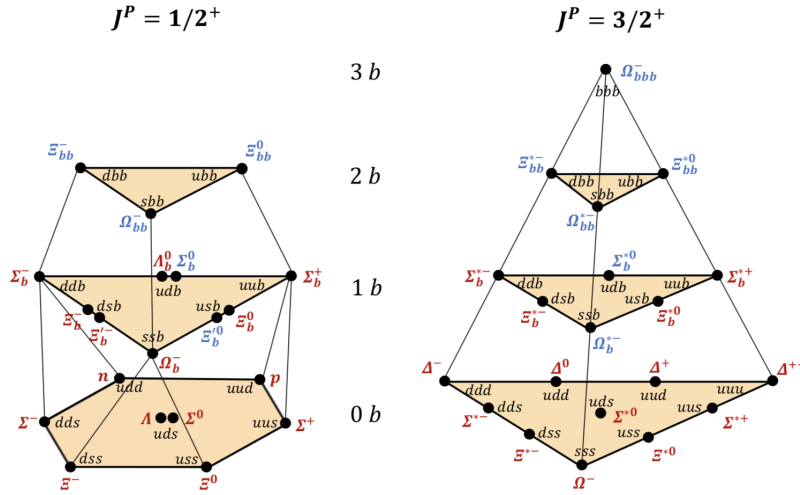


Figure 1.1: SU(4) multiplets of baryons made of u , d , s and b quarks. Left: the multiplet with an SU(3) octet on the lowest level. Right: the multiplet with an SU(3) decuplet on the lowest level. Observed states are shown in red, while predicted unobserved states are in blue [1].

1.2 Handling multi-scale problems

Effective Field Theories (EFTs) are powerful tools to describe high energy NP phenomena and their effect on precision observables. Their strength lies in their ability to separate and treat multi-scale problems such as for example $b \rightarrow s\ell^+\ell^-$ transitions. At each scale, all the degrees of freedom with properties higher than the value of the scale will be integrated out. For instance, let us consider tree-level $b \rightarrow c$ decay, in the SM at the lowest order it mediated by the exchange of W boson, these transitions are referred to a Flavour Changing Charged Current (FCCC). For this type of decay, the momentum transfer from the W is very small in comparison to its mass, one can write:

$$\frac{-g_{\mu\nu} + q_\mu q_\nu / M_W^2}{q^2 - M_W^2} \xrightarrow{q^2 \ll M_W^2} \frac{g_{\mu\nu}}{M_W^2}, \quad (1.2)$$

The charged current can be reduced to a point-like four fermion interaction by "integrating-out" the W boson. This is illustrated in Figure: 1.2. Different models can be adopted depending on the scale where

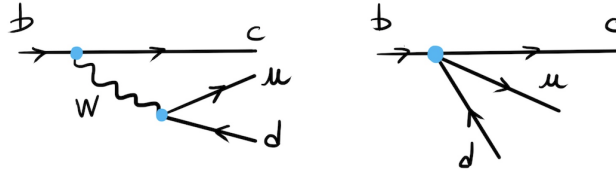


Figure 1.2: Example of "integrating-out" a W boson in a FCCC.

one is trying to address a specific problem or make a prediction for a physics observable. Examples of models which will be later discussed in this document as a function of energy are illustrated in Figure 1.3. What makes EFTs powerful to describe NP is that they can be used to study processes, where one does not know a priori the underlying ultra violet (UV) theory [4, 5]. Another usage of EFT is the study of low energy properties of the strong interaction, for example Chiral Perturbative Theory or Heavy Quark Expansion Theory [6, 7] which do not rely on fully perturbative computations.

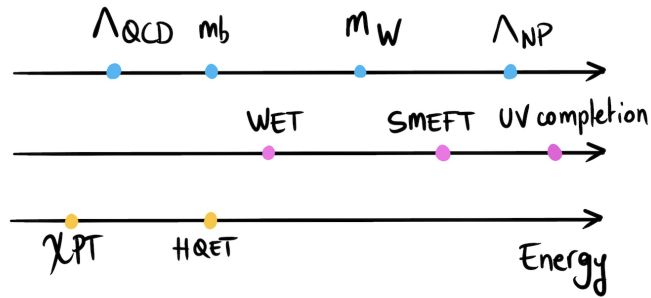


Figure 1.3: Sketch of relevant energy scale (first line), New Physics EFTs and QCD ones.

In the EFT framework, the phenomenology of b -decays can be described in a convenient way, with an Effective Hamiltonian formalism [6, 8, 9]. For a given initial state I going to a final state F , the amplitude can be written as :

$$\mathcal{A}(I \rightarrow F) = \langle F | \mathcal{H}_{\text{eff}} | I \rangle, \quad (1.3)$$

where the \mathcal{H}_{eff} describes both the low energy dynamics (long distance) and high energy ones (short distance).

1.3 What can we learn from mass measurements?

A hadron can be thought of as a bound state of constituent quarks. It can either form a meson ($q\bar{q}$), a baryon ($qqq, \bar{q}\bar{q}\bar{q}$) or more exotic combinations such as tetra- or pentaquarks [10]. This classification was first proposed by Gell-Mann and Nishijima in 1958. The generalised Gell-Mann-Nishijima formula relating the various hadron quantum numbers is given by:

$$Q = I_z + \frac{\mathcal{B} + S + C + B + T}{2} \quad (1.4)$$

where Q is the charge, \mathcal{B} is the baryon number, I_z is the z projection of the Isospin and S, C, B and T are the *avour* of the quark. While, we know today that there are six types of quarks, *up, down, strange, charm, top* and *beauty*, one should remember that at that time, Gell-Mann and Nishijima, nor any other physicists, were not aware of the existence of neither the *charm, beauty* nor the *top* quark. Nevertheless, they were able to predict the existence of the $\Omega^-(sss)$ baryon discovered in 1964 in a hydrogen bubble chamber. The masses, which are one of the most fundamental properties of all hadrons, are a pure QCD effect. One could write in a simplified way:

$$m_{\text{hadron}} = \sum_i m_{\text{quark}}^i + E_{\text{Binding}} \quad (1.5)$$

Except for the top quark, there are not free quarks in nature. This makes the information about their mass difficult to access. Furthermore, the binding energy is completely driven by QCD effects. Therefore, relatively large uncertainties in the theoretical description of hadron masses are expected, see for example those predictions listed in Table 1.1. Given that baryons are three-body systems, the theory describing their dynamics within quark models is much more complicated than that for mesons. There are many approaches used within QCD to predict their properties. For example non-relativistic formulations of QCD, quark models [1] or light-cone sum rules [11] allow us to investigate the dependence of the baryon mass splittings on the heavy and light quark masses. In lattice QCD, the correlation functions used to compute the action for baryons are more difficult to determine than those for mesons, therefore it is comparatively harder to extract a reliable mass spectrum for heavy baryons [12]. The predictions of the CQM [13] method for example, rely on the knowledge of the charm baryonic counter part. The spread of the predictions and their uncertainties in Table 1.1 demonstrate that precise measurements of many

heavy hadron and in particular b -baryon masses help to either exclude some of the theoretical approaches or contribute to refining them. Furthermore, a better understanding of the dynamics of quarks inside the hadrons can help to understand and characterize the nature of exotic particles, such as the pentaquarks, the $X(3872)$ or the $Z(4140)$, *etc.* which have been observed in the past years at the B -factories and at the LHC [1].

Prediction	Λ_b^0 mass	Ξ_b^- mass	Ω_b^- mass
CQM [13]	Used as input	5790-5800	6052.1 ± 5.6
$1/N_c$ expansion [14]	Used as input	Used as input	6039.1 ± 8.3
RCQM [15]	5211 ± 100	5812 ± 100	6065 ± 100
HQET + QCD sum rule [16]	5637_{-56}^{+68}	5780_{-68}^{+73}	6036 ± 81
QCD sum rule [17]	5690 ± 130		5890 ± 180
Lattice QCD [18]	$5641 \pm 21_{-33}^{+15}$	$5781 \pm 17_{-16}^{+17}$	$6006 \pm 10_{-19}^{+20}$

Table 1.1: Mass predictions in MeV/c^2 for Λ_b^0 , Ξ_b^- and Ω_b^- baryons.

1.4 What can we learn from lifetime measurements?

Another fundamental property of particles is their lifetime. While at first order all b -hadron lifetimes are expected to be the same, the presence of the spectator quark displayed in Figure 1.4 can not be ignored in accurate numerical computations. Non-perturbative effects to heavy-flavour decays can be expressed through an expansion in inverse powers of m_b . The decay rate of the transition of a b -hadron, H_b , to an inclusive final state X , can be expressed in terms of a phase-space integral (PS) of the square of the matrix element, summed over all final state X with the same quantum numbers

$$\Gamma(H_b \rightarrow X) = \frac{1}{2m_{H_b}} \sum_X \int_{\text{PS}} (2\pi)^4 \delta^{(4)}(p_{H_b} - p_X) |\langle X | H_{\text{eff}} | H_b \rangle|^2 \quad (1.6)$$

Explicitly calculating the integral, one arrives at the Heavy Quark Expansion [7] of decay rates of heavy hadrons:

$$\Gamma(H_b \rightarrow X) = \Gamma_0 + \frac{\Lambda^2}{m_b^2} \Gamma_2 + \frac{\Lambda^3}{m_b^3} \Gamma_3 + \frac{\Lambda^4}{m_b^4} \Gamma_4 + \dots, \quad (1.7)$$

where the expansion parameter is denoted Λ/m_b , where the typical scale of Λ is ~ 1 GeV.

Each of the Γ_i terms of the expansion describes different aspects of the possible effects inside the hadrons.

- Γ_0 *spectator model* all b -hadrons have the same lifetime.

- There are no corrections in $1/m_b$.
- Γ_2 *Fermi motion* and *chromomagnetic interaction*, first corrections due to the strong interaction, isospin, at this order one would expect : $\tau_{B^+}/\tau_{B^0} - 1 \approx 0$ and $\tau_{\Lambda_b^0}/\tau_{B^0} - 1 \approx 2\%$.
- Γ_3 *Weak annihilation* and *Pauli interference*, the spectator quark is involved only at $1/m_b^3$ order.

The measurement of the lifetime differences of b -hadrons allows therefore to test HQET at the third order.

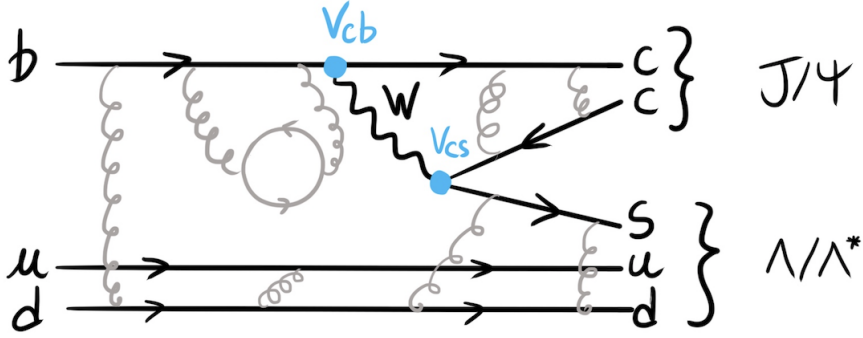


Figure 1.4: Feynman diagram of $\Lambda_b^0 \rightarrow J/\psi \Lambda^{(*)}$

One important assumption behind the heavy quark expansion is the so-called *quark-hadron* duality. It can be translated as follows: rates computed at the quark-gluon level are equal to the corresponding observables involving hadrons. Extensive discussions can be found in the literature regarding this assumption. One of the best ways to test this is to confront HQET computations to experimental measurements. A detailed review and summary of HQET principles can be found in Ref. [19] and useful references can be found in Refs. [20],[21], [22].

1.5 What can we learn from Lepton Universality tests?

Within the SM, there are no Flavour Changing Neutral Currents (FCNC) at tree level, as a consequence $b \rightarrow s \ell^+ \ell^-$ transitions can only occur through loops. Therefore, NP contributions can compete with the SM ones, which makes $b \rightarrow s \ell^+ \ell^-$ transitions a particularly interesting laboratory. For instance, in Figure: 1.5 the SM gauge boson Z could be replaced by a new particle, such as a heavier gauge boson, for example the Z' or Leptoquarks.

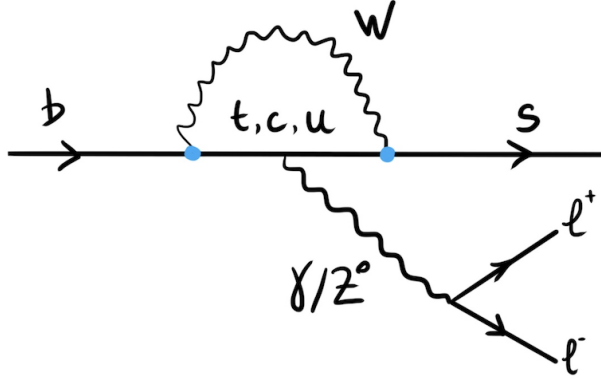


Figure 1.5: Feynman diagram of a $b \rightarrow s \ell^+ \ell^-$ transition.

For these decays, the effective Hamiltonian, \mathcal{H}_{eff} is defined as:

$$\mathcal{H}_{\text{eff}} = \frac{G_F}{\sqrt{2}} \lambda^{\text{CKM}} \sum_i C_i \mathcal{O}_i, \quad (1.8)$$

where G_F is the Fermi constant and λ^{CKM} are the Cabibbo-Kobayashi-Maskawa terms describing the coupling between the W^\pm bosons and the quarks [1]. In this formalism, the hard contributions generated by the electromagnetic, weak, and strong interactions can be factorised depending on their energy scale at leading order. The low energy part of the transition, typically lower than the mass of the b -quark, mediated for example by soft gluons, is encoded in what are called hadronic matrix elements, \mathcal{O}_i . These elements can be evaluated using “numerical” techniques such as Lattice QCD [23]. The Wilson coefficients C_i , on the other hand describe short distance contributions to the transition occurring at high energy, typically $\mathcal{O}(m_W)$. These coefficients can be calculated using perturbative methods [24].

As shown in Equation 1.8, with EFTs one can factorise long distance from short distance components. The short distances parts, which are sensitive to NP, are encoded in the Wilson coefficients. The dominant operators relevant for $b \rightarrow s \ell^+ \ell^-$ transitions are:

$$\mathcal{O}_7 = \frac{e}{16\pi^2} m_b (\bar{s} \sigma_{\mu\nu} P_R b) F^{\mu\nu}; \quad (1.9)$$

$$\mathcal{O}_9 = \frac{e^2}{16\pi^2} (\bar{s} \gamma_\mu P_L b) (\bar{\ell} \gamma^\mu \ell); \quad (1.10)$$

$$\mathcal{O}_{10} = \frac{e^2}{16\pi^2} (\bar{s} \gamma_\mu P_L b) (\bar{\ell} \gamma^\mu \gamma_5 \ell); \quad (1.11)$$

where $P_{L,R} = (1 \mp \gamma_5)/2$ are the projectors for left-(right-)handed chirality. P_L corresponds to the $V - A$

structure of the weak interaction in the SM. Due to the universality of lepton couplings for the three generations, the SM Wilson coefficients have the same value for all three lepton generations. The determination of the Wilson coefficients requires a matching of the high-energy theory (in this case the SM) and at the electroweak scale and a running from this scale down to the low-energy one close to the mass of the b quark. NP can manifest itself as shifts to the Wilson coefficients or enhancements of new operators which are either absent or strongly suppressed in the SM.

One interesting feature of $b \rightarrow s\ell^+\ell^-$ decays is shown in Figure: 1.6. It displays the variation of the differential rate *i.e.* the probability of a $b \rightarrow s\ell^+\ell^-$ decay to occur as a function of q^2 , where q^2 is the sum square of the di-lepton system invariant mass. In particular, it is worth noting that Wilson coefficients ($C_7^{(\prime)}, C_9^{(\prime)}, C_{10}^{(\prime)}$) contribute differently to the different q^2 regions. For example, the very low q^2 region is dominated by the Wilson coefficient $C_7^{(\prime)}$ corresponding to a Feynman diagram where a photon is produced as illustrated in Figure: 1.6. Therefore, to fully exploit the rich phenomenology of these decays, experimental measurements, such as branching fractions, forward-backward asymmetry, *etc.* are performed as a function of q^2 . In order to constrain the values of the Wilson coefficients, the LHCb collaboration

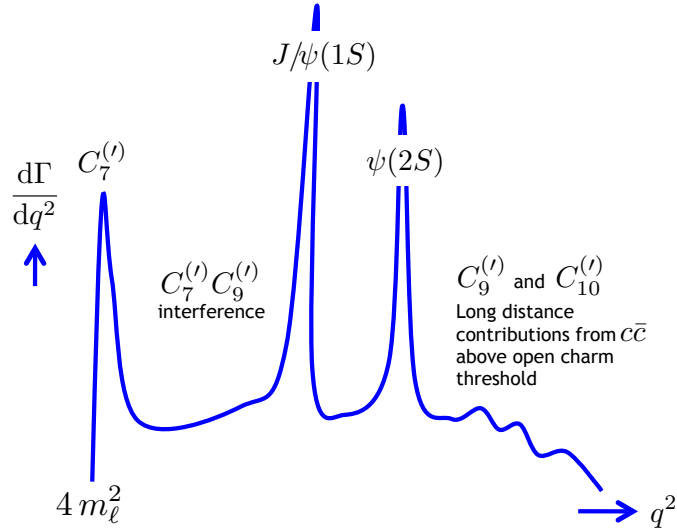


Figure 1.6: Differential rate as a function of q^2 in $b \rightarrow s\ell^+\ell^-$ transitions.

has conducted many measurements of $b \rightarrow s\ell^+\ell^-$ transitions, such as differential branching fraction of $B^+ \rightarrow K^+\mu^+\mu^-$, $B^0 \rightarrow K^{*0}\mu^+\mu^-$, as well as $B_s^0 \rightarrow \phi\mu^+\mu^-$ and $\Lambda_b^0 \rightarrow \Lambda\mu^+\mu^-$. A few deviations have been observed with respect to the SM predictions. Similar patterns have been observed in angular analyses, where optimised observables, for example P_5' , have been designed and employed to minimize the impact

of hadronic uncertainties, as shown in Figure: 1.7.

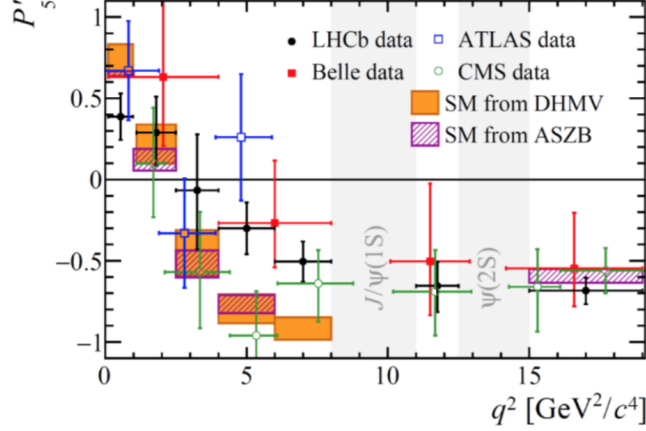


Figure 1.7: Measurements of P'_5 by different experiments, compared to the theoretical predictions.

Lepton Universality (LU) is an “accidental” property of the SM. It predicts equal coupling of the SM gauge bosons to all three families of leptons at tree-level. Lepton universality tests form some of the “cleanest” observables, since all the hadronic uncertainties in these decays cancel in the ratios leaving only differences due to QED corrections, which are expected to be very small [25]. This property can be tested in many sectors and in particular in loop-induced decays such as $b \rightarrow s\ell^+\ell^-$ transitions, but also tree-level decays such as $b \rightarrow c\ell\nu_\ell$ decays. For this latter process, the ratios $R_D = 0.299 \pm 0.003$ and $R_{D^*} = 0.258 \pm 0.005$ were measured at the B -factories and LHCb and lie 3.5 standard deviations above the SM predictions. The current world average agrees with the SM at only three standard deviations [26]. For $b \rightarrow s\ell^+\ell^-$ transitions, the LU ratios are defined as as:

$$R_H \equiv \frac{\int \frac{d\Gamma(B \rightarrow H\mu^+\mu^-)}{dq^2} dq^2}{\int \frac{d\Gamma(B \rightarrow He^+e^-)}{dq^2} dq^2}. \quad (1.12)$$

LU in $b \rightarrow s\ell^+\ell^-$ decays has been tested until now in B meson decays by the LHCb experiment [27], [28], and the results as a function of q^2 are :

$$R_K = 0.846^{+0.060}_{-0.054} \quad {}^{+0.016}_{-0.014}, \quad q^2 \in [1, 6] \text{ GeV}^2/c^4, \quad (1.13)$$

$$R_{K^*0} = \begin{cases} 0.66^{+0.11}_{-0.07} \pm 0.03, & q^2 \in [0.045, 1.1] \text{ GeV}^2/c^4, \\ 0.69^{+0.11}_{-0.07} \pm 0.05, & q^2 \in [1.1, 6.0] \text{ GeV}^2/c^4. \end{cases}$$

While these results are still statistically limited, it is important to extend the scope of these measurements

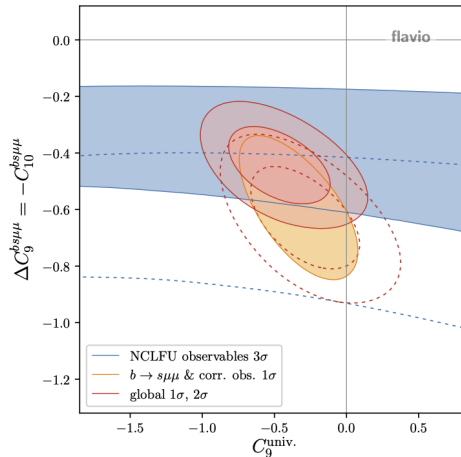


Figure 1.8: Likelihood contours from neutral current LFU observables and the global fit in the the plane of a lepton flavour universal contribution to C_9^{univ} Figure taken from Ref.[32].

to verify if the pattern of a “deficit” of muons emerging from the LU tests together with the branching fraction measurements in the muonic decays [29, 30], holds or not.

Recently, Ref.[4] argued that if NP has a $V - A$ structure, *i.e.* $C_9 = -C_{10}$, then one expects in the SM that the electron-muon LU ratios across all species of b -hadrons should be the same:

$$R_K \approx R_{K^*0} \approx R_{K\pi\pi} \approx R_{K_S} \approx R_\phi \approx R_\Lambda \approx R_{pK}. \quad (1.14)$$

The first test of lepton universality with a b -baryon is discussed in this habilitation in Chapter 3.

1.6 What is emerging in the Loch Ness?

As of today there are a few phenomenological attempts to fits the Wilson coefficients. While some of these approaches differ in their treatment of the hadronic uncertainties [31], which can manifest themselves in the size of the uncertainties on form factors for instance, most of them seem to draw a similar picture.

An example of such a phenomenological study [32] is shown in Figure 1.8. The selected result displays one of the phenomenological global fits, with a lepton flavour universal C_9^{univ} Wilson coefficient shown as a function of a scenario linking a purely muonic contribution to C_9 and a $C_9^{bs\mu\mu} = -C_{10}^{bs\mu\mu}$ hypothesis, before and after the inclusion of the latest R_K result from LHCb. This pattern of Wilson coefficients can be found in several NP models with tree-level mediators, such as Leptoquarks.

While there has been a myriad of theory developments in the past few years to interpret the flavour anomalies in a consistent and coherent way, Leptoquarks, which are tree-level mediators, have received particular attention. Given the experimental constraints from both loop-induced currents and tree-level decays, there are today three viable options for Leptoquarks models summarised in Table 1.2. The first option is based on models which predict a U_1 Leptoquark and necessitate UV completion [33, 34, 35, 36]. The other two make use of two scalar Leptoquarks $S_1 + S_3$ [37, 38, 39] or $S_3 + R_2$ [5]. It will be most interesting to see in the next few years which scenarios survive the additional experimental constraints.

Model	$R_{K^{(*)}}$	$R_{D^{(*)}}$	$R_{K^{(*)}} \& R_{D^{(*)}}$
$S_1 = (3, 1)_{-1/3}$	✗	✓	✗
$R_2 = (3, 2)_{7/6}$	✗	✓	✗
$\tilde{R}_2 = (3, 2)_{1/6}$	✗	✗	✗
$S_3 = (3, 3)_{-1/3}$	✓	✗	✗
$U_1 = (3, 1)_{2/3}$	✓	✓	✓
$U_3 = (3, 3)_{2/3}$	✓	✗	✗

Table 1.2: Summary of Leptoquark models which can accommodate $R_{K^{(*)}}$, $R_{D^{(*)}}$ and both. Table based on work from Ref. [40]. The SM quantum numbers are denoted by $(SU(3)_c, SU(2)_L)_Y$.

Pick your horse in Figure 1.9, the bets are open !

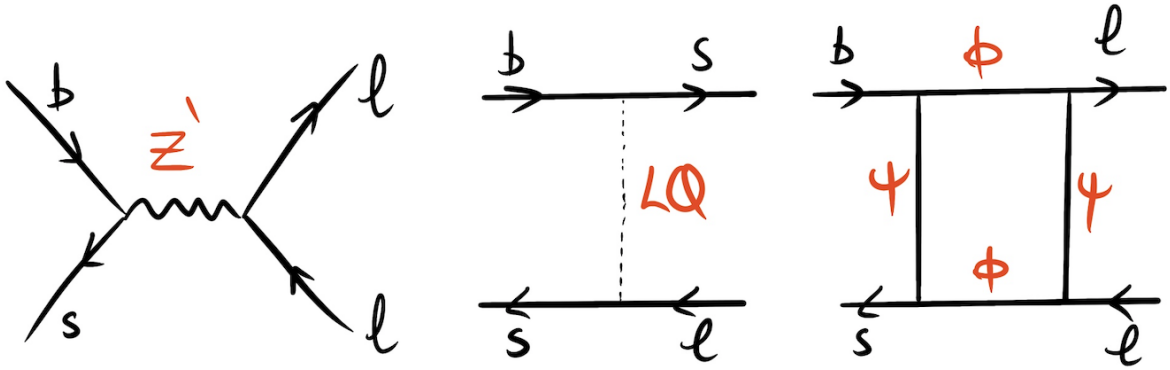


Figure 1.9: Example of NP Feynman diagrams [41],[42],[43].

Chapter 2

Allegretto

*\Don't you know that Rome
wasn't built in a day"*

Morcheeba

2.1 The LHCb detector

The LHCb detector [44], shown in Figure 2.1, was designed to study the asymmetry between matter and anti-matter, and search for physics beyond the SM in b -hadron decays. It turned out that the excellent performance of the detector was such that the physics program was extended very rapidly to explore also charm, electroweak, and, more recently, heavy ion physics.

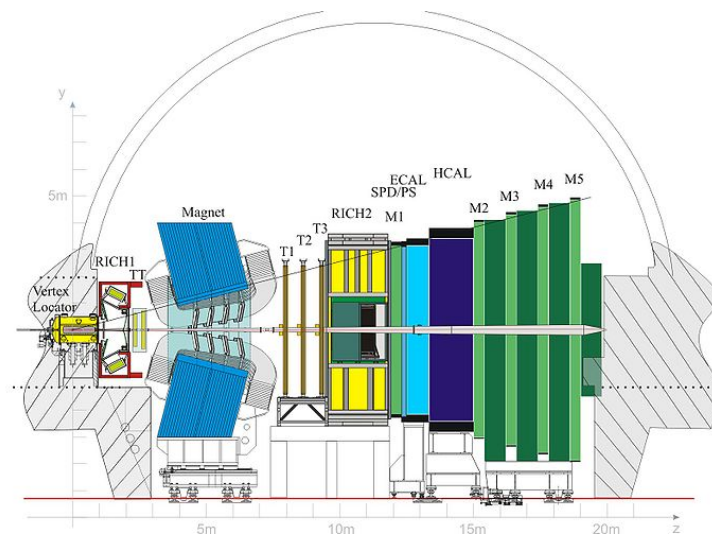


Figure 2.1: The LHCb detector [44].

LHCb is a single-arm spectrometer located at the interaction point (IP) 8 of the LHC. The choice of detector geometry is justified by the fact that both b and \bar{b} hadrons are predominantly produced in the same forward or backward cone. If our collaboration had the budget of the ministry of defence we would probably have built two LHCb detectors, to catch both the forward and backward pairs. Charged tracks are detected by a vertex locator near to the IP, and their momenta and charge are subsequently determined with tracking stations (TT, T1, T2 and T3) either side of a magnet providing an integrated field of 4 Tm. The tracking efficiencies were found to be $\sim 96\%$ for $J/\psi \rightarrow \mu^+\mu^-$ in the momentum range $5 \text{ GeV}/c < p < 200 \text{ GeV}/c$. Ring imaging Cherenkov (RICH) counters are used to distinguish kaons, pions and protons. An excellent hadron identification is crucial for a flavour experiment¹, for example the measurement of CP asymmetries in $B_{d,s}^0 \rightarrow \pi\pi, KK, \pi\pi$ decays. Electromagnetic and hadronic calorimeters (ECAL and HCAL), together with an instrumented preshower (SPD/PS) system, provide measurements of the energies of neutral particles as well as electrons. Finally, muons are identified with a dedicated detection system (M1-M5). The vertex locator provides precise information on the origin of the tracks and the tracking stations are essential to measure the momenta of the particles involved in the decay of the particles of interest. This gives extremely powerful information to reject background, since signal tracks *i.e.* secondary particles produced by the particles of interest, must originate from common vertices that are displaced from the primary vertex of the LHC proton-proton collision, due to the non-negligible lifetimes of the decaying bottom hadrons ($\mathcal{O}(1)$ ps), whereas the largest potential source of background is from random combinations of tracks that originate from the primary vertex. The LHCb trigger is a key to the success of the experiment. It operates in two stages. A hardware trigger based on the information provided by the calorimeters and the muon chambers reduces the frequency of events from the LHC beam crossing rate of up to 40 MHz to a rate of 1 MHz at which the entire detector can be read out. The subsequent high-level software trigger stage was responsible for reducing the output rate to a level at which data can be written to permanent storage. This rate evolved significantly between Run 1 and Run 2, reaching 12.5 kHz at the end of Run 2. Detailed discussion of the performances of the LHCb detector can be found in Ref. [45]. The Run naming convention and the schedule of the LHC are defined in Table 2.1.

Run 1	LS1	Run 2	LS2	Run 3	LS3	Run 4...
2010-2012	2013-2015	2015-2018	2018 - 2020	2021-2024	2025 - 2027	2027 -

Table 2.1: LHC schedule. The data taking period are highlighted in blue, the technical stops are highlighted in yellow.

¹For instance, for a requirement on the $K-\pi$ separation, $\Delta \log \mathcal{L}(K - \pi) > 0$, when averaging over the momentum range 2-100 GeV/c one finds the kaon efficiency to be $\sim 95\%$ with a pion misidentification rate of $\sim 10\%$.

The LHCb detector is currently undergoing its first major upgrade to allow for data taking at $2 \times 10^{33} \text{cm}^{-2} \text{s}^{-1}$ in 2021, a factor five increase compared to earlier runs. All the tracking system will be replaced [46]. The vertex locator strips will be replaced by pixel detectors [47], and the TT will be upgraded to an Upstream Tracker (UT) with a larger acceptance around the beam pipe. The central trackers will be replaced with a scintillating fibre tracker (SciFi). Furthermore, the entire electronics will be replaced to allow the detector to be read out at the proton-proton collision rate, and to send the data to be processed online in the high level trigger. In order to maximise the physics output of the experiment, the philosophy of the collaboration has been to perform full track reconstruction, including particle identification and track fitting, as early as possible in the data processing.

I have been involved in two upgrade projects. With my former PhD student Renato Quagliani [48], whom I co-supervised with Patrick Robbe and colleagues from LPNHE in Paris, Pierre Billoir and Francesco Polci, we developed a pattern recognition algorithm that we baptised Hybrid Seeding. The aim of this tracking algorithm is to reconstruct track segments using only in the information of the SciFi, enabling later the reconstruction of long-lived particles such as K_S^0 , Λ or more exotic ones, like dark photon candidates. This algorithm and its performance are discussed in Section 2.2. I am also involved in a hardware project for the calorimeter, where I am responsible for a control board designed by O.Duarte and A.Saussac. The purpose of this board is to distribute information from the central LHCb system such as the 40 MHz clock and propagate it to the calorimeter front-end boards. The design of this board is described Section 2.3.

2.2 Pattern recognition

The LHCb upgrade tracking algorithms rely on three detectors: the vertex locator, the upstream tracker and the scintillating fibre tracker. Figure 2.2 shows the different types of tracks produced by the reconstruction; their somewhat jargonic classification can be found in Table 2.2.

The SciFi tracker [49] is composed of three tracking stations, T1, T2, T3. Each station is composed of four layers, separated by air-filled gap of 50 mm, oriented in the so called *stereo* configuration (x - u - v - x). The fibre mats in the first and fourth x -*layer* (within the same station) are vertically oriented, *i.e.* the fibre mats are parallel to the y axis of the laboratory frame. Therefore, the read-out of a x -*layer* provides the direct measurement of the $x^{track}(z_{layer})$ position. But no information at all about the y can be directly extracted. The second (u) and the third (v) layers are identical to the x -*layer*, but their fibre mats are

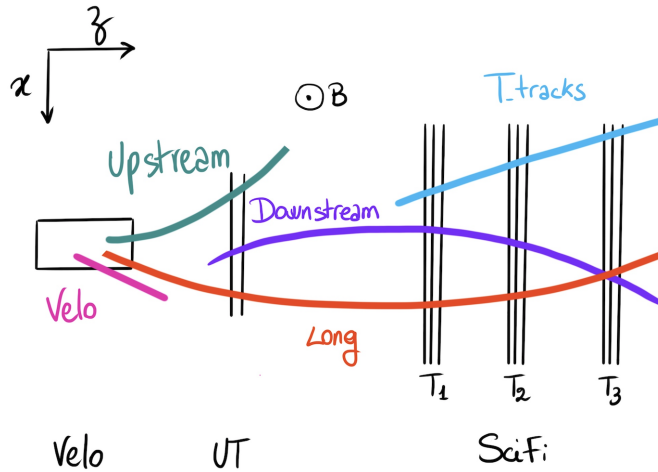


Figure 2.2: Track types in the LHCb Upgrade.

tilted with respect to the x -layer by $+5^\circ$ and -5° respectively. The read-out of the u/v -layers provides the u and v stereo coordinates, which are used to extract the information on the y - z plane motion of the particles.

The SciFi tracker benefits from a good uniformity whereas the former central tracking system, was based on different technologies, mechanical supports *etc.*. This ensures that the fraction of particles that survive the passage through the SciFi Tracker is quite high. The fraction was found to be 96.9% for hadrons, 93.9% for electrons and 95.2% for photons. With the SciFi, a difficulty was introduced by the absence of a y -segmentation in the tracker. This feature makes the track finding close to the beam pipe, where the detector occupancy is the highest, quite challenging, and the impact of the loss of light propagation in the fibres, a particular problem. Renato worked out a way around this. From the expected y -position of a traversing track based on the information from the x -layers and the stereo ones, he figured out a way to tune the hit requirements of the tracks according to the expected light attenuation in the SciFi fibres, which reduced significantly the fake (or ghost) rate.

The decay rates and topologies considered for the LHCb Upgrade are very broad [46]. They vary from rare decays, such as the very rare $B_s^0 \rightarrow \mu^+ \mu^-$ mode or the radiative mode $\Lambda_b^0 \rightarrow \Lambda \gamma$, to multi-track final states such as $B_s^0 \rightarrow D_s^+ (\rightarrow K^+ K^- \pi^+) D_s^- (\rightarrow K^+ K^- \pi^-)$. One has also to take into account from the spread of the momentum ranges of these particles, from the very soft tracks like the pions from D^* decays all the way to the hard ones from W and Z decays. With this in mind, the algorithm was designed to reach a good compromise in the holy tracking trinity: high tracking efficiencies and low fake rate and small processing

time.

The main idea behind the Hybrid Seeding is to progressively clean the tracking environment by first finding the tracks which are easier to reconstruct, and then searching for those with more complicated trajectories or signatures using the left-over hits.

Some of the improvements reached were achieved thanks to an update of the track parametrisation, an optimisation of the search windows and a redesign of the loops over the hit containers. The rethinking of recovery routines permitted to improve the low momentum track efficiency and the robustness of the algorithm.

Name	Property
<i>hasT</i>	<i>reconstructible</i> in <i>Scintillating Fiber Tracker</i>
<i>UT + Scintillating Fiber Tracker</i>	<i>reconstructible</i> in <i>Scintillating Fiber Tracker</i> and <i>UT</i>
<i>noVelo</i>	not <i>reconstructible</i> in the VELO
<i>long</i>	<i>reconstructible</i> in VELO and <i>Scintillating Fiber Tracker</i>
<i>strange</i>	daughter of a strange particle (K_s^0 , Λ , ..)
<i>from B</i>	belong to the decay chain of a <i>b</i> hadron
<i>from D</i>	belong to the decay chain of a <i>c</i> hadron

Table 2.2: Sub-selections used by the performances indicators.

The results obtained from these studies are summarised in Table 2.3 and Figure 2.3. They make clear that the Hybrid Seeding performs significantly better than the first implementation of the prototype algorithm referred to in this text as TDR Seeding. A significant improvement is achieved in all the fields:

- The *ghost rate* is reduced by a factor two with respect to the old seeding version (even when averaged for the events), and the efficiencies are significantly larger.
- The *tracking efficiencies* are significantly improved for all the track categories, especially for lower p and p_T tracks ($\sim 20\%$), while for higher p a gain of 4-6 % is achieved.
- The *clone killing* which allows to remove duplicate candidates is more efficient than the previous algorithm. This is achieved thanks to a more accurate track comparison and to the internal sorting of the hits, which allows a better track-to-track comparison.
- The *timing* of the Hybrid Seeding is significantly improved with respect to TDR Seeding, by almost a factor 3-4 on average (depending on the detector occupancy level), as shown in Table 2.3.

In other words, Hybrid Seeding is more robust against busy events with respect to the TDR Seeding. Timing comparisons have been achieved running both the algorithms on the same machine (a standard lxplus machine SLC6 in 64-bit mode) and we also quote the timing of the *forward tracking* algorithm (as a reference value) in the so called best tracking sequence stage, *i.e.*, the configuration aiming to find all *long* tracks in the event.

Machine speed <i>n</i> · 2.8 GHz Xenon	Algorithm	Avg. time [$\frac{ms}{evt.}$]	Min. time [$\frac{ms}{evt.}$]	Max. time [$\frac{ms}{evt.}$]
2.79	Forward Tracking Best	48.62	0.30	1271.4
	TDR Seeding	150.95	1.86	6069.0
	Hybrid Seeding	46.80	0.70	1239.1

Table 2.3: Average, maximum and minimum timing of the algorithms for the different samples. Timing performances are also quoted with respect to the *forward* tracking used for the upgrade.

Track type	Sample 2	
	TDR Seeding ϵ (clone rate)	Hybrid Seeding ϵ (clone rate)
<i>hasT</i>	(53.5 ± 0.1)(3.5) %	(66.6 ± 0.1)(0.0) %
<i>long</i>	(78.4 ± 0.1)(3.3) %	(92.1 ± 0.1)(0.0) %
<i>long P > 5 GeV/c</i>	(87.5 ± 0.1)(2.6) %	(95.4 ± 0.4)(0.0) %
<i>long from B</i>	(80.4 ± 0.6)(2.7) %	(93.0 ± 0.3)(0.0) %
<i>long from B P > 5 GeV/c</i>	(88.5 ± 0.5)(2.3) %	(95.9 ± 0.1)(0.0) %
<i>long from B or D</i>	(80.7 ± 0.2)(2.7) %	(93.3 ± 0.1)(0.0) %
<i>long from B or D P > 5 GeV/c</i>	(89.3 ± 0.2)(2.3) %	(95.9 ± 0.1)(0.0) %
<i>UT + Scintillating Fiber Tracker strange</i>	(76.3 ± 0.1)(3.3) %	(91.8 ± 0.1)(0.0) %
<i>UT + Scintillating Fiber Tracker strange P > 5 GeV/c</i>	(88.8 ± 0.1)(2.5) %	(95.7 ± 0.1)(0.0) %
<i>noVELO + UT + Scintillating Fiber Tracker strange</i>	(76.8 ± 0.2)(3.3) %	(91.3 ± 0.1)(0.0) %
<i>noVELO + UT + Scintillating Fiber Tracker strange P > 5 GeV/c</i>	(88.7 ± 0.2)(2.7) %	(95.6 ± 0.1)(0.0) %
<i>ghost rate</i>	(37.3 ± 0.1) %	(19.4 ± 0.1) %
<i>ghost rate (evt.avg)</i>	21.6 %	11.2 %
<i>hit purity</i>	98.9 %	99.6 %
<i>hit efficiency</i>	93.6 %	95.4 %

Table 2.4: Tracking performance comparison between the TDR Seeding and the Hybrid Seeding algorithms.

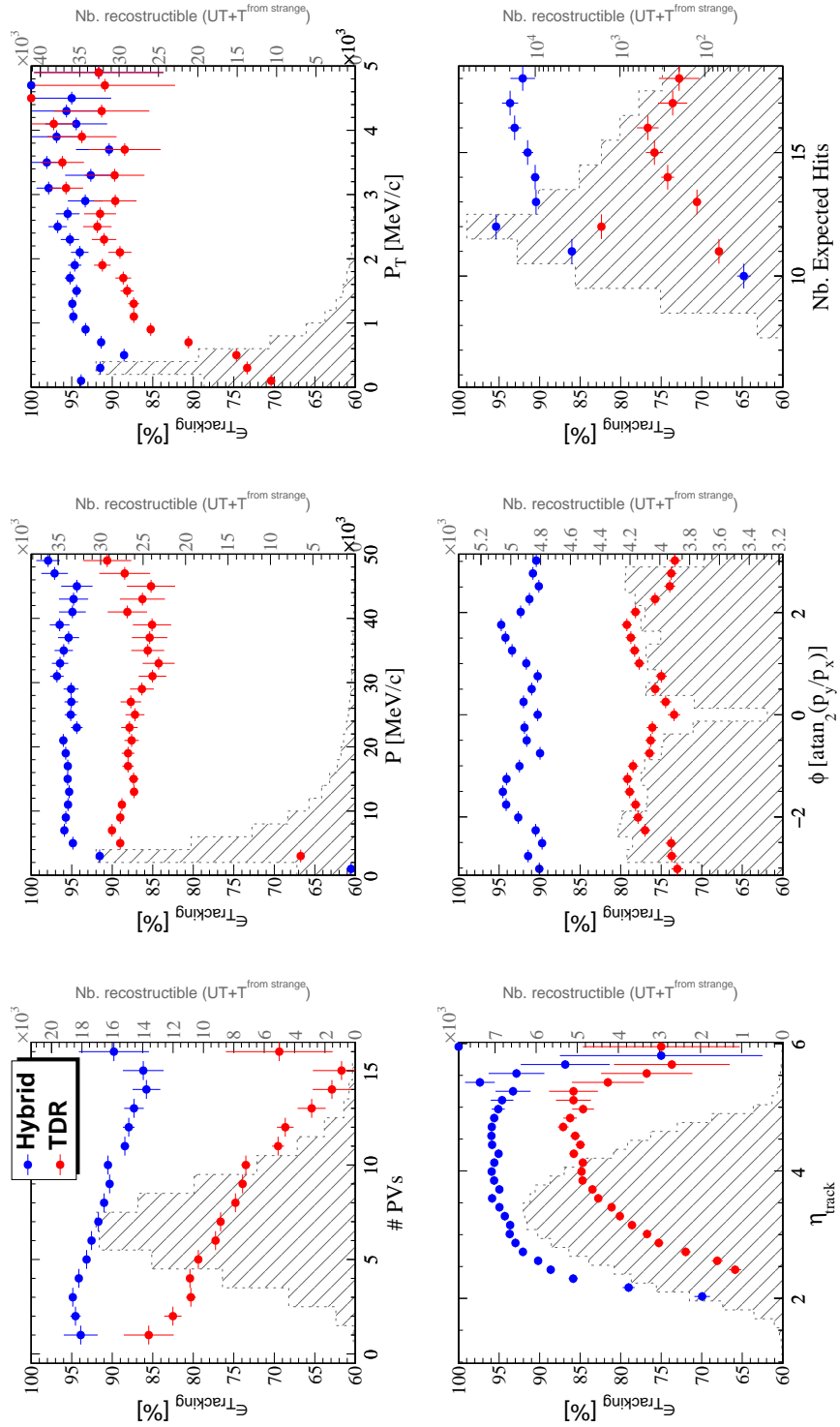


Figure 2.3: Tracking efficiency distributions, selecting tracks having hits in the *UT* and the *Scintillating Fiber Tracker* and being daughters of long-lived strange particles, such as K_S^0 or Λ^0 . The efficiencies obtained with the Hybrid Seeding (blue) algorithm are on average $\simeq 12\%$ better than the ones from the TDR Seeding.

The performance quoted in this section have been obtained with a description of the SciFi geometry which was not final. However, even with more refined versions of the geometry, which were later made available, the overall conclusions of this work remain unchanged. The Hybrid Seeding algorithm has continued to evolve, and further improvements have been achieved. More recently, the focus of the efforts has been towards improving the reconstruction electrons at low momenta.

2.3 Calorimeters

As part of the first phase of the LHCb upgrade and the calorimeters upgrade in particular, both the SPD and PS detectors have been removed and the entire electronics of the system will be replaced. There will no longer be a hardware trigger and the aim is to process all the subdetectors at 40 MHz. The electromagnetic (ECAL) and hadronic (HCAL) calorimeters will remain in place. They are both based on a “shashlik” technology of lead/iron and scintillators, and the light is collected by wave length shifting fibres [50]. The ECAL energy resolution is $10\%/\sqrt{E} \oplus 1\%$ where the energy is expressed in GeV. The information provided by this sub-detector is used as input to the particle identifications algorithms and flags photons, neutral pions or electrons. The HCAL energy resolution is significantly worse being $80\%/\sqrt{E}$, however this was enough to provide information for the hardware trigger (L0) during Run 1 and 2.

The new acquisition systems of both the ECAL and HCAL calorimeters will be driven by a control board (3CU). The purpose of this board is to process and send critical information (the clock, the slow control signals and the fast and synchronous command) received through optical fibres from the main LHCb system to the front-end boards. A total of 23 control boards including spares are needed for both the electromagnetic and hadronic calorimeters.

The LHCb operational master clock for data taking and the entire precise timing and synchronisation of the sub-detectors rely on the LHC bunch clock and the LHC orbit signal. The orbit signal marks each turn of the full LHC circulating bunch scheme (3563 steps). The readout supervisor system receives directly these two clocks from the RF-system of the LHC via an LHC Interface card located on the readout supervisor card. The LHC bunch clock is distributed to the front-end and readout boards with sufficiently low jitter (assumed for the moment to be $\mathcal{O}(10\text{ ps})$), and constant and reproducible phase. To ensure this low jitter requirement, a great care was needed in the design of the clock tree distribution within the board. The readout supervisor card distributes the clock and the Fast Control commands to the readout board, and

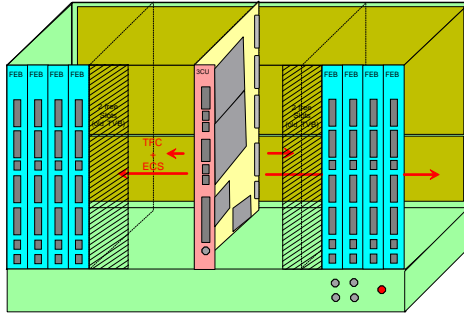


Figure 2.4: Schematic of a calorimeter crate.

the interface readout board distribute the clock and the Fast Control command to the control board.

The calorimeter crate mechanics are a standard 9U frame. They have two custom backplanes mounted in the back. The lower 3U backplane provides the power supplies, the Time Fast Control commands and the clock distribution. The upper 6U backplane is dedicated for the exchange of signals between the boards inside the crate and with the other crates. A calorimeter front-end crate contains up to 16 front-end boards which perform the acquisition of the detector channels, and in the middle of the crate, a reserved slot for the control board.

The main role of the control board is to receive the GBT (GigaBit Transceiver) frame through the optical link and to extract the information which is needed by the front end boards inside a same crate: the 40 MHz clock, the Time Fast Control (TFC) commands and Experiment Control System (ECS). Figure 2.5 shows a picture of the control board (3CU). The various parts of the board are clearly identified. The board contains :

- A Versatile Link Transceiver-Receiver (VTRx), for the reception and transmission to the SOL40 which an interface board that allows is to interface the fast and the slow control to the front-end boards.
- A radiation tolerant chip that can be used to implement multipurpose high speed (3.2-4.48 Gb/s user bandwidth) bidirectional optical links (GBTX).
- A GBT-SCA ASIC, part of the GBT chip-set, to distribute control and monitoring signals to the on-detector front-end electronics and perform monitoring operations of detector environmental parameters.
- A Microsemi FPGA (IGLOO2 family) which is in charge of the processing on the 3CU.

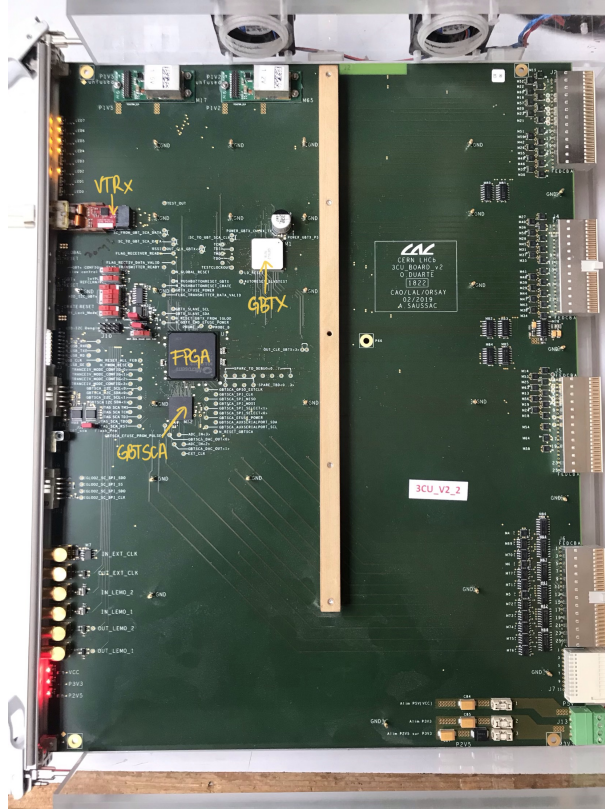


Figure 2.5: 3CU board.

Except for the commercial FPGA, the components listed above were designed at CERN and are shared across various sub-detectors in the LHCb upgrade. Following the clock and TFC command (or from left to right on the picture), first the 3CU receives the clock and the TFC command through the optical transmitter (VTRx) and decoding inside the GBTX. After processing inside the FPGA, the board transmits through the 3U backplane these signals to all the front-end boards inside the same crate.

A challenging aspect of the board was the design of the schematic for the PCB (Printer Circuit Board) especially around the GBTX component, where the density of extracted links is very high, about 300 out of the 400 of the GBTX pins.

Two prototypes of these boards are currently available in the lab in Orsay and have been validated, the final production of the board has been submitted.

The next steps will be to start testing the whole setup in a crate at CERN using the central acquisition system. Later, we will proceed to install and commission the electronics and ramp up for data taking.

Chapter 3

Allegro

*"Once you kill a cow,
you gotta make a burger"*

Lady Gaga

3.1 Dear b -baryons

The first observed baryon with a b -quark was the Λ_b^0 baryon (bud). This isospin-zero particle was discovered in $J/\psi \Lambda$ decays, at the UA1 detector in proton-antiproton collisions at CERN [51] and was later confirmed and studied by several experiments. Λ_b^0 particles are produced abundantly in the proton-proton collisions of the LHC, their production rate¹ relative to B -mesons is $f_{\Lambda_b^0}/(f_u + f_d) = 0.259 \pm 0.018$ [52].

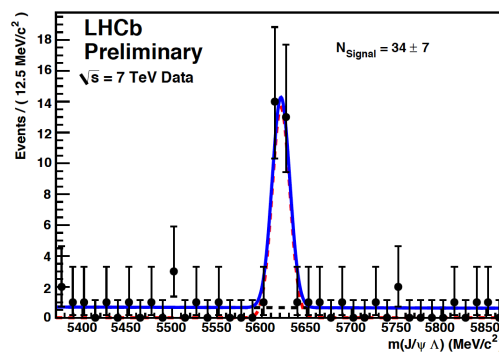


Figure 3.1: Most probably one of the first Λ_b^0 distributions seen at LHCb.

Figure 3.1 shows the $J/\psi \Lambda$ invariant mass using 5 pb^{-1} from the 2010 dataset, when a requirement on the decay time of the Λ_b^0 candidate to be higher than 0.3 ps is applied. I am particularly fond of this

¹In 13 TeV proton-proton collisions.

plot, because it was one of the first distribution of Λ_b^0 decays seen at LHCb and it really marked the start of my research activities with b -baryons. With more data, more b -baryons were seen and discovered, in particular I was involved in the studies of the Ξ_b^- and Ω_b^- baryons at LHCb. For what concerns NP searches, b -baryons allow to verify the anomalies in a different hadronic environment. Furthermore, since they carry half-integer spin, NP-sensitive observables which are not present in B -mesons can be measured in Λ_b^0 decays. Table 3.1 summarises the current experimental knowledge on the lightest b -baryons.

Table 3.1: Properties of the lightest b -baryon states. Based on Ref. [1].

Name	Quark content	Mass, MeV/ c^2	Lifetime or width	J^P	(I, I_3)	S
Λ_b^0	udb	5619.60 ± 0.17	1.470 ± 0.010 ps	$1/2^+$	$(0, 0)$	0
Ξ_b^0	usb	5791.9 ± 0.5	1.479 ± 0.031 ps	$1/2^+$	$(1/2, 1/2)$	-1
Ξ_b^-	dsb	5797.0 ± 0.9	1.571 ± 0.040 ps	$1/2^+$	$(1/2, -1/2)$	-1
Σ_b^+	uub	5810.55 ± 0.25	4.83 ± 0.48 MeV/ c^2	$1/2^+$	$(1, 1)$	0
Σ_b^0	udb	not yet observed		$1/2^+$	$(1, 0)$	0
Σ_b^-	ddb	5815.64 ± 0.28	5.33 ± 0.56 MeV/ c^2	$1/2^+$	$(1, -1)$	0
$\Xi_b'^0$	usb	not yet observed		$1/2^+$	$(1/2, 1/2)$	-1
$\Xi_b'^-$	dsb	5935.02 ± 0.05	< 0.08 MeV/ c^2	$1/2^+$	$(1/2, -1/2)$	-1
Ω_b^-	ssb	6046.1 ± 1.7	1.64 ± 0.18 ps	$1/2^+$	$(0, 0)$	-2
Σ_b^{*+}	uub	5830.28 ± 0.28	9.34 ± 0.54 MeV/ c^2	$3/2^+$	$(1, 1)$	0
Σ_b^{*0}	udb	not yet observed		$3/2^+$	$(1, 0)$	0
Σ_b^{*-}	ddb	5834.73 ± 0.30	10.68 ± 0.68 MeV/ c^2	$3/2^+$	$(1, -1)$	0
Ξ_b^{*0}	usb	5949.8 ± 1.4	0.90 ± 0.18 MeV/ c^2	$3/2^+$	$(1/2, 1/2)$	-1
Ξ_b^{*-}	dsb	5955.33 ± 0.13	1.65 ± 0.33 MeV/ c^2	$3/2^+$	$(1/2, -1/2)$	-1
Ω_b^{*-}	ssb	not yet observed		$3/2^+$	$(0, 0)$	-2

3.2 Mass measurements

My main collaborators for the measurements [53] discussed in this section were Sneha Malde and Matthew Needham. Within the SM of particle physics, mesons and baryons are colourless objects composed of quarks and gluons as discussed in Chapter 1. These systems are bound through the strong interaction, described by QCD. A basic property of hadrons that can be compared to QCD theoretical predictions is their masses. In 2008, there was the controversial discovery of the Ω_b^- first claimed by the $D\mathcal{O}$ experiment with $M(\Omega_b^-) = 6165 \pm 10(\text{stat}) \pm 13(\text{syst})$ MeV/ c^2 . A few months later the CDF collaboration also reported a measurement of the mass of this baryon $M(\Omega_b^-) = 6054.4 \pm 6.8(\text{stat}) \pm 0.9(\text{syst})$ MeV/ c^2 . Assuming the uncertainties to be uncorrelated across experiments, the difference between these two measurements, $111 \pm 12(\text{stat}) \pm 13(\text{syst})$ MeV/ c^2 , represents a discrepancy of more than six standard deviations. What was

particularly puzzling about the $D\bar{O}$ measurement is that it was in disagreement with the expectations of mass splittings inferred from quark model predictions of both beauty and charm particles. For example, as shown in Chapter 1, the theoretical predictions for the Ω_b^- mass are fairly broad, they lie in the range of 5940 - 6120 MeV/c^2 .

A key aspect of mass measurements is controlling the momentum scale of the experiment. A time-dependent momentum scale calibration procedure was used to “correct” the measured b -baryon masses [54].

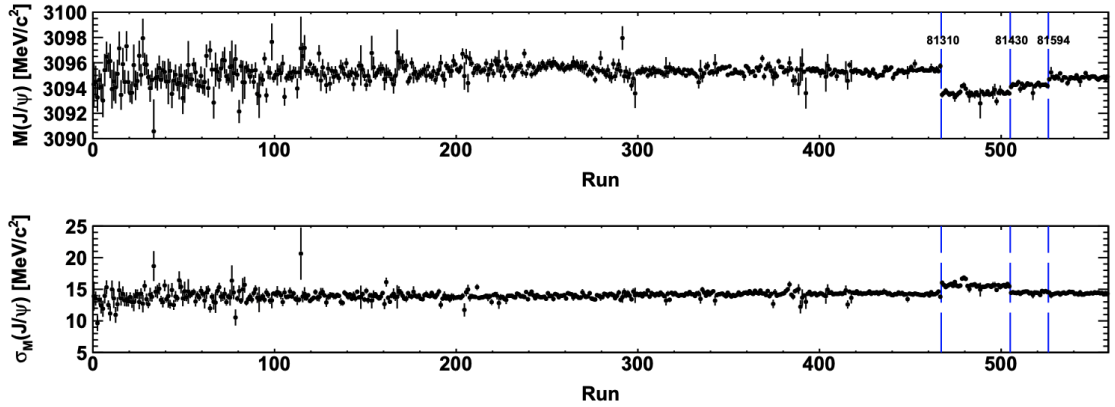


Figure 3.2: Measured $J/\psi \rightarrow \mu^+\mu^-$ mass (top) and resolution (bottom) as a function of run number during the entire 2010 data-taking period. The steps (indicated with vertical lines) correspond to the times when the TT operating temperature was altered.

The principles behind the momentum scale calibration can be described as follows. For a two-body decay $P \rightarrow c_1c_2$ relativistic mechanics gives:

$$m_{12}^2 = (E_1 + E_2)^2 - (\vec{p}_1 + \vec{p}_2) \cdot (\vec{p}_1 + \vec{p}_2). \quad (3.1)$$

It can be shown that if the momentum scale is wrong by a factor $(1-\alpha)$, the the measured mass m_{12} is given to first order in m/p by:

$$m_{12} = \frac{m_P^2 - f}{(1 - \alpha)^2} + f, \quad (3.2)$$

where

$$f = m_1^2 + m_2^2 + \frac{p_2}{p_1} m_1^2 + \frac{p_1}{p_2} m_2^2. \quad (3.3)$$

If $\alpha \ll 1$ this expression simplifies, to first order, to

$$\Delta m = \alpha \frac{f - m_P^2}{m_P} \quad (3.4)$$

where $\Delta m = m_P - m_{12}$. For decays of quarkonia or heavy hadrons where the mass of the final state particles can be neglected with respect to the parent particle, the correction needed can be written as:

$$\Delta m = -\alpha m_P. \quad (3.5)$$

A set of two-body decay modes was considered for the calibration of the momentum scale. The central value of the momentum scale is taken as the value of α extracted using $J/\psi \rightarrow \mu^+ \mu^-$ decays. An example of the trends is shown in Figure: 3.2.

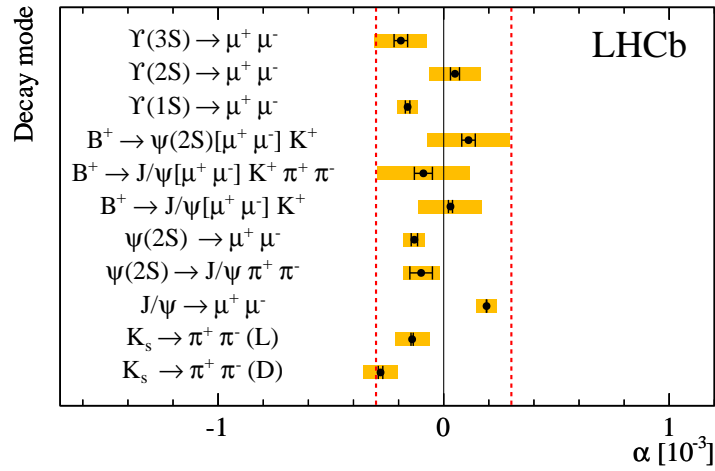


Figure 3.3: Average momentum scale bias α extracted from the reconstructed mass of various decay modes after the momentum calibration procedure. The K_s^0 decays are divided into two categories: those where the two child tracks have hits in the vertex detector (labelled L) and those without (labelled D). The black error bars represent the statistical uncertainty whilst the (yellow) filled areas also include contributions to the systematic uncertainty from the fitting procedure, the effect of QED radiative corrections, and the uncertainty on the mass of the decaying meson [1]. The (red) dashed line shows the assigned uncertainty of $\pm 0.03\%$ on the momentum scale.

To understand the odd behaviour in the trends (around Run 500), we relied on the log-books of the LHCb data shifter. We identified that it was due to a temperature variation of the TT tracker. To evaluate the impact of these variations, two versions of the detector alignment were tested, the standard one and one where the hits from the TT are systematically excluded from the track reconstruction. The whole exercise (track reconstruction, selection, mass fits) was repeated. Finally, the impact of the TT temperature variation was found not to be significant on the observables of interest, and no additional systematic uncertainty was assigned.

The systematic uncertainty on the momentum scale was taken as the difference between the values of α extracted from $J/\psi \rightarrow \mu^+ \mu^-$ and $K_s^0 \rightarrow \pi^+ \pi^-$ decays. The calibration was cross-checked using other

Table 3.2: Comparison of the b -baryon mass measurements using the full LHCb 2011 data sample with the single most precise results from the ATLAS [55], CDF [56, 57] and D0 [58, 59] collaborations, and with the PDG averages [60]. The PDG averages (2014) contain the results from CDF and D0 as well as the Λ_b^0 measurement from LHCb performed with the 2010 data sample. The quoted errors include statistical and systematic uncertainties. All values are in MeV/c^2 .

	$M(\Lambda_b^0)$	$M(\Xi_b^-)$	$M(\Omega_b^-)$
ATLAS	5619.7 ± 1.3	–	–
CDF	5619.7 ± 1.7	5790.9 ± 2.7	6054.4 ± 6.9
D0	–	5774 ± 19	6165 ± 16
PDG (2014)	5619.4 ± 0.7	5791.1 ± 2.2	6071 ± 40
LHCb	5619.5 ± 0.5	5795.8 ± 1.0	6046.0 ± 2.3

b -decay modes.

Figure 3.3 shows a summary of the momentum scale calibration. To measure the impact of systematic effects, the overall momentum scale was shifted by $\alpha = 0.5 \times 10^{-3}$ with little variation amongst the modes. The momenta of all the tracks used to form the b -baryon candidates are multiplied by $1 - \alpha$ before any mass constraint is applied, the uncertainty on the knowledge of α is later propagated to the final measurement as a systematic uncertainty on the mass measurements.

The decay modes employed to measure the masses of the Λ_b^0 , Ξ_b^- and Ω_b^- , were $J/\psi \Lambda$, $J/\psi \Xi(\rightarrow \Lambda \pi^-)$ and $J/\psi \Omega(\rightarrow \Lambda K^-)$ respectively. The Λ particle that decays to a pion and a proton travels a relatively long distance in the LHCb detector, $\mathcal{O}(\text{cm})$. The child tracks from the Λ baryon are referred to as long tracks if they leave energy deposits in the vertex locator or downstream tracks if they don't. To improve the resolution on the measured mass of the b -baryons by almost a factor two, a constraint on the known masses of the J/ψ and the Λ particles was systematically applied.

For these measurements simple cut-based selections relying on the kinematic properties of the final state particles and their identification probabilities were sufficient to select clean signal samples. The values of the masses were extracted from maximum likelihood fits to the invariant mass. The fit model was based on a Gaussian function to describe the signal and an exponential function to describe the combinatorial background. In the case of the Ω_b^- baryon, given the discrepancy which was observed between the previous measurements, the fitted value of the mass was kept blind throughout the analysis process, although not the mass distribution itself. The results are reported in Table 3.2.

To take into account the “look elsewhere effect”, the significance of the Ω_b^- signal was determined using a large number of pseudo-experiments with background only. For each pseudo-experiment a sample of mass

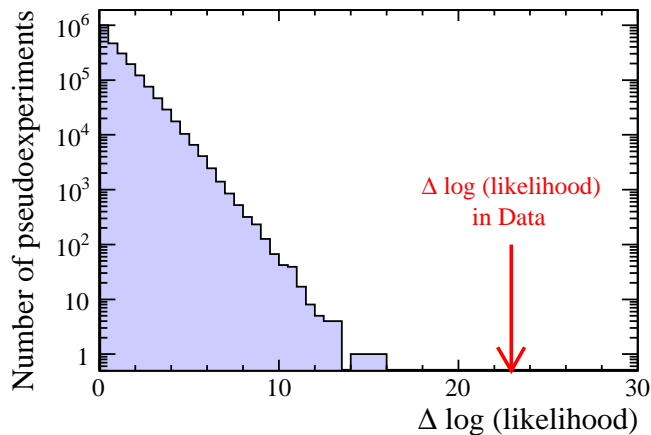


Figure 3.4: Distribution of the negative log-likelihood difference $\ln(\mathcal{L}_{\max}/\mathcal{L}_0)$ in 2.5×10^6 pseudo-experiments with background only. The red arrow corresponds to the value observed in the data.

values with the same size as the data sample is generated using the exponential background distribution determined from the fit to the data candidates. We determined the probability that, in these pseudo-experiments, any signal seen in the mass range $5.8\text{--}6.3 \text{ GeV}/c^2$ would lead to a value of $\ln(\mathcal{L}_{\max}/\mathcal{L}_0)$ larger than in the data, and interpret it as the probability that the observed Ω_b^- peak in the data is due to a statistical fluctuation of the background. The distribution of $\ln(\mathcal{L}_{\max}/\mathcal{L}_0)$, determined with 2,500,000 pseudo-experiments, is shown in Figure 3.4. The fact that no pseudo-experiment yields a value larger than the data suggests a p -value smaller than 4×10^{-7} , which translates to a statistical significance consistent with 6.8σ .

The LHCb collaboration measured the Ω_b^- mass, using the hadronic final state $\Omega_c^0 (\rightarrow pKK\pi)\pi$ [61]. The result was found to be in agreement with the measurement discussed in this section and the result from CDF. The measurement from the DØ experiment is no longer taken into account in the PDG averages [1]. Spectroscopy and mass measurements have a bright future at LHCb, the first observation of Ω_b^- baryon excited states was reported recently in Ref. [62].

3.3 Lifetime measurements

My main collaborators on the lifetime measurements [63] were Francesca Dordei and Greig Cowan. Lifetime measurements are often considered to be the “bread & butter” of a flavour experiment. Whoever thinks this should be sent to jail. The analysis discussed in this section grouped many b -hadrons. The decays of these hadrons all shared $J/\psi X$ topologies displayed in Figure 3.5, where X was required to be K^+ , K_S^0 , K^{*0} , ϕ or

a Λ . Thanks to the clean dimuon signatures of these decays and the usage of mass constraints on the known

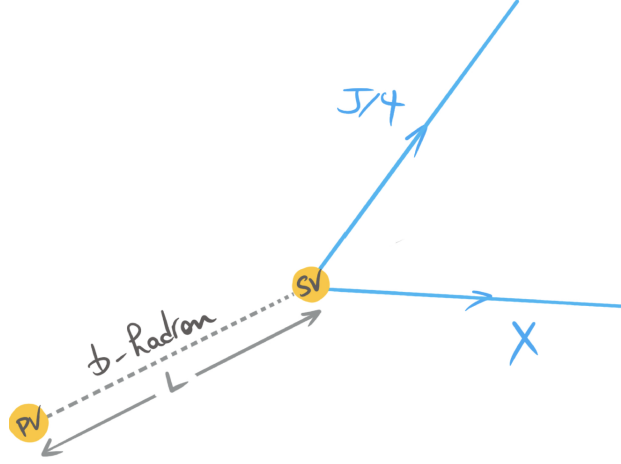


Figure 3.5: Sketch of the decay of a b -hadron to a J/ψ and an additional particle X . The b -hadron is produced at the primary vertex (PV) and it decays at the decay vertex (SV). The length L is the spatial separation between the two vertices.

values mass of the J/ψ , K_S^0 and Λ particles, simple cut-based selections were found to be sufficient to select all the signals. Furthermore, cut-based selections were even favoured to more sophisticated multivariate ones, since we were trying to track down all the possible sources of biases that might influence the measured lifetimes. The decay time, t , of a particle in its rest frame, can be computed as follows:

$$t = L \frac{m}{|\vec{p}|} \quad (3.6)$$

where L is the flight distance travelled by the b -hadron, p is the reconstructed three-momentum and m its reconstructed mass.

Two approaches were used to access the observable of interest. The first one was based on a two-dimensional likelihood fit to the invariant mass and decay time of the b -hadron. In the second approach, s Weights [64] were extracted from a fit to the invariant mass distribution and exploited to subtract the background components from the lifetime distributions, which were then fitted. While doing the analysis it was thought to be very useful to have two methods for cross-checks.

The signal probability density function used in the lifetime fit to extract the observable of interest τ_{H_b} can be written as follows:

$$[e^{(t'/\tau_{H_b})} \otimes \mathcal{R}(t, t')] \times \text{Acc}(t) \quad (3.7)$$

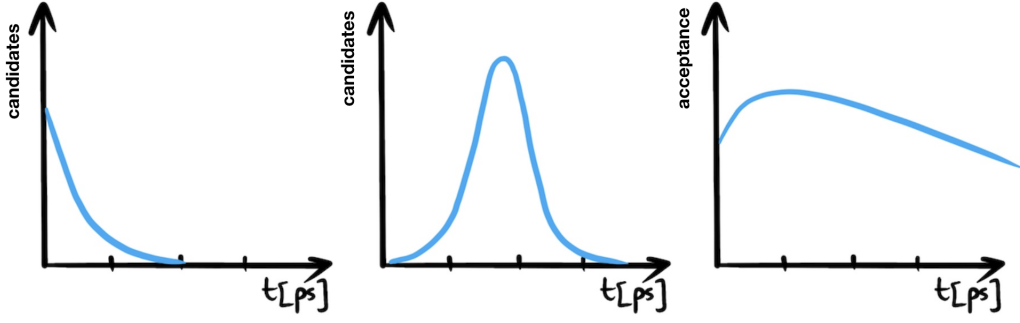


Figure 3.6: Sketch of a decay-time distribution, decay-time resolution and decay-time acceptance of a b -hadron (x -axes not to scale).

A sketch of a typical shape of the decay time resolution (\mathcal{R}) and the decay time acceptance (Acc) are shown in Figure 3.6. Given that the expected statistical uncertainty for these measurements was around a few femtoseconds, it was mandatory to have a very good control of the acceptance effects in particular. The decay-time resolution was measured using data. At the start of the LHCb data taking, large samples of “prompt- J/ψ ” decays were recorded with dedicated trigger lines. Given that they were produced at zero lifetime, the width of their decay time distribution was dominated by the decay time resolution. Typical values of the decay time resolution for these decay modes was about 50 fs.

Understanding the decay-time acceptances turned out to be a tricky job. Figure 3.7 displays the breakdown of all the effects entering the decay-time acceptance seen in Λ_b^0 decays. When we first started to test the fitting procedure using simulated samples, on which the full reconstruction and event selection was applied, biases up to 18 fs were observed for the decay modes where all the tracks were decaying inside the vertex locator. The biases were smaller ~ 10 fs for decays with long-lived particles (K_S^0 and Λ). This observation allowed to point towards effects coming from the vertex locator reconstruction. And indeed, an assumption that the tracks were produced in a region close to the interaction region was used in the pattern recognition algorithms. This assumption was the main cause for the “upper lifetime” acceptance. Since this was the start of LHCb data taking and the time-dependent analyses did not have the maturity that they have now, we did not feel comfortable to simply plug whatever bias was measured from simulation into the data fit. We developed a data-driven method to address this point. A large sample of $B^+ \rightarrow J/\psi K^+$ decays was used where the kaon was reconstructed without using the information from the vertex locator². For the purpose of these studies, we reprocessed both the data and simulation samples using the downstream tracking on the kaon. The vertex locator reconstruction efficiency was then computed using a tag-and-probe technique.

²The K was reconstructed using only the downstream tracking.

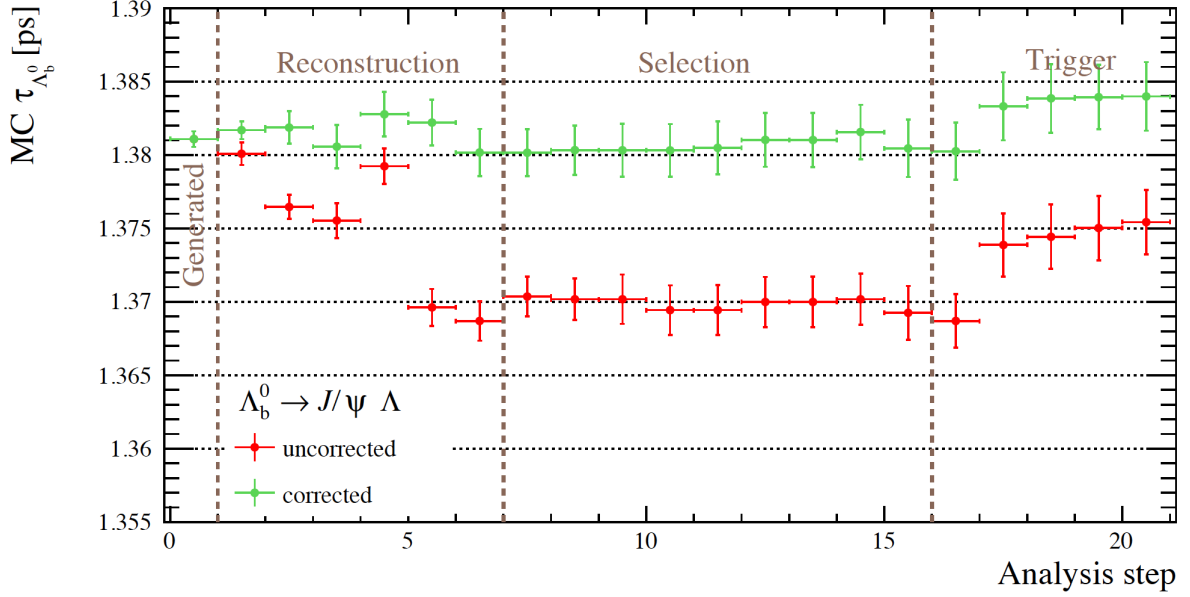


Figure 3.7: Λ_b^0 acceptance steps as a function of the different reconstruction, selection and trigger requirements in the analysis.

A parametrisation based on the distance of closest approach of one of the final state particles allowed to model the efficiency of this algorithm on data. This parametrisation took into account the different tunings of the reconstruction in the trigger and offline, as well as correlations between tracks. Weights were extracted from the vertex locator reconstruction efficiency distribution and applied to the signal candidates in data to correct for this effect.

The remaining effects that contributed to the decay time acceptances were: the position of the primary vertex, the vertex quality of the fit which was worse for tracks with a small opening angle (for example $\phi \rightarrow K^+ K^-$), a requirement on the displacement of the J/ψ from the primary vertex in the software trigger and in the stripping selection.

The absolute lifetimes of the b -hadrons are reported in Table 3.3. Besides the Λ_b^0 measurement all the others were the world's best measurements.

The early measurements of the ratio of Λ_b^0 to B^0 lifetimes were mainly driven by the Tevatron, and gave results which were considerably smaller than the theoretical expectation [22, 65, 66]. It was considered for a while by the theory community that additional operators should be included in the description of the Λ_b^0 amplitude to account for these differences. However, today the combined measurement of the Λ_b^0 lifetime from LHCb, $1.468 \pm 0.009 \pm 0.008$ ps is in agreement with most of the predictions from HQET [19]. With work, it is fair to say that we closed the Λ_b^0 lifetime saga.

Table 3.3: Fit results for the B^+ , B^0 , B_s^0 mesons and Λ_b^0 baryon lifetimes. The first uncertainty is statistical and the second is systematic.

Lifetime	Value [ps]
$\tau_{B^+ \rightarrow J/\psi K^+}$	$1.637 \pm 0.004 \pm 0.003$
$\tau_{B^0 \rightarrow J/\psi K^{*0}}$	$1.524 \pm 0.006 \pm 0.004$
$\tau_{B^0 \rightarrow J/\psi K_S^0}$	$1.499 \pm 0.013 \pm 0.005$
$\tau_{\Lambda_b^0 \rightarrow J/\psi \Lambda}$	$1.415 \pm 0.027 \pm 0.006$
$\tau_{B_s^0 \rightarrow J/\psi \phi}$	$1.480 \pm 0.011 \pm 0.005$

The cherry on the cake from this analysis, was that the lifetimes of $B^0 \rightarrow J/\psi K^{*0}$ and $B^0 \rightarrow J/\psi K_S^0$ decays were used to measure $\Delta\Gamma_d/\Gamma_d$ as suggested in Ref. [67]. Flavour-specific final states such as $B^0 \rightarrow J/\psi K^{*0}$ have $\mathcal{A}_{\Delta\Gamma_d}^{B^0 \rightarrow J/\psi K^{*0}} = 0$, while $\mathcal{A}_{\Delta\Gamma_d}^{B^0 \rightarrow J/\psi K_S^0} = \cos(2\beta)$ to a good approximation in the SM, where for a given final state f :

$$\mathcal{A}_{\Delta\Gamma_d}^f = \frac{2\text{Re}(\lambda_f)}{1 + |\lambda_f|^2}, \quad \text{and} \quad \lambda_f = \frac{q}{p} \frac{\bar{A}_f}{A_f} \quad (3.8)$$

where, parameters \bar{A}_f and A_f are the complex amplitudes for the decay of a \bar{B}^0 and B^0 to the final state f , respectively, and $\beta \equiv \arg[-(V_{cd}V_{cb}^*)/(V_{td}V_{tb}^*)]$ is one of the CKM unitarity triangle angles [26]. Hence, the two effective lifetimes can be expressed as

$$\tau_{B^0 \rightarrow J/\psi K^{*0}} = \frac{1}{\Gamma_d} \frac{1}{1 - y_d^2} (1 + y_d^2), \quad (3.9)$$

$$\tau_{B^0 \rightarrow J/\psi K_S^0} = \frac{1}{\Gamma_d} \frac{1}{1 - y_d^2} \left(\frac{1 + 2 \cos(2\beta)y_d + y_d^2}{1 + \cos(2\beta)y_d} \right). \quad (3.10)$$

Using the effective lifetimes reported in Table 3.3 and $\beta = (21.5_{-0.7}^{+0.8})^\circ$ [26], a fit of $\Delta\Gamma_d$ and Γ_d to the expressions in Eq. (3.9) and Eq. (3.10) leads to

$$\Gamma_d = 0.656 \pm 0.003 \pm 0.002 \text{ ps}^{-1}, \quad (3.11)$$

$$\Delta\Gamma_d = -0.029 \pm 0.016 \pm 0.007 \text{ ps}^{-1}, \quad (3.12)$$

where the first uncertainty is statistical and the second is systematic. The correlation coefficient between $\Delta\Gamma_d$ and Γ_d is 0.43 when including statistical and systematic uncertainties. The combination gives

$$\frac{\Delta\Gamma_d}{\Gamma_d} = -0.044 \pm 0.025 \pm 0.011, \quad (3.13)$$

consistent with the SM expectation: $40.9_{-9.9}^{+8.9} \times 10^{-4}$ [68, 69] and the current world-average value [26].

3.4 Lepton universality test

In this section, I will discuss the first test of lepton universality measurement with b -baryons from Ref.[70]. This measurement was the PhD thesis of Vitalii Lisovskyi [71] whom I co-supervised together with Marie-Hélène. We were then joined by Carla Marin Benito who is funded by the ANR BACH project.

In the SM the couplings of the W and Z bosons to all charged lepton species are identical and a large number of experiments where the electroweak bosons are directly produced have tested this property. The LEP measurements of the $Z \rightarrow e^+e^-$, $Z \rightarrow \mu^+\mu^-$ and $Z \rightarrow \tau^+\tau^-$ partial widths are in very good agreement with each other [72]:

$$\frac{\Gamma(Z \rightarrow \mu^+\mu^-)}{\Gamma(Z \rightarrow e^+e^-)} = 1.0009 \pm 0.0028. \quad (3.14)$$

$$\frac{\Gamma(Z \rightarrow \tau^+\tau^-)}{\Gamma(Z \rightarrow e^+e^-)} = 1.0019 \pm 0.0032. \quad (3.15)$$

In addition to the measurement at the Z pole, a good agreement was also found in the LHC measurements [73]. A detailed review of further LU tests with W bosons, as well as in light pseudo scalar mesons can be found in Ref. [74]. Under the assumption of LU, all the decay widths of the Z boson decay to leptons are expected to be equal in the SM.

As it was shown in the previous sections, Λ particles have a rather long lifetime and a lower reconstruction efficiency in comparison to particles produced close to the interaction point. Therefore, the overall yields of $\Lambda_b^0 \rightarrow \Lambda \ell^+ \ell^-$ decays were expected to be smaller than $\Lambda_b^0 \rightarrow pK \ell^+ \ell^-$ decays. This is what motivated the choice of this particular decay for the LU test. Table 3.4 summarised the current experimental knowledge on Λ_b^0 baryon to pKX final states. What can be seen is that at the time when this analysis started only the branching fraction of the decays to charmonia decays were known. The pK resonant structure was resolved only for the J/ψ mode³, as shown in Figure 3.8.

Table 3.4: Status of the decay modes of interest of the Λ_b^0 baryon before the work discussed in this section.

Decay mode	Observed	Published	BR measured	Refs.
$\Lambda_b^0 \rightarrow pK\mu^+\mu^-$	Yes	Yes	No	[75]
$\Lambda_b^0 \rightarrow pKe^+e^-$	No	No	No	N/A
$\Lambda_b^0 \rightarrow pKJ/\psi$	Yes	Yes	$(3.17 \pm 0.04_{-0.45}^{+0.57}) \times 10^{-4}$	[76]
$\Lambda_b^0 \rightarrow pK\psi(2S)$	Yes	Yes	$(6.6_{-1.0}^{+1.2}) \times 10^{-5}$	[77]
$\Lambda_b^0 \rightarrow pK\gamma$	(Yes)	No	No	N/A

³This analysis that led to the discovery of the states compatible with pentaquark particles.

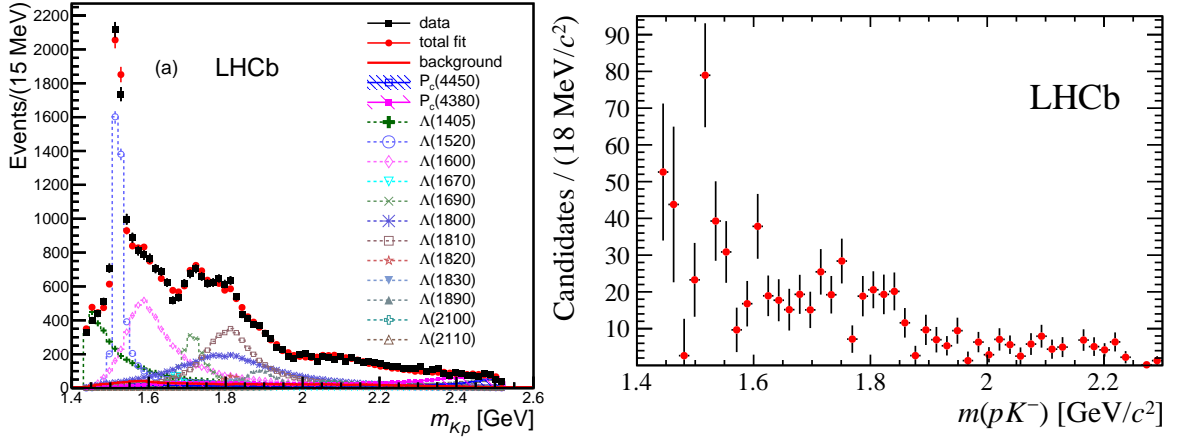


Figure 3.8: Invariant mass of $m(pK)$ in $\Lambda_b^0 \rightarrow pK J/\psi$ (left) and $\Lambda_b^0 \rightarrow pK \mu^+ \mu^-$ (right) data. Figures taken from and Ref. [78] Ref. [75] respectively.

The identification of electrons is peculiar with respect to the other charged tracks in the LHCb detector. Electrons⁴ emit bremsstrahlung radiation when they interact with the material in the detector. This radiation is emitted colinearly to the electron direction. This effect will have an impact on the electron momentum estimate. If the bremsstrahlung photon is emitted before the magnet, it will continue its path in the original direction of the electron, while the electron will be bent in the magnet. Hence the electron and the photon will not be absorbed in the same cells of the electromagnetic calorimeter. The measured momentum of the electron is lower given that it lost some of its energy to the photon. In this configuration the emitted bremsstrahlung does not affect the measured ratio E/p used in the electron identification. If on the other hand the photon is emitted after the magnet, but before the electromagnetic calorimeter, the momentum of the electron has already been estimated. The photon and the electron end up in the same cell. Hence their combined energy release provides the original electron energy and here also E/p is not affected.

In order to account for the bremsstrahlung effects, dedicated algorithms are used inside the LHCb reconstruction algorithms to correct for them. One of the main impacts of the bremsstrahlung radiation is the very striking and non-trivial shape of the b -hadron invariant mass distribution. Typically, three⁵ bifurcated Crystal-Ball functions are necessary to describe the shapes decays involving electrons like $B^+ \rightarrow K^+ e^+ e^-$, $B^0 \rightarrow K^{*0} e^+ e^-$ or $\Lambda_b^0 \rightarrow pK e^+ e^-$. Furthermore, because of the worse overall mass resolution with respect to muon modes, great care is needed to model the partially reconstructed backgrounds which populate the

⁴The average transverse momentum of electrons from b -decays is a couple of GeV.

⁵One per bremsstrahlung category.

left hand side of the invariant mass distributions. These distributions were quite a change of scenery to me, given that I was used to very clean dimuon signatures. The observable of interest R_{pK}^{-1} can be written

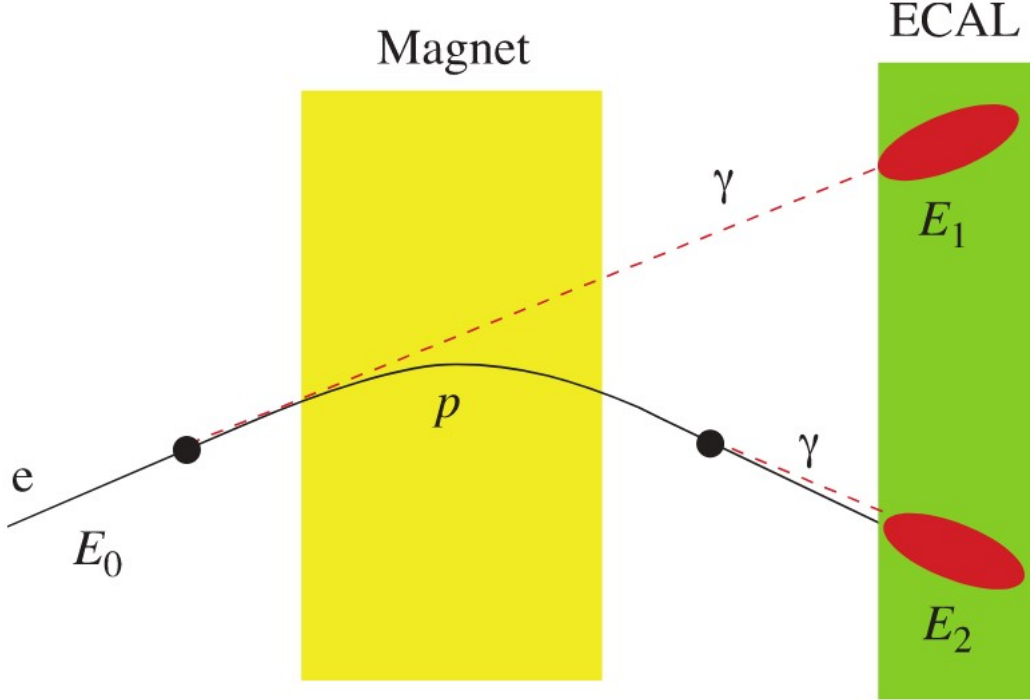


Figure 3.9: Illustration of the bremsstrahlung photons emitted by an electron before and after the magnet.

as:

$$R_{pK}^{-1} = \frac{BR(\Lambda_b^0 \rightarrow pK e^+ e^-)}{BR(\Lambda_b^0 \rightarrow pK \mu^+ \mu^-)} \times \frac{BR(\Lambda_b^0 \rightarrow pK J/\psi (\rightarrow \mu^+ \mu^-))}{BR(\Lambda_b^0 \rightarrow pK J/\psi (\rightarrow e^+ e^-))}. \quad (3.16)$$

It is defined this way to ensure the best possible cancellation of effects that can be introduced by the differences in the treatment of reconstruction effects between muons and electrons. For example, the universality of the J/ψ decays which has been already tested very precisely:

$$\frac{\Gamma_{J/\psi \rightarrow e^+ e^-}}{\Gamma_{J/\psi \rightarrow \mu^+ \mu^-}} = 1.0016 \pm 0.0031, \quad (3.17)$$

is used to evaluate R_{pK}^{-1} as a double ratio rather than a more obvious single ratio.

One of the most frequent questions that the proponents of the analysis and myself received since the publication of our results is: “Why did you measure R_{pK}^{-1} and not R_{pK} ?”. The answer to this question is illustrated in Figure 3.10 which indicates better behaviour of the log-likelihood profile for R_{pK}^{-1} with respect to R_{pK} . This effect is driven by the fact that a log-likelihood profile will be more Gaussian if the smaller number (the electron yield in our case) is at the numerator rather than the denominator. The first R_K

and R_{K^*0} measurements were done at the B -factories where the overall yields of the electron and muon rare modes were of about the same size and this particular point was not as relevant for them.

The R_{pK}^{-1} analysis was performed in trigger categories. Indeed it was shown that the kinematics of the decay vary depending on whether the candidates were triggered by the hardware trigger based on the electromagnetic calorimeter or by the “other” particles in the event. In the jargon of LHCb, this classification is called TIS for Triggered Independently of the Signal and this was the prime category for the electron channel, or TOS for Trigger On Signal and this was the second category. In our construction these two categories were exclusive. For decays involving muons in the final state, only one trigger category based on the information from the muon stations in the hardware level was used.

To reduce the combinatorial background, multivariate approaches based on boosted-decision trees were employed. The algorithms were trained on simulated signal samples which were reweighed to account for differences between data and simulation. The background samples were obtained from the upper side bands of the invariant mass data distribution and k -folding was used to avoid biases in the training phase.

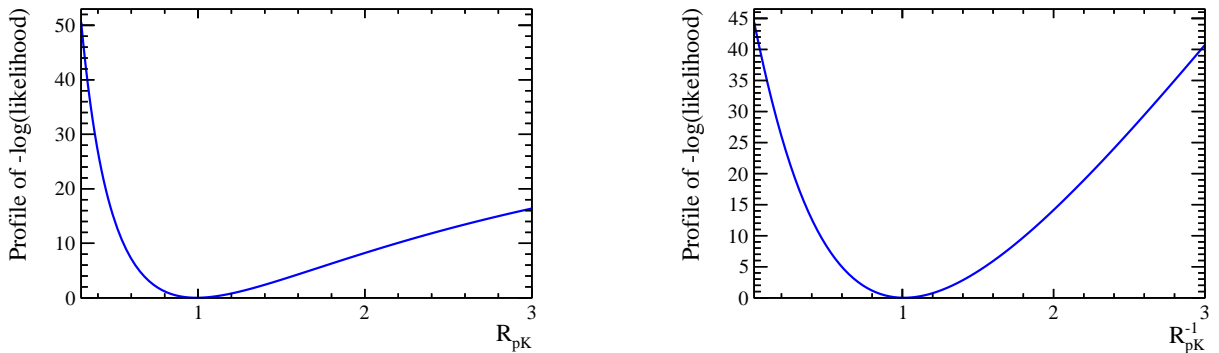


Figure 3.10: Log-likelihood profile for R_{pK} (left) and R_{pK}^{-1} (right) using “fake” efficiency to constrain the central value to be equal to unity.

Requirements based on the particle identification probabilities were applied to all the tracks to reduce the backgrounds originating from hadron mis-identification. The remaining components were then later taken into account in the fit to the invariant mass distributions.

Besides these sources of background, one has to take into account backgrounds from cascade decays. The branching fraction of $b \rightarrow c \ell \nu$ decays is typically three orders of magnitude larger than the $b \rightarrow s$ one. These types of backgrounds are not relevant in the cases where the leptons decay via a resonance like the J/ψ .

Dedicated vetoes were setup to suppress some of them, the remaining events are then modelled in the fit

or taken into account as part of the systematic studies.

One of the most important aspects of a LU test is to ensure a good control of the efficiencies; this was achieved as stated earlier thanks to the evaluation of the ratio $r_{J/\psi}^{-1}$ computed as:

$$r_{J/\psi}^{-1} = \frac{N(\Lambda_b^0 \rightarrow pKJ/\psi (\rightarrow e^+e^-))}{N(\Lambda_b^0 \rightarrow pKJ/\psi (\rightarrow \mu^+\mu^-))} \times \frac{\epsilon(\Lambda_b^0 \rightarrow pKJ/\psi (\rightarrow \mu^+\mu^-))}{\epsilon(\Lambda_b^0 \rightarrow pKJ/\psi (\rightarrow e^+e^-))}. \quad (3.18)$$

The aim of this stringent test is to make sure that this ratio is equal to unity and flat across phase-space. The simulation is known not to be a perfect description of the data. A set of “corrections” derived from data are applied to the simulation to account for these differences. They are based on the kinematics and decay model of the Λ_b^0 particle but also on the multiplicity of the events. The $r_{J/\psi}^{-1}$ test was performed separately for each of the trigger categories and data taking periods.

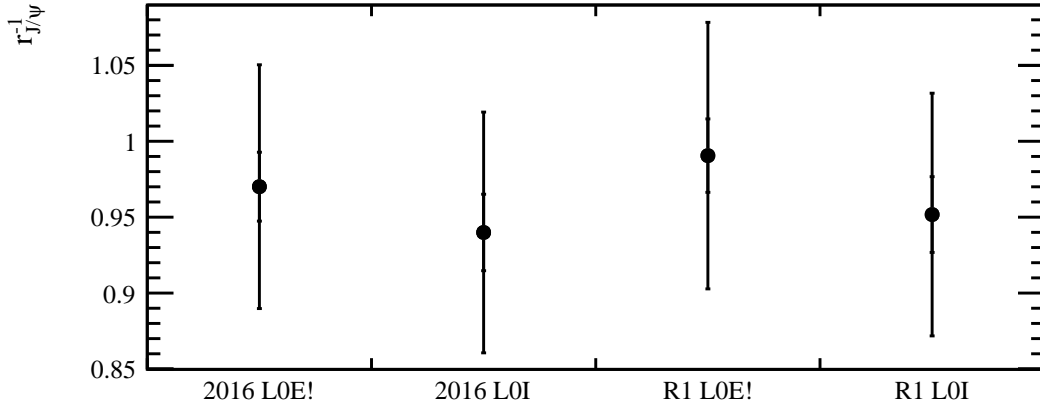


Figure 3.11: Comparison of unblinded $r_{J/\psi}^{-1}$ values in different trigger categories and datasets, with total and statistical-only uncertainties displayed.

The procedure described below to measure $r_{J/\psi}^{-1}$ is identical between the datasets, with the only difference arising from selection requirements and weights applied to the simulation.

1. The $\Lambda_b^0 \rightarrow pKJ/\psi (\rightarrow \mu^+\mu^-)$ generator-level simulation sample, with the relevant weights applied, is used to extract the number of simulated events at the generator stage.
2. The $\Lambda_b^0 \rightarrow pKJ/\psi (\rightarrow \mu^+\mu^-)$ reconstructed-level simulation sample, processed through the complete chain of selection requirements, and having all the relevant weights applied, is used to extract the number of simulated events after the final selection.
3. The number of reconstructed-level events (step 2) is divided by the number of generated-level events

(step 1), and multiplied by the values of generating and filtering efficiencies, to get the total efficiency.

4. For Run I, the 2011 and 2012 datasets have to be merged. To do so, their simulation samples are merged, having a dedicated weight applied ensuring the correct ratio of integrated luminosity (1:2) between the two datasets. In addition, the ratio of Λ_b^0 production cross-sections at 8 and 7 TeV is taken to be 1.23, as per the LHCb measurement [76]. The relevant values of generation and filtering efficiencies are passed to each of the two datasets. Steps 1 and 2 are performed with already merged generator-level and reconstruction-level samples.
5. The simulation samples of the specific backgrounds, with the final selection applied, are used to extract their invariant mass shapes.
6. The $\Lambda_b^0 \rightarrow pKJ/\psi(\rightarrow \mu^+\mu^-)$ simulation sample is used to extract the signal invariant mass shape.
7. The fit is performed to the $\Lambda_b^0 \rightarrow pKJ/\psi(\rightarrow \mu^+\mu^-)$ data, with the final selection applied. The signal yield and its uncertainty are extracted from the fit.
8. The signal yield is divided by the total efficiency (step 3) to obtain the efficiency-corrected yield.
9. All the previous steps are repeated for the $\Lambda_b^0 \rightarrow pKJ/\psi(\rightarrow e^+e^-)$ mode.
10. Efficiency-corrected yields of the $\Lambda_b^0 \rightarrow pKJ/\psi(\rightarrow e^+e^-)$ are divided by the efficiency-corrected $\Lambda_b^0 \rightarrow pKJ/\psi(\rightarrow \mu^+\mu^-)$ yields to get the value of $r_{J/\psi}^{-1}$.

Comparisons of $r_{J/\psi}^{-1}$ between trigger categories and datasets are shown in Fig. 3.11. The uncertainties displayed are statistical uncertainties only. Getting $r_{J/\psi}^{-1}$ “right” as a function of phase-space, $r_{J/\psi}^{-1} = 0.96 \pm 0.05$, took the best part of a year of Vitalii’s PhD.

Finally, R_{pK}^{-1} is measured using a simultaneous fit to both $\Lambda_b^0 \rightarrow pK\mu^+\mu^-$ and $\Lambda_b^0 \rightarrow pKe^+e^-$ decay modes, using all available data sets and trigger categories. The yields of the control modes and the efficiencies are measured beforehand and are plugged as Gaussian constraints in the fit. The fit has two observables, R_{pK}^{-1} and $r_B = \mathcal{B}(\Lambda_b^0 \rightarrow pK\mu^+\mu^-)/\mathcal{B}(\Lambda_b^0 \rightarrow pKJ/\psi(\rightarrow \mu^+\mu^-))$. The branching fraction of the rare electron mode is later derived as a byproduct of the simultaneous fit.

The result of the test of LU in $\Lambda_b^0 \rightarrow pK\ell^+\ell^-$ decays, R_{pK}^{-1} , in the range $0.1 < q^2 < 6 \text{ GeV}^2/c^4$ and $m(pK^-) < 2600 \text{ MeV}/c^2$ is

$$R_{pK}^{-1} \Big|_{0.1 < q^2 < 6 \text{ GeV}^2/c^4} = 1.17^{+0.18}_{-0.16} \pm 0.07,$$

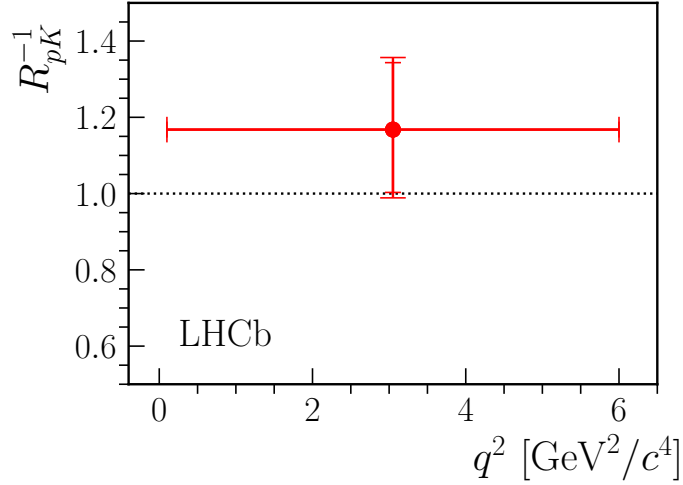


Figure 3.12: Measured value of R_{pK}^{-1} in the range $0.1 < q^2 < 6 \text{ GeV}^2/c^4$ and $m(pK^-) < 2600 \text{ MeV}/c^2$ (red point), including statistical and systematic uncertainties, compared to unity (dashed line).

where the first uncertainty is statistical and the second systematic.

The first measurement of the branching fraction of the rare muonic decay mode $\Lambda_b^0 \rightarrow pK\mu^+\mu^-$ is also performed and its value is found to be $\mathcal{B}(\Lambda_b^0 \rightarrow pK\mu^+\mu^-)|_{0.1 < q^2 < 6 \text{ GeV}^2/c^4} = (2.65 \pm 0.14 \pm 0.12 \pm 0.29_{-0.23}^{+0.38}) \times 10^{-7}$.

The electron mode $\Lambda_b^0 \rightarrow pKe^+e^-$ is observed for the first time $\mathcal{B}(\Lambda_b^0 \rightarrow pKe^+e^-)|_{0.1 < q^2 < 6 \text{ GeV}^2/c^4} = (3.1 \pm 0.4 \pm 0.2 \pm 0.3_{-0.3}^{+0.4}) \times 10^{-7}$, with a significance larger than 7σ including systematic uncertainties.

To conclude, more data are needed to confirm or exclude the presence of NP contributions in these decays. It should be noted that the current analysis is sensitive to different experimental uncertainties than those of lepton-universality tests performed with B mesons, such as the backgrounds that affect the extraction of the signal yields from data, or the control modes which are used to calibrate the simulation and measure the double ratio. Consequently, it provides an independent test of the SM.

Finally, the prospects for $b \rightarrow s\ell^+\ell^-$ decays with the LHCb Upgrades are very exciting. The statistical uncertainties will be significantly reduced, so that with 23 fb^{-1} we expect to reach about 0.025, 0.031 and 0.076 precision on R_K , R_{K^*0} and R_{pK} respectively [79]. It will also be possible to investigate new b -decay modes, and especially to explore angular observables, to probe directly the Wilson coefficients and who knows maybe discover New Physics ?

Chapter 4

Conclusion

*\Que mon conte soit beau et se
deroule comme un long l"*

Marie Louise Taous Amrouche

Le grain magique

I had the good fortune to contribute to a few, yet very diverse facets of flavour physics, as well to the LHCb detector and its first upgrade. The months ahead of us are extremely important, as we are about to embark in the commissioning of an almost whole new detector, while working on the analysis of the legacy datasets and preparing LHCb upgrade II. Truly someday, it seems like a titanic work. However, the excitement and the myriad of possibilities from flavour physics are such, that I believe all the efforts are worth it (although to be honest, sometimes after sitting in four or five hours long meetings, discussing the impact of the phases of the moon on our measurements of detector designs, I do think that all of it should be tossed out a window).

The results presented in this habilitation explored different properties of b -baryons. To achieve precise mass measurements of the Λ_b^0 , Ξ_b and Ω_b^- baryons, it was shown that a good control and understanding of the momentum scale played an essential role. The Ω_b^- measurement allowed to clarify the observed discrepancy between the two previous measurements from the Tevatron. I then proceeded to discuss lifetime measurements of the b -hadrons using decay modes with J/ψ in the final state. Given the size of the statistical uncertainties, it was mandatory to have an excellent handle on the systematic uncertainties. With this analysis, lifetime acceptance effects were broken down as much as physically possible. Data-driven methods were employed to estimate the impact of reconstruction effects. The results were in good agreement with the theoretical prediction from HQET and contributed to significantly reduce the uncertainty of the updated world averages. Finally, I discussed the first test of lepton universality using

Λ_b^0 decays, R_{pK}^{-1} . With this analysis, the first observation of the rare mode $\Lambda_b^0 \rightarrow pK e^+ e^-$ was established as well as the measurement of the branching fraction of $\Lambda_b^0 \rightarrow pK e^+ e^-$ in $q^2 \in [1, 6] \text{ GeV}^2/c^4$ and $m_{pK} < 2600 \text{ MeV}/c^2$. A key aspect of this analysis relies on the computation of the observable $r_{J/\psi}^{-1}$ which gives confidence in the good control of the reconstruction effects and expected differences between electrons and muons. While this is statistically limited, it follows the same trend observed in lepton universality tests performed with other B -mesons. With this measurement, we did not close the window on the anomalies, so let us see if they will remain and lead to the discovery of new particles, or fade away with more data.

To conclude, the experimental measurements of b -baryon properties contributed to the understanding or validation of theoretical computations. However, there are still plenty of measurements to be done and phenomena to be further investigated, and I am looking forward to doing so in LHCb in the next few years.

Apprentices

An HDR would make little to probably no sense without the participation of students. I had the pleasure to supervise and co-supervise many bachelor (L3) and master (M1 or M2) students since I started working at CNRS in 2012. I don't mention in this section the contribution of my PhD students Renato Quagliani and Vitalii Lisovskyi as they each produced almost 300 pages of material describing their work [48], [71]. They all played very different roles and contributed to many areas of my research activities for example, they helped me to kick-start physics analyses, learn new techniques, methods or software, study the feasibility of a measurement, address a specific analysis point. I would like to thank all of them for their enthusiasm and energy. I would like also to thank Carla Marin Benito & Sébastien Descotes-Genon who shared some of the supervision with me.

Kevin de Vasconcelos Corga 2013/M1

With Kevin we evaluated the expected statistical uncertainty on $\Delta\Gamma_d$ and τ_{B^0} using LHCb 2011 and 2012 datasets. Kevin wrote a new fitting program which permitted to access the observables of interest in a simultaneous way from $B^0 \rightarrow J/\psi K_S^0$ and $B^0 \rightarrow J/\psi K^{*0}$ signal events. He also made an extrapolation for the LHCb Upgrade. For this study, there was no special treatment of the K_S^0 tracks, both types of track categories were accounted for and each of them had their own decay time acceptance.

Ilham Dami 2015/L3

With Ilham we stated the lepton universality analysis with Λ_b^0 decays. During her internship, Ilham studied the shape of the rare electron mode using simulated samples of $\Lambda_b^0 \rightarrow \Lambda(1520)e^+e^-$ decays. We also had a

look at multivariate selections for this decay mode, she used the scikit learn software and we played with the various algorithms and optimisation techniques [80].

Rabah Abdul Khalek 2016/M1

Rabah's internship happened during a time where I was working on the software of the scintillator fibre tracker for the LHCb Upgrade. Trying to reduce the processing time and optimise the algorithms was a priority. Using dedicated tools such as Valgrind, Rabah identified that a significant amount of processing time was spent in the first loop making combinations from hits from *x-layers*. He rewrote part of this code in a smarter way and this allowed to reduce the processing time in this step by a factor two. Later on, he gave a try to using a Neural Network in the suppression of the ghosts track combinations inside the algorithm. With this improvement the ghost rate was reduced by a factor two.

Florian Mercier - 2017/L3

Co-supervised with Sébastien Descotes-Genon.

During three years, I shared a course called "introduction to particle physics" for second year bachelor students. Amongst my students Florian was probably the most curious one, and he asked me for advice. He wanted to do an internship working on a "theory" project but he was worried to end up only reading papers and making photocopies. After discussing with S. Descotes-Genon, we agreed to share his supervisor and investigate what would be the impact of measuring properties of $\Lambda_b^0 \rightarrow \Lambda(1520)\ell^+\ell^-$ decays in global fits. Florian used `flavio` a python based package for global flavour fits [81]. A few assumptions had to be made given that no form factors were computed for this decay, he used approximations suggested in arXiv:1102.00897 based on quark models and Heavy Quark Effective theory and produced constraints on the Wilson coefficients C_9 and C_{10} .

Mathieu Markovitch & Corentin van Den Broek D'obrenan - 2019/L3

Co-supervised with Carla Marin Benito.

The work of Mathieu and Corentin was based on arXiv:1807.01643. Mathieu studied the impact of the radiative decay $B_s \rightarrow f_1(1420)\gamma$ on the Wilson coefficient C_7' associated with right-handed currents in $b \rightarrow s$

transitions using the `flaviO` package. The final state $B_s \rightarrow f_1(1420)(\rightarrow KK\pi^0)\gamma$ is quite challenging to reconstruct at LHCb. Corentin used multivariate approaches from the `scikit learn` software to evaluate the possibility of seeing this signal in the LHCb data.

Felicia Volle - 2019/M2

Co-supervised with Carla Marin Benito.

The $m(pK)$ spectrum from $\Lambda_b^0 \rightarrow pK\ell^+\ell^-$ decays has never been measured outside of the J/ψ region, ultimately it will be needed to know the resonant structure of the hadronic part of the rare modes to be able to compare any result to theoretical predictions and this will be possible when enough data will be analysed. One can use the region around $q^2 = 0$, where the photon is produced on shell to perform such a study. As part of her internship, Felicia worked on a selection using a multi-variable method to isolate $\Lambda_b^0 \rightarrow pK\gamma$ decays. She showed that one can expect to have about 1'000 signal candidates in 2012 data collected by LHCb.

Anja Beck - 2019/M2

Co-supervised with Carla Marin Benito.

Anja is enrolled at the University of Dortmund in Johannes Albrecht's group. She spent six months in our group at IJCLab as part of an Erasmus program. Anja's work is a follow up of Felicia's one. She first investigated the shape of the angular acceptance and resolution. Anja dived in the helicity formalism needed to perform the amplitude analysis of $\Lambda_b^0 \rightarrow pK\gamma$. This work is now documented in [arXiv:2002.02692](https://arxiv.org/abs/2002.02692) and submitted to JHEP. The amplitude fit that she is developing is based on the TensorFlow software. She already has a version of the fit which gives sensible results of the fractions for the different Λ^* resonances, using the legacy Run 1/2 LHCb datasets.



Measurement of the Λ_b^0 , Ξ_b^- and Ω_b^- baryon masses

The LHCb collaboration[†]

Abstract

Bottom baryons decaying to a J/ψ meson and a hyperon are reconstructed using 1.0 fb^{-1} of data collected in 2011 with the LHCb detector. Significant $\Lambda_b^0 \rightarrow J/\psi \Lambda$, $\Xi_b^- \rightarrow J/\psi \Xi^-$ and $\Omega_b^- \rightarrow J/\psi \Omega^-$ signals are observed and the corresponding masses are measured to be

$$\begin{aligned} M(\Lambda_b^0) &= 5619.53 \pm 0.13 \text{ (stat)} \pm 0.45 \text{ (syst)} \text{ MeV}/c^2, \\ M(\Xi_b^-) &= 5795.8 \pm 0.9 \text{ (stat)} \pm 0.4 \text{ (syst)} \text{ MeV}/c^2, \\ M(\Omega_b^-) &= 6046.0 \pm 2.2 \text{ (stat)} \pm 0.5 \text{ (syst)} \text{ MeV}/c^2, \end{aligned}$$

while the differences with respect to the Λ_b^0 mass are

$$\begin{aligned} M(\Xi_b^-) - M(\Lambda_b^0) &= 176.2 \pm 0.9 \text{ (stat)} \pm 0.1 \text{ (syst)} \text{ MeV}/c^2, \\ M(\Omega_b^-) - M(\Lambda_b^0) &= 426.4 \pm 2.2 \text{ (stat)} \pm 0.4 \text{ (syst)} \text{ MeV}/c^2. \end{aligned}$$

These are the most precise mass measurements of the Λ_b^0 , Ξ_b^- and Ω_b^- baryons to date. Averaging the above Λ_b^0 mass measurement with that published by LHCb using 35 pb^{-1} of data collected in 2010 yields $M(\Lambda_b^0) = 5619.44 \pm 0.13 \text{ (stat)} \pm 0.38 \text{ (syst)} \text{ MeV}/c^2$.

Submitted to Physical Review Letters

© CERN on behalf of the LHCb collaboration, license CC-BY-3.0.

[†]Authors are listed on the following pages.

Hadrons are systems bound by the strong interaction, described at the fundamental level by quantum chromodynamics (QCD). While QCD is well understood at high energy in the perturbative regime, low-energy phenomena such as the binding of quarks and gluons within hadrons are more difficult to predict. Several models and techniques, such as constituent quark models or lattice QCD calculations, attempt to reproduce the spectrum of the measured hadron masses (for a review, see Ref. [1]). While the masses of all expected ground-state mesons are now well measured, baryon data are still sparse. In particular, only six out of the sixteen b -baryon ground states predicted by the quark model have been observed so far [2]. A complete and reliable experimental mass spectrum would allow for precision tests of a variety of QCD models [3].

The mass measurement of the heaviest observed b baryon, the Ω_b^- state with bss valence quark content, is of particular interest. While both the D0 and CDF collaborations have claimed the observation of the $\Omega_b^- \rightarrow J/\psi \Omega^-$ decay, the reported mass values, 6165 ± 10 (stat) ± 13 (syst) MeV/ c^2 from D0 [4] and 6054.4 ± 6.8 (stat) ± 0.9 (syst) MeV/ c^2 from CDF [5], differ by more than 6 standard deviations. On the other hand, there is good agreement between the mass measurements of the Ξ_b^- (bsd) baryon, which has also been observed by D0 [6] and CDF [7] in the $\Xi_b^- \rightarrow J/\psi \Xi^-$ mode and, more recently, by CDF [8] in the $\Xi_b^- \rightarrow \Xi_c^0 \pi^-$ mode. These measurements average to 5791.1 ± 2.2 MeV/ c^2 [2].

This letter presents mass measurements of the weakly decaying Λ_b^0 (bud), Ξ_b^- and Ω_b^- baryons using the decay modes $\Lambda_b^0 \rightarrow J/\psi \Lambda$, $\Xi_b^- \rightarrow J/\psi \Xi^-$ and $\Omega_b^- \rightarrow J/\psi \Omega^-$ (charge-conjugated modes are implied throughout). The mass differences with respect to the Λ_b^0 mass are also reported. This analysis uses data corresponding to an integrated luminosity of 1.0 fb^{-1} and collected in pp collisions at a centre-of-mass energy of $\sqrt{s} = 7 \text{ TeV}$ with the LHCb detector in 2011.

The LHCb detector [9] is a single-arm forward spectrometer covering the pseudorapidity range $2 < \eta < 5$, designed for the study of particles containing b or c quarks. The detector includes a high precision tracking system consisting of a silicon-strip vertex detector surrounding the pp interaction region, a large-area silicon-strip detector located upstream of a dipole magnet with a bending power of about 4 Tm, and three stations of silicon-strip detectors and straw drift tubes placed downstream. The combined tracking system has a momentum resolution $\Delta p/p$ that varies from 0.4% at 5 GeV/ c to 0.6% at 100 GeV/ c , and an impact parameter resolution of $20 \mu\text{m}$ for tracks with high transverse momentum. Charged hadrons are identified using two ring-imaging Cherenkov detectors. Photon, electron and hadron candidates are identified by a calorimeter system consisting of scintillating-pad and preshower detectors, an electromagnetic calorimeter and a hadronic calorimeter. Muons are identified by a system composed of alternating layers of iron and multiwire proportional chambers. The trigger [10] consists of a hardware stage, based on information from the calorimeter and muon systems, followed by a software stage which applies a full event reconstruction.

Precision mass measurements require the momenta of the final state particles to be determined accurately. Therefore, an important feature of this analysis is the calibration of the tracker response. This accounts for imperfect knowledge of the magnetic field and tracker alignment [11]. In order to reduce these dominant contributions to the systematic

uncertainty, a two-step momentum calibration procedure is applied. Firstly, inclusive $J/\psi \rightarrow \mu^+\mu^-$ decays are used to account for the changes in the relative momentum scale between different data taking periods. Secondly, the absolute scale is derived from $B^+ \rightarrow J/\psi K^+$ decays, taking the known masses [2] as references. In this procedure, the use of a J/ψ mass constraint allows the momentum scale to be determined as a function of the K^+ track kinematics. The resulting calibration is checked with a variety of fully reconstructed decays listed in Fig. 1. For each mode the mass distribution is modelled taking into account the effect of QED radiative corrections, resolution and background, and the mean mass value is determined. Following the procedure described in Ref. [11], the deviation of the measured mass from the expected value is converted into an estimate of an average momentum scale bias independent of time and track kinematics. The bias is referred to as α , which is defined such that the measured mass becomes equal to the expected value if all particle momenta are multiplied by $1 - \alpha$. By definition, one expects $\alpha = 0$ to a good precision for the $B^+ \rightarrow J/\psi K^+$ calibration mode. Figure 1 shows the resulting values of α . The nominal mass measurements are performed with $\alpha = 0$ and the largest value of $|\alpha|$ amongst the considered modes, 0.3×10^{-3} , is conservatively taken as the systematic uncertainty on the calibrated momentum scale. This uncertainty is somewhat larger than the 0.2×10^{-3} achieved with the 2010 data [11], due to changes in the alignment of the tracking devices.

In this analysis, the b -baryon decays $\Lambda_b^0 \rightarrow J/\psi \Lambda$, $\Xi_b^- \rightarrow J/\psi \Xi^-$ and $\Omega_b^- \rightarrow J/\psi \Omega^-$, followed by $J/\psi \rightarrow \mu^+\mu^-$, $\Lambda \rightarrow p\pi^-$, $\Xi^- \rightarrow \Lambda\pi^-$ and $\Omega^- \rightarrow \Lambda K^-$, are reconstructed. The topology of these decays is characterised by the long-lived particles in the decay chain. The lifetime of weakly-decaying b baryons is ~ 1.5 ps and their decay vertex is expected to be separated from the primary pp interaction vertex by ~ 6 mm on average. The J/ψ candidates are reconstructed from pairs of oppositely-charged tracks, originating from the secondary vertex, that have hits in the muon detector. In the Ξ_b^- (Ω_b^-) decay chain the long-lived Ξ^- (Ω^-) decays into a Λ and a charged pion (kaon) at a tertiary vertex and the Λ decays at a quaternary vertex. Since $\sim 90\%$ of the decays are not fully contained in the vertex detector, tracks that have no hits in the vertex detector are also considered in the reconstruction of the tertiary and quaternary vertices.

The selections of Ξ_b^- and Ω_b^- candidates are identical apart from the choice of the Ξ^- , Ξ_b^- , Ω^- , Ω_b^- invariant mass ranges and particle identification requirements on the pion (kaon) from the Ξ^- (Ω^-) vertex. The Λ_b^0 selection is slightly different, owing to the different topology.

The J/ψ candidates are required to satisfy $|M_{\mu\mu} - M_{J/\psi}| < 4.2\sigma$ where $M_{\mu\mu}$ is the reconstructed di-muon mass, $M_{J/\psi}$ the J/ψ mass [2] and σ the estimated event-by-event uncertainty on $M_{\mu\mu}$ (typically $10 \text{ MeV}/c^2$). The invariant mass windows for the Λ , Ξ^- and Ω^- candidates are $\pm 6 \text{ MeV}/c^2$, $\pm 11 \text{ MeV}/c^2$ and $\pm 11 \text{ MeV}/c^2$ around the expected masses [2], respectively. Particle identification requirements are applied to the kaon from the Ω^- candidate and the proton from the Λ decay to improve the purity of the selected daughter particles, but none is placed on the pion from the Ξ^- candidate. In addition, the hyperon decay vertices are required to be downstream of the b -hadron decay vertex.

The Λ_b^0 , Ξ_b^- and Ω_b^- mass resolutions are improved by performing a fit of the decay

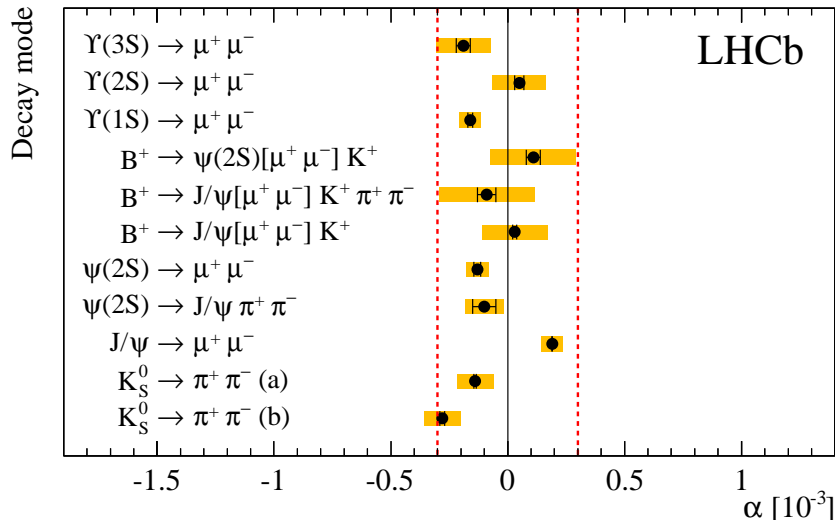


Figure 1: Average momentum scale bias α determined from the reconstructed mass of various decay modes after the momentum calibration procedure. The K_S^0 decays are divided into two categories according to whether both daughter tracks (a) have hits or (b) do not have hits in the vertex detector. The black error bars represent the statistical uncertainty whilst the (yellow) filled areas also include contributions to the systematic uncertainty from the fitting procedure, the effect of QED radiative corrections, and the uncertainty on the mass of the decaying meson [2]. The (red) dashed lines show the assigned uncertainty of $\pm 0.3 \times 10^{-3}$ on the momentum scale.

topology and vertices [12] while constraining the masses of the J/ψ , Λ , Ξ^- and Ω^- hadrons to have their known values [2], the final-state and intermediate long-lived particles to originate from common vertices according to the decay chain, and the b baryon to originate from the primary vertex. Three additional variables are considered for the selection. These are the χ^2 per degree of freedom (χ^2/ndf) from the fit, the reconstructed decay time and the χ_{IP}^2 of the b baryon from the primary vertex. The χ_{IP}^2 is defined as the difference in the χ^2 of the primary vertex fit with and without the b -baryon candidate. In the case of the Ξ_b^- candidates, the selection requirements for these variables are chosen to maximise the expected significance of the Ξ_b^- signal; the same selection is used for the Ω_b^- candidates. To determine the significance for a set of selection criteria the background yield is estimated from the yield of Ξ_b^- candidates found in mass side-bands in the ranges 5600–5700 MeV/ c^2 and 5900–6100 MeV/ c^2 . The expected signal yield is estimated using the product of the world average hadronisation fraction for $b \rightarrow \Xi_b^-$ and branching fractions for $\Xi_b^- \rightarrow J/\psi \Xi^-$ and subsequent daughter particle decays [2], the $b\bar{b}$ production cross-section in the LHCb acceptance [13] and the selection efficiencies obtained from simulation. The selection criteria giving the highest expected signal significance correspond to a decay time greater than 0.25 ps, a χ^2/ndf smaller than 4 and a χ_{IP}^2 smaller than 16. Amongst these, the decay time requirement is the most powerful given the high level of background close to the interaction point. In the case of the Λ_b^0 candidates, the decay time is required to be

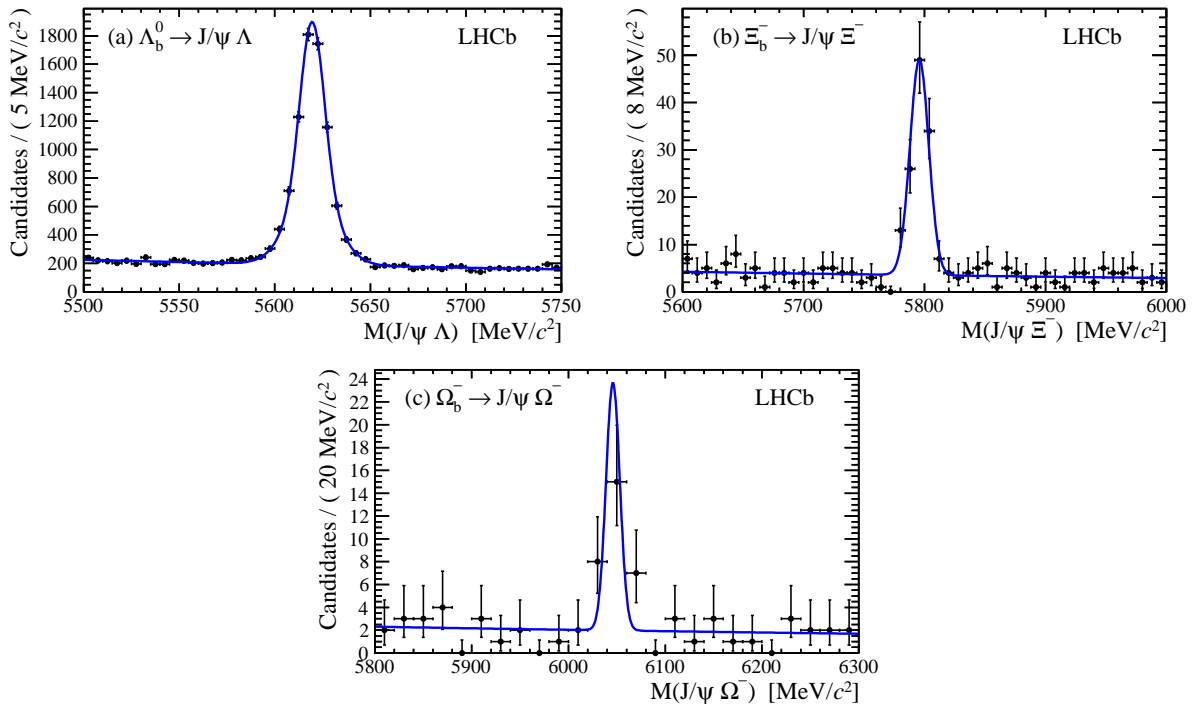


Figure 2: Invariant mass distribution for (a) $\Lambda_b^0 \rightarrow J/\psi \Lambda$, (b) $\Xi_b^- \rightarrow J/\psi \Xi_b^-$ and (c) $\Omega_b^- \rightarrow J/\psi \Omega_b^-$ candidates. The results of the unbinned maximum likelihood fits are shown with solid lines.

greater than 0.3 ps and the χ^2/ndf smaller than 5 (no requirement on the χ_{IP}^2 is made). The possibility of a cross-feed background between Ξ_b^- and Ω_b^- is investigated using simulation and found to be negligible in comparison with the combinatorial background.

The invariant mass distributions of the selected Λ_b^0 , Ξ_b^- and Ω_b^- candidates are shown in Fig. 2. In each case, the mass is measured by performing an unbinned extended maximum likelihood fit. The Λ_b^0 , Ξ_b^- , Ω_b^- candidates are retained for the mass fit if their invariant mass lies in the range 5500–5750, 5600–6000, 5800–6300 MeV/c^2 , respectively. The signal component is described with a single Gaussian function (or the sum of two Gaussian functions with common mean in the case of the Λ_b^0 baryon) and the background is modelled with an exponential function. The widths of the Λ_b^0 and Ξ_b^- signals are left unconstrained in the fit. Due to the low expected yield for the Ω_b^- signal, the width of the Gaussian function describing the Ω_b^- signal is fixed to the measured Ξ_b^- signal width multiplied by the ratio of Ω_b^- and Ξ_b^- widths from the simulation (8.2 MeV/c^2 for Ω_b^- and 8.9 MeV/c^2 for Ξ_b^-). The fit results are given in Table 1.

The statistical significance of the Ω_b^- signal is determined using simulated pseudo-experiments with background only. We determine the probability that, anywhere in the mass range between 5800 and 6300 MeV/c^2 , a peak appears with the expected width and a yield at least as large as that observed in the data. This probability corresponds to 6 standard deviations, which we interpret as the statistical significance of the Ω_b^- signal.

Table 1: Results of the fits to the invariant mass distributions. The quoted uncertainties are statistical. The Λ_b^0 signal is described by a double Gaussian function with widths σ_1 and σ_2 ; the fraction of the yield described by the first component is 0.58 ± 0.11 .

	Signal yield	Mass [MeV/ c^2]	Width(s) [MeV/ c^2]
Λ_b^0	6870 ± 110	5619.53 ± 0.13	$\sigma_1 = 6.4 \pm 0.5$ $\sigma_2 = 12.5 \pm 1.3$
Ξ_b^-	111 ± 12	5795.8 ± 0.9	7.8 ± 0.7
Ω_b^-	19 ± 5	6046.0 ± 2.2	7.2 (fixed)

The systematic uncertainties are evaluated by repeating the complete analysis (including the track fit and the momentum scale calibration when needed), varying in turn within its uncertainty each parameter to which the mass determination is sensitive. The observed changes in the central values of the fitted masses relative to the nominal results are then assigned as systematic uncertainties and summed in quadrature. The systematic uncertainties are summarised in Table 2.

The dominant systematic uncertainty is due to the momentum scale calibration described previously, which is assigned an uncertainty of $\pm 0.3 \times 10^{-3}$. A significant contribution to this uncertainty comes from the overall detector length scale along the beam axis, which is known to a relative precision of 10^{-3} [14]. This translates into a $\pm 0.13 \times 10^{-3}$ uncertainty on the momentum scale, and is included in the overall $\pm 0.3 \times 10^{-3}$ uncertainty. Most of the uncertainty related to the momentum scale is removed in the measurements of the mass differences.

The uncertainty on the amount of material assumed in the track reconstruction for the energy loss (dE/dx) correction has been found to be small [11]. It translates into an uncertainty on the Λ_b^0 mass of $0.09 \text{ MeV}/c^2$, which we apply to all masses.

The invariant mass of Ω_b^- candidates is computed assuming the central value of the Ω^- world-average mass [2]. The uncertainty of $\pm 0.29 \text{ MeV}/c^2$ on this value is propagated as a systematic uncertainty. A similar, but smaller, uncertainty is estimated for the Ξ_b^- and Λ_b^0 masses from the imperfect knowledge of the Ξ^- and Λ masses, respectively.

Two alternative fits for the Λ_b^0 signal are performed: a first fit where the candidates are split into two categories depending on whether the daughter tracks have vertex detector information or not, each category being described with a single Gaussian function where the two Gaussian functions have a common mean, and a second fit using the sum of two Crystal Ball functions [15] with common peak value and otherwise unconstrained parameters. The second fit allows to take into account possible QED radiative corrections.

The Ξ_b^- mass fit is repeated using as an alternative model either the sum of two Gaussian functions with a common mean, or a single Crystal Ball function. In the Ω_b^- mass fit, the fixed Gaussian width is varied within both the uncertainty of the fitted Ξ_b^- width and the statistical uncertainty of the width ratio from simulation.

An alternative background model assuming a linear shape leads to negligible changes.

Table 2: Systematic uncertainties (in MeV/c^2) on the mass measurements and their differences. The total systematic uncertainty is obtained from adding all uncertainties in quadrature.

Source	Λ_b^0	Ξ_b^-	Ω_b^-	$\Xi_b^- - \Lambda_b^0$	$\Omega_b^- - \Lambda_b^0$
Momentum scale	0.43	0.43	0.31	0.01	0.12
dE/dx correction	0.09	0.09	0.09	0.01	0.01
Hyperon mass	0.01	0.07	0.25	0.07	0.25
Signal model	0.07	0.01	0.24	0.07	0.25
Background model	0.01	0.01	0.02	0.01	0.02
Total	0.45	0.45	0.47	0.10	0.37

We also repeat the Ξ_b^- and Ω_b^- mass fits in a restricted mass range of 5650–5950 MeV/c^2 and 5900–6200 MeV/c^2 , respectively, and assign the resulting change as a systematic uncertainty.

In summary, the Λ_b^0 , Ξ_b^- and Ω_b^- baryons are observed in the $\Lambda_b^0 \rightarrow J/\psi \Lambda$, $\Xi_b^- \rightarrow J/\psi \Xi^-$ and $\Omega_b^- \rightarrow J/\psi \Omega^-$ decay modes using 1.0 fb^{-1} of pp collisions collected in 2011 at a centre-of-mass energy of $\sqrt{s} = 7 \text{ TeV}$. The statistical significance of the observed $\Omega_b^- \rightarrow J/\psi \Omega^-$ signal is 6 standard deviations. The masses of the b baryons are measured to be

$$\begin{aligned}
 M(\Lambda_b^0) &= 5619.53 \pm 0.13 \pm 0.45 \text{ MeV}/c^2, \\
 M(\Xi_b^-) &= 5795.8 \pm 0.9 \pm 0.4 \text{ MeV}/c^2, \\
 M(\Omega_b^-) &= 6046.0 \pm 2.2 \pm 0.5 \text{ MeV}/c^2,
 \end{aligned}$$

where the first (second) quoted uncertainty is statistical (systematic). The dominant systematic uncertainty, due to the knowledge of the momentum scale, partially cancels in mass differences. We obtain

$$\begin{aligned}
 M(\Xi_b^-) - M(\Lambda_b^0) &= 176.2 \pm 0.9 \pm 0.1 \text{ MeV}/c^2, \\
 M(\Omega_b^-) - M(\Lambda_b^0) &= 426.4 \pm 2.2 \pm 0.4 \text{ MeV}/c^2.
 \end{aligned}$$

A measurement of the Λ_b^0 mass based on the 2010 data sample, $M(\Lambda_b^0) = 5619.19 \pm 0.70 \pm 0.30 \text{ MeV}/c^2$, has been previously reported by LHCb [11]. Since the new alignment and momentum calibration procedures differ from those applied in the previous study, a possible correlation between the systematic uncertainties related to the momentum scale can be neglected. Considering that the only correlated systematic uncertainties are those due to energy loss correction and mass fitting, the weighted average of the two Λ_b^0 mass measurements that minimizes the total uncertainty is

$$M(\Lambda_b^0) = 5619.44 \pm 0.13 \pm 0.38 \text{ MeV}/c^2.$$

These Λ_b^0 , Ξ_b^- and Ω_b^- mass measurements are the most precise to date. They are compared in Table 3 with the single most precise measurements from ATLAS, CDF and

Table 3: Comparison of the b -baryon mass measurements using the full 2011 data sample with the single most precise results from the ATLAS [16], CDF [5, 17] and D0 [4, 6] collaborations, and with the PDG averages [2]. The PDG averages contain the results from CDF and D0 as well as the Λ_b^0 measurement from LHCb performed with the 2010 data sample. The quoted errors include statistical and systematic uncertainties. All values are in MeV/c^2 .

	$M(\Lambda_b^0)$	$M(\Xi_b^-)$	$M(\Omega_b^-)$
ATLAS	5619.7 ± 1.3	–	–
CDF	5619.7 ± 1.7	5790.9 ± 2.7	6054.4 ± 6.9
D0	–	5774 ± 19	6165 ± 16
PDG	5619.4 ± 0.7	5791.1 ± 2.2	6071 ± 40
LHCb	5619.5 ± 0.5	5795.8 ± 1.0	6046.0 ± 2.3

D0, and with the current world averages [2]. The Λ_b^0 and Ξ_b^- results are in agreement with previous measurements. The Ω_b^- result is in agreement with the CDF measurement [5], but in disagreement with the D0 measurement [4].

Acknowledgements

We express our gratitude to our colleagues in the CERN accelerator departments for the excellent performance of the LHC. We thank the technical and administrative staff at the LHCb institutes. We acknowledge support from CERN and from the national agencies: CAPES, CNPq, FAPERJ and FINEP (Brazil); NSFC (China); CNRS/IN2P3 and Region Auvergne (France); BMBF, DFG, HGF and MPG (Germany); SFI (Ireland); INFN (Italy); FOM and NWO (The Netherlands); SCSR (Poland); ANCS/IFA (Romania); MinES, Rosatom, RFBR and NRC “Kurchatov Institute” (Russia); MinECo, XuntaGal and GENCAT (Spain); SNSF and SER (Switzerland); NAS Ukraine (Ukraine); STFC (United Kingdom); NSF (USA). We also acknowledge the support received from the ERC under FP7. The Tier1 computing centres are supported by IN2P3 (France), KIT and BMBF (Germany), INFN (Italy), NWO and SURF (The Netherlands), PIC (Spain), GridPP (United Kingdom). We are thankful for the computing resources put at our disposal by Yandex LLC (Russia), as well as to the communities behind the multiple open source software packages that we depend on.

References

- [1] C. Amsler, T. Degrand, and B. Krusche, *Quark model*, published in Ref. [2].
- [2] Particle Data Group, J. Beringer *et al.*, *Review of particle physics*, Phys. Rev. **D86** (2012) 010001.

- [3] M. Karliner, B. Keren-Zur, H. Lipkin, and J. Rosner, *The quark model and b baryons*, *Annals Phys.* **342** (2009) 2, arXiv: 0804.1575; J. P. Day, W. Plessas, and K.-S. Choi, *Universal constituent-quark model for baryons*, arXiv: 1205.6918; X. Liu *et al.*, *Bottom baryons*, *Phys. Rev.* **D77** (2008) 014031, arXiv: 0710.0123; E. E. Jenkins, *Model-independent bottom baryon mass predictions in the $1/N_c$ expansion*, *Phys. Rev.* **D77** (2008) 034012, arXiv: 0712.0406; R. Roncaglia, D. Lichtenberg, and E. Predazzi, *Predicting the masses of baryons containing one or two heavy quarks*, *Phys. Rev.* **D52** (1995) 1722, arXiv: hep-ph/9502251; N. Mathur, R. Lewis, and R. Woloshyn, *Charmed and bottom baryons from lattice NROCD*, *Phys. Rev.* **D66** (2002) 014502, arXiv: hep-ph/0203253; D. Ebert, R. Faustov, and V. Galkin, *Masses of heavy baryons in the relativistic quark model*, *Phys. Rev.* **D72** (2005) 034026, arXiv: hep-ph/0504112.
- [4] D0 collaboration, V. Abazov *et al.*, *Observation of the doubly strange b baryon Ω_b^-* , *Phys. Rev. Lett.* **101** (2008) 232002, arXiv: 0808.4142.
- [5] CDF collaboration, T. Aaltonen *et al.*, *Observation of the Ω_b^- baryon and measurement of the properties of the Ξ_b^- and Ω_b^- baryons*, *Phys. Rev.* **D80** (2009) 072003, arXiv: 0905.3123.
- [6] D0 collaboration, V. Abazov *et al.*, *Direct observation of the strange b baryon Ξ_b^-* , *Phys. Rev. Lett.* **99** (2007) 052001, arXiv: 0706.1690.
- [7] CDF collaboration, T. Aaltonen *et al.*, *Observation and mass measurement of the baryon Ξ_b^-* , *Phys. Rev. Lett.* **99** (2007) 052002, arXiv: 0707.0589.
- [8] CDF collaboration, T. Aaltonen *et al.*, *Observation of the Ξ_b^0 baryon*, *Phys. Rev. Lett.* **107** (2011) 102001, arXiv: 1107.4015.
- [9] LHCb collaboration, A. A. Alves Jr. *et al.*, *The LHCb detector at the LHC*, *JINST* **3** (2008) S08005.
- [10] R. Aaij *et al.*, *The LHCb trigger and its performance*, arXiv: 1211.3055.
- [11] LHCb collaboration, R. Aaij *et al.*, *Measurement of b -hadron masses*, *Phys. Lett.* **B708** (2012) 241, arXiv: 1112.4896.
- [12] W. D. Hulsbergen, *Decay chain fitting with a Kalman filter*, *Nucl. Instrum. Meth.* **A552** (2005) 566, arXiv: phys/cs/0503191.
- [13] LHCb collaboration, R. Aaij *et al.*, *Measurement of $\sigma(pp \rightarrow b\bar{b}X)$ at $\sqrt{s} = 7$ TeV in the forward region*, *Phys. Lett.* **B694** (2010) 209, arXiv: 1009.2731.
- [14] LHCb collaboration, R. Aaij *et al.*, *Measurement of the $B_s^0 - \bar{B}_s^0$ oscillation frequency Δm_s in $B_s^0 \rightarrow D_s^-(3)\pi$ decays*, *Phys. Lett.* **B709** (2012) 177, arXiv: 1112.4311.

- [15] T. Skwarnicki, *A study of the radiative cascade transitions between the Upsilon-prime and Upsilon resonances*, PhD thesis, Institute of Nuclear Physics, Krakow, 1986, DESY-F31-86-02.
- [16] ATLAS collaboration, G. Aad *et al.*, *Measurement of the Λ_b^0 lifetime and mass in the ATLAS experiment*, arXiv: 1207.2284.
- [17] CDF collaboration, D. Acosta *et al.*, *Measurement of b hadron masses in exclusive J/ψ decays with the CDF detector*, Phys. Rev. Lett. **96** (2006) 202001, arXiv: hep-ex/0508022.



Measurements of the B^+ , B^0 , B_s^0 meson and Λ_b^0 baryon lifetimes

The LHCb collaboration[†]

Abstract

Measurements of b -hadron lifetimes are reported using pp collision data, corresponding to an integrated luminosity of 1.0 fb^{-1} , collected by the LHCb detector at a centre-of-mass energy of 7 TeV. Using the exclusive decays $B^+ \rightarrow J/\psi K^+$, $B^0 \rightarrow J/\psi K^{*(892)0}$, $B^0 \rightarrow J/\psi K_S^0$, $\Lambda_b^0 \rightarrow J/\psi \Lambda$ and $B_s^0 \rightarrow J/\psi \phi$ the average decay times in these modes are measured to be

$$\begin{aligned} \tau_{B^+ \rightarrow J/\psi K^+} &= 1.637 \pm 0.004 \pm 0.003 \text{ ps}, \\ \tau_{B^0 \rightarrow J/\psi K^{*0}} &= 1.524 \pm 0.006 \pm 0.004 \text{ ps}, \\ \tau_{B^0 \rightarrow J/\psi K_S^0} &= 1.499 \pm 0.013 \pm 0.005 \text{ ps}, \\ \tau_{\Lambda_b^0 \rightarrow J/\psi \Lambda} &= 1.415 \pm 0.027 \pm 0.006 \text{ ps}, \\ \tau_{B_s^0 \rightarrow J/\psi \phi} &= 1.480 \pm 0.011 \pm 0.005 \text{ ps}, \end{aligned}$$

where the first uncertainty is statistical and the second is systematic. These represent the most precise lifetime measurements in these decay modes. In addition, ratios of these lifetimes, and the ratio of the decay-width difference, $\Delta\Gamma_d$, to the average width, Γ_d , in the B^0 system, $\Delta\Gamma_d/\Gamma_d = -0.044 \pm 0.025 \pm 0.011$, are reported. All quantities are found to be consistent with Standard Model expectations.

Submitted to JHEP

© CERN on behalf of the LHCb collaboration, license CC-BY-3.0.

[†]Authors are listed on the following pages.

1 Introduction

Within the framework of heavy quark expansion (HQE) theory [1–7], b -hadron observables are calculated as a perturbative expansion in inverse powers of the b -quark mass, m_b . At zeroth order the lifetimes of all weakly decaying b hadrons are equal, with corrections appearing at order $1/m_b^2$. Ratios of b -hadron lifetimes can be theoretically predicted with higher accuracy than absolute lifetimes since many terms in the HQE cancel. The latest theoretical predictions and world-average values for the b -hadron lifetimes and lifetime ratios are reported in Table 1. A measurement of the ratio of the Λ_b^0 baryon lifetime, using the $\Lambda_b^0 \rightarrow J/\psi p K^-$ decay mode¹, to that of the B^0 meson lifetime has recently been made by the LHCb collaboration [8] and is not yet included in the world average.

In this paper, a measurement of the lifetimes of the B^+ , B^0 and B_s^0 mesons and Λ_b^0 baryon is reported using pp collision data, corresponding to an integrated luminosity of 1.0 fb^{-1} , collected in 2011 with the LHCb detector at a centre-of-mass energy of 7 TeV. The lifetimes are measured from the reconstructed b -hadron decay time distributions of the exclusive decay modes $B^+ \rightarrow J/\psi K^+$, $B^0 \rightarrow J/\psi K^{*(892)0}$, $B^0 \rightarrow J/\psi K_s^0$, $B_s^0 \rightarrow J/\psi \phi$ and $\Lambda_b^0 \rightarrow J/\psi \Lambda$. Collectively, these are referred to as $H_b \rightarrow J/\psi X$ decays. In addition, measurements of lifetime ratios are reported.

As a result of neutral meson mixing the decay time distribution of neutral B_q^0 mesons ($q \in \{s, d\}$) is characterised by two parameters, namely the average decay width Γ_q and the decay width difference $\Delta\Gamma_q$ between the light (L) and heavy (H) B_q^0 mass eigenstates. The summed decay rate of B_q^0 and \bar{B}_q^0 mesons to a final state f is given by [9–11]

$$\langle \Gamma(B_q^0(t) \rightarrow f) \rangle \equiv \Gamma(B_q^0(t) \rightarrow f) + \Gamma(\bar{B}_q^0(t) \rightarrow f) = R_{q,L}^f e^{-\Gamma_{q,L} t} + R_{q,H}^f e^{-\Gamma_{q,H} t}, \quad (1)$$

where terms proportional to the small flavour specific asymmetry, a_{fs}^q , are ignored [12]. Therefore, for non-zero $\Delta\Gamma_q$ the decay time distribution of neutral B_q^0 decays is not purely exponential. In the case of an equal admixture of B_q^0 and \bar{B}_q^0 at $t = 0$, the observed average decay time is given by [11]

$$\tau_{B_q^0 \rightarrow f} = \frac{1}{\Gamma_q} \frac{1}{1 - y_q^2} \left(\frac{1 + 2\mathcal{A}_{\Delta\Gamma_q}^f y_q + y_q^2}{1 + \mathcal{A}_{\Delta\Gamma_q}^f y_q} \right), \quad (2)$$

where $y_q \equiv \Delta\Gamma_q/(2\Gamma_q)$ and $\mathcal{A}_{\Delta\Gamma_q}^f \equiv (R_{q,H}^f - R_{q,L}^f)/(R_{q,H}^f + R_{q,L}^f)$ is an observable that depends on the final state, f . As such, the lifetimes measured are usually referred to as *effective* lifetimes. In the B_s^0 system, where $\Delta\Gamma_s/\Gamma_s = 0.159 \pm 0.023$ [13], the deviation from an exponential decay time distribution is non-negligible. In contrast, in the B^0 system this effect is expected to be small as $\Delta\Gamma_d/\Gamma_d$ is predicted to be $(42 \pm 8) \times 10^{-4}$ in the Standard Model (SM) [14, 15]. Both the BaBar [16, 17] and Belle [18] collaborations have measured $|\Delta\Gamma_d/\Gamma_d|$ and the current world average is $|\Delta\Gamma_d/\Gamma_d| = 0.015 \pm 0.018$ [13]. A deviation in the value of $\Delta\Gamma_d$ from the SM prediction has recently been proposed [19] as

¹Charge conjugation is implied throughout this paper, unless otherwise stated.

Table 1: Theoretical predictions and current world-average values [13] for b -hadron lifetimes and lifetime ratios.

Observable	Prediction	World average
τ_{B^+} [ps]	–	1.641 ± 0.008
τ_{B^0} [ps]	–	1.519 ± 0.007
$\tau_{B_s^0}$ [ps]	–	1.516 ± 0.011
$\tau_{A_b^0}$ [ps]	–	1.429 ± 0.024
τ_{B^+}/τ_{B^0}	1.063 ± 0.027 [15, 22, 23]	1.079 ± 0.007
$\tau_{B_s^0}/\tau_{B^0}$	1.00 ± 0.01 [15, 23–25]	0.998 ± 0.009
$\tau_{A_b^0}/\tau_{B^0}$	0.86–0.95 [3, 23, 26–32]	0.941 ± 0.016

a potential explanation for the anomalous like-sign dimuon charge asymmetry measured by the D0 collaboration [20]. In this paper, $\Delta\Gamma_d/\Gamma_d$ is measured from the effective lifetimes of $B^0 \rightarrow J/\psi K^*(892)^0$ and $B^0 \rightarrow J/\psi K_s^0$ decays, as proposed in Ref. [21].

The main challenge in the measurements reported is understanding and controlling the detector acceptance, reconstruction and selection efficiencies that depend upon the b -hadron decay time. This paper is organised as follows. Section 2 describes the LHCb detector and software. The selection criteria for the b -hadron candidates are described in Sec. 3. Section 4 describes the reconstruction efficiencies and the techniques used to correct the decay time distributions. Section 5 describes how the efficiency corrections are incorporated into the maximum likelihood fit that is used to measure the signal yields and lifetimes. The systematic uncertainties on the measurements are described in Sec. 6. The final results and conclusions are presented in Sec. 7.

2 Detector and software

The LHCb detector [33] is a single-arm forward spectrometer covering the pseudorapidity range $2 < \eta < 5$, designed for the study of particles containing b or c quarks. The detector includes a high-precision tracking system consisting of a silicon-strip vertex detector (VELO) surrounding the pp interaction region, a large-area silicon-strip detector (TT) located upstream of a dipole magnet with a bending power of about 4 Tm, and three stations of silicon-strip detectors and straw drift tubes placed downstream. The combined tracking system provides a momentum, p , measurement with relative uncertainty that varies from 0.4% at 5 GeV/ c to 0.6% at 100 GeV/ c , and impact parameter resolution of 20 μm for charged particles with high transverse momentum, p_T . Charged hadrons are identified using two ring-imaging Cherenkov detectors [34]. Photon, electron and hadron candidates are identified by a calorimeter system consisting of scintillating-pad and preshower detectors, an electromagnetic calorimeter and a hadronic calorimeter. Muons are identified by a system composed of alternating layers of iron and multiwire proportional chambers [35]. The right-handed coordinate system adopted has the z -axis along the beam line and the y -axis along the vertical. The trigger [36] consists of a hardware stage,

based on information from the calorimeter and muon systems, followed by a software stage, which applies a full event reconstruction.

Two distinct classes of tracks are reconstructed using hits in the tracking stations on both sides of the magnet, either with hits in the VELO (long track) or without (downstream track). The vertex resolution of b -hadron candidates reconstructed using long tracks is better than that for candidates reconstructed using downstream tracks. However, the use of long tracks introduces a dependence of the reconstruction efficiency on the b -hadron decay time.

In the simulation, pp collisions are generated using PYTHIA 6.4 [37] with a specific LHCb configuration [38]. Decays of hadronic particles are described by EVTGEN [39], in which final state radiation is generated using PHOTOS [40]. The interaction of the generated particles with the detector and its response are implemented using the GEANT4 toolkit [41] as described in Ref. [42].

3 Candidate selection

The reconstruction of each of the $H_b \rightarrow J/\psi X$ decays is similar and commences by selecting $J/\psi \rightarrow \mu^+\mu^-$ decays. Events passing the hardware trigger contain dimuon candidates with high transverse momentum. The subsequent software trigger is composed of two stages. The first stage performs a partial event reconstruction and requires events to have two well-identified oppositely charged muons with an invariant mass larger than $2.7 \text{ GeV}/c^2$. The selection at this stage has a uniform efficiency as a function of decay time. The second stage performs a full event reconstruction, calculating the position of each pp interaction vertex (PV) using all available charged particles in the event. The average number of PVs in each event is approximately 2.0. Their longitudinal (z) position is known to a precision of approximately 0.05 mm. If multiple PVs are reconstructed in the event, the one with the minimum value of χ_{IP}^2 is associated with the J/ψ candidate, where χ_{IP}^2 is the increase in the χ^2 of the PV fit if the candidate trajectory is included. Events are retained for further processing if they contain a $J/\psi \rightarrow \mu^+\mu^-$ pair that forms a vertex that is significantly displaced from the PV. This introduces a non-uniform efficiency as function of decay time.

The offline sample of J/ψ meson candidates is selected by requiring each muon to have p_{T} larger than $500 \text{ MeV}/c$ and the J/ψ candidate to be displaced from the PV by more than three times its decay length uncertainty. The invariant mass of the two muons, $m(\mu^+\mu^-)$, must be in the range $[3030, 3150] \text{ MeV}/c^2$.

The b -hadron candidate selection is performed by applying kinematic and particle identification criteria to the final-state tracks, the details of which are reported in Sec. 3.1 to 3.5. No requirements are placed on variables that are highly correlated to the b -hadron decay time, thereby avoiding the introduction of additional biases. All final-state particles are required to have a pseudorapidity in the range $2.0 < \eta < 4.5$. In addition, the z -position of the PV (z_{PV}) is required to be within 100 mm of the nominal interaction point, where the standard deviation of the z_{PV} distribution is approximately 47 mm. These criteria cause a reduction of approximately 10% in signal yield but define a fiducial region where

the reconstruction efficiency is largely uniform.

The maximum likelihood fit uses the invariant mass, $m(J/\psi X)$, and proper decay time, t , of each b -hadron candidate. The decay time of the b -hadron candidate in its rest frame is derived from the relation $t = m l/q$, where m is its invariant mass and the decay length, l , and the momentum, q , are measured in the experimental frame. In this paper, t is computed using a kinematic decay-tree fit (DTF) [43] involving all final-state tracks from the b -hadron candidate with a constraint on the position of the associated PV. Unlike in the trigger, the position of each PV is calculated using all available charged particles in the event after the removal of the b -hadron candidate final-state tracks. This is necessary to prevent the final-state tracks from biasing the PV position towards the b -hadron decay vertex and helps to reduce the tails of the decay-time resolution function. This prescription does not bias the measured lifetime using simulated events. The χ^2 of the fit, χ_{DTF}^2 , is useful to discriminate between signal and background. In cases where there are multiple b -hadron candidates per event, the candidate with the smallest χ_{DTF}^2 is chosen. The z -position of the displaced b -hadron vertices are known to a precision of approximately 0.15 mm.

Studies of simulated events show that in the case of $B^0 \rightarrow J/\psi K^{*0}$ ($B_s^0 \rightarrow J/\psi \phi$) decays, imposing requirements on χ_{DTF}^2 introduces a dependence of the selection efficiency on the decay time if the K^+ and π^- (K^+ and K^-) tracks are included in the DTF. If no correction is applied to the decay time distribution, the measured lifetime would be biased by approximately -2 fs relative to the generated value. Using simulated events it is found that this effect is correlated to the opening angle between the K^+ and π^- (K^+ and K^-) from the K^{*0} (ϕ) decay. No effect is observed for the muons coming from the J/ψ decay due to the larger opening angle in this case. To remove the effect, the calculation of χ_{DTF}^2 for the $B^0 \rightarrow J/\psi K^{*0}$ and $B_s^0 \rightarrow J/\psi \phi$ channels is performed with an alternative DTF in which the assigned track parameter uncertainties of the kaon and pion are increased in such a way that their contribution to the b -hadron vertex position is negligible.

Candidates are required to have t in the range [0.3, 14.0] ps. The lower bound on the decay time suppresses a large fraction of the prompt combinatorial background that is composed of tracks from the same PV, while the upper bound is introduced to reduce the sensitivity to long-lived background candidates. In the case of the $B^0 \rightarrow J/\psi K_s^0$ and $\Lambda_b^0 \rightarrow J/\psi \Lambda$ decays, the lower bound is increased to 0.45 ps to compensate for the worse decay time resolution in these modes.

In events with multiple PVs, b -hadron candidates are removed if they have a χ_{IP}^2 with respect to the next best PV smaller than 50. This requirement is found to distort the decay time distribution, but reduces a source of background due to the incorrect association of the b hadron to its production PV.

The invariant mass is computed using another kinematic fit without any constraint on the PV position but with the invariant mass of the $\mu^+\mu^-$ pair, $m(\mu^+\mu^-)$, constrained to the known J/ψ mass [44]. Figures 1 and 2 show the $m(J/\psi X)$ distributions for the selected candidates in each final state and Table 2 gives the corresponding signal yields.

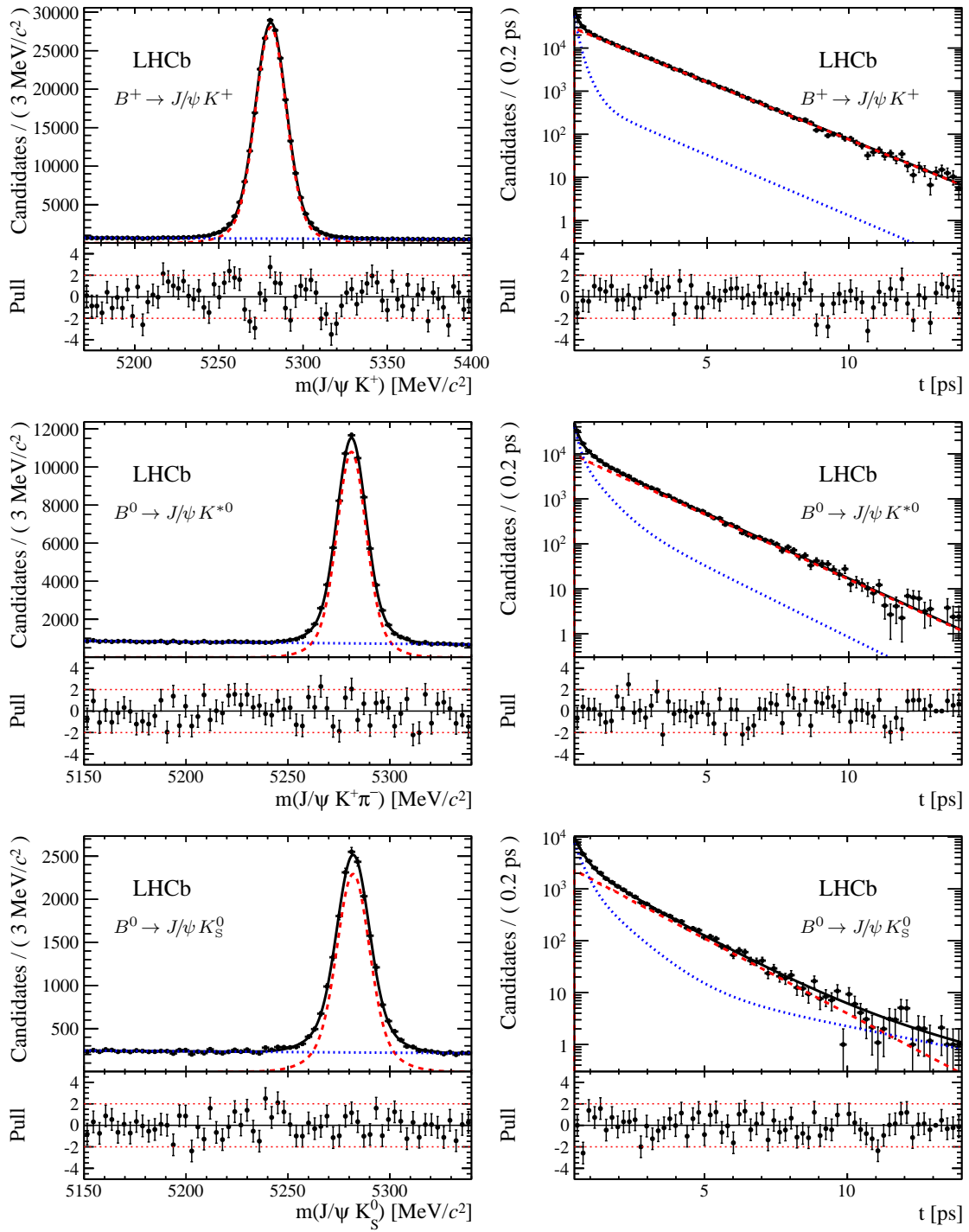


Figure 1: Distributions of the (left) mass and (right) decay time of $B^+ \rightarrow J/\psi K^+$, $B^0 \rightarrow J/\psi K^{*0}$ and $B^0 \rightarrow J/\psi K_s^0$ candidates and their associated residual uncertainties (pulls). The data are shown by the black points; the total fit function by the black solid line; the signal contribution by the red dashed line and the background contribution by the blue dotted line.

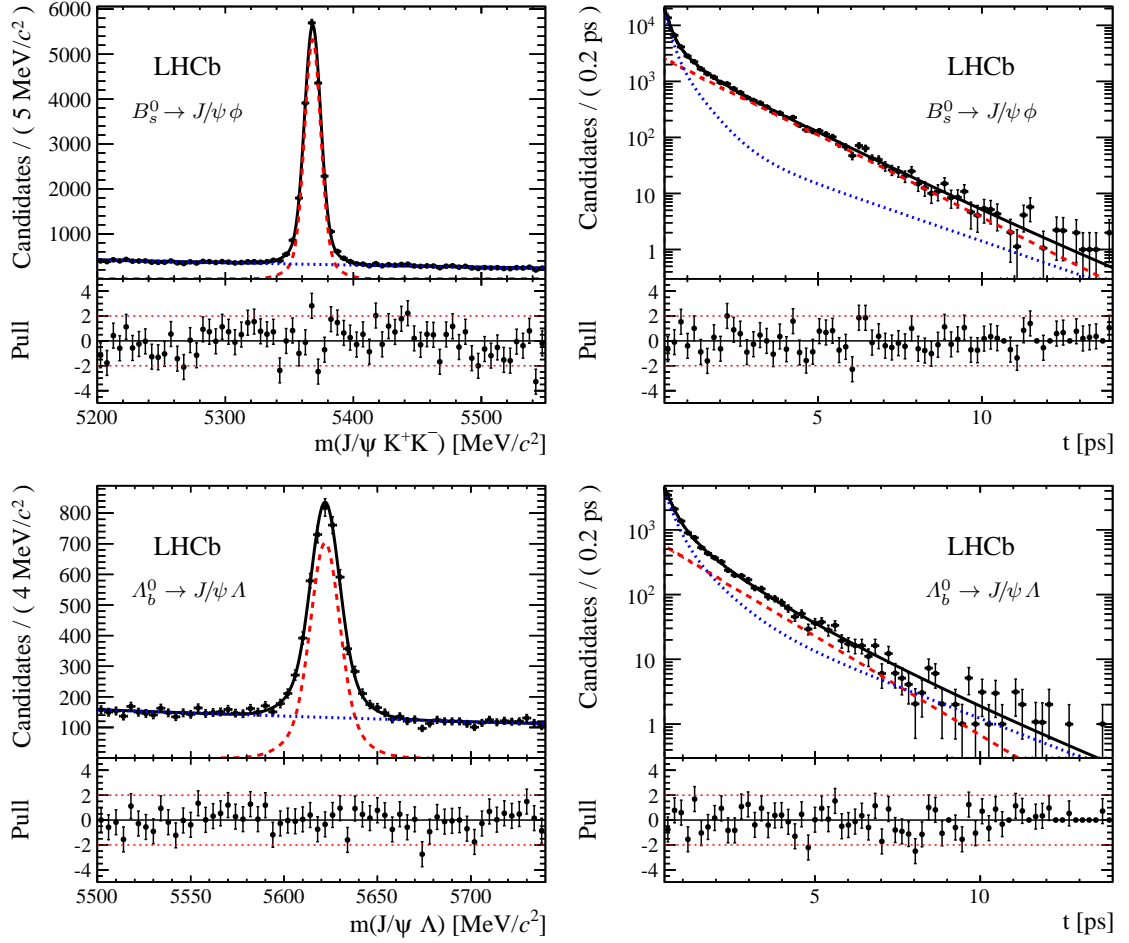


Figure 2: Distributions of the (left) mass and (right) decay time of $B_s^0 \rightarrow J/\psi \phi$ and $\Lambda_b^0 \rightarrow J/\psi \Lambda$ candidates and their associated residual uncertainties (pulls). The data are shown by the black points; the total fit function by the black solid line; the signal contribution by the red dashed line and the background contribution by the blue dotted line.

Table 2: Estimated event yields for the five $b \rightarrow J/\psi X$ channels selected using the criteria described in Sec. 3.1 to 3.5.

Channel	Yield
$B^+ \rightarrow J/\psi K^+$	$229\,434 \pm 503$
$B^0 \rightarrow J/\psi K^{*0}$	$70\,534 \pm 312$
$B^0 \rightarrow J/\psi K_s^0$	$17\,045 \pm 175$
$B_s^0 \rightarrow J/\psi \phi$	$18\,662 \pm 152$
$\Lambda_b^0 \rightarrow J/\psi \Lambda$	$3\,960 \pm 89$

3.1 Selection of $B^+ \rightarrow J/\psi K^+$ decays

The B^+ candidates are reconstructed by combining the J/ψ candidates with a charged particle that is identified as a kaon with p_T larger than 1 GeV/ c and p larger than 10 GeV/ c . The invariant mass, $m(J/\psi K^+)$, must be in the range [5170, 5400] MeV/ c^2 , where the lower bound is chosen to remove feed-down from incompletely reconstructed $B^0 \rightarrow J/\psi K^{*0}$ decays. The χ_{DTF}^2 of the fit, which has 5 degrees of freedom, is required to be less than 25. Multiple B^+ candidates are found in less than 0.02% of selected events.

3.2 Selection of $B^0 \rightarrow J/\psi K^{*0}$ decays

The K^{*0} candidates are reconstructed by combining two oppositely charged particles that are identified as a kaon and a pion. The pion and K^{*0} must have p_T greater than 0.3 GeV/ c and 1.5 GeV/ c , respectively. The invariant mass, $m(K^+\pi^-)$, must be in the range [826, 966] MeV/ c^2 .

The B^0 candidates are reconstructed by combining the J/ψ and K^{*0} candidates. The invariant mass, $m(J/\psi K^+\pi^-)$, must be in the range [5150, 5340] MeV/ c^2 , where the upper bound is chosen to remove the contribution from $B_s^0 \rightarrow J/\psi \bar{K}^{*0}$ decays. The χ_{DTF}^2 of the fit, which has 3 degrees of freedom, is required to be less than 15. Multiple B^0 candidates are found in 2.2% of selected events.

3.3 Selection of $B^0 \rightarrow J/\psi K_s^0$ decays

The K_s^0 candidates are formed from the combination of two oppositely charged particles that are identified as pions and reconstructed as downstream tracks. This is necessary since studies of simulated signal decays demonstrate that an inefficiency depending on the b -hadron decay time is introduced by the reconstruction of the long-lived K_s^0 and Λ particles using long tracks. Even so, it is found that the acceptance of the TT still depends on the origin of the tracks. This effect is removed by further tightening of the requirement on the position of the PV to $z_{\text{PV}} > -50$ mm.

For particles produced close to the interaction region, this effect is suppressed by the requirements on the fiducial region for the PV, which is further tightened by requiring

that , to account for the additional acceptance introduced by the TT.

The downstream pions are required to have p_T greater than $0.1 \text{ GeV}/c$ and p greater than $2 \text{ GeV}/c$. The K_s^0 candidate must have p_T greater than $1 \text{ GeV}/c$ and be well separated from the B^0 decay vertex, to suppress potential background from $B^0 \rightarrow J/\psi K^{*0}$ decays where the kaon has been misidentified as a pion. The χ^2 of the K_s^0 vertex fit must be less than 25 and the invariant mass of the dipion system, $m(\pi^+\pi^-)$, must be within $15 \text{ MeV}/c^2$ of the known K_s^0 mass [44]. For subsequent stages of the selection, $m(\pi^+\pi^-)$ is constrained to the known K_s^0 mass.

The invariant mass, $m(J/\psi K_s^0)$, of the J/ψ and K_s^0 candidate combination must be in the range $[5150, 5340] \text{ MeV}/c^2$, where the upper bound is chosen to remove the contribution from $B_s^0 \rightarrow J/\psi K_s^0$ decays. The χ_{DTF}^2 of the fit, which has 6 degrees of freedom, is required to be less than 30. Multiple B^0 candidates are found in less than 0.4% of selected events.

3.4 Selection of $B_s^0 \rightarrow J/\psi \phi$ decays

The ϕ candidates are formed from two oppositely charged particles that have been identified as kaons and originate from a common vertex. The K^+K^- pair is required to have p_T larger than $1 \text{ GeV}/c$. The invariant mass of the K^+K^- pair, $m(K^+K^-)$, must be in the range $[990, 1050] \text{ MeV}/c^2$.

The B_s^0 candidates are reconstructed by combining the J/ψ candidate with the K^+K^- pair, requiring the invariant mass, $m(J/\psi K^+K^-)$, to be in the range $[5200, 5550] \text{ MeV}/c^2$. The χ_{DTF}^2 of the fit, which has 3 degrees of freedom, is required to be less than 15. Multiple B_s^0 candidates are found in less than 2.0% of selected events.

3.5 Selection of $\Lambda_b^0 \rightarrow J/\psi \Lambda$ decays

The selection of $\Lambda_b^0 \rightarrow J/\psi \Lambda$ candidates follows a similar approach to that adopted for $B^0 \rightarrow J/\psi K_s^0$ decays. Only downstream protons and pions are used to reconstruct the Λ candidates. The pions are required to have p_T larger than $0.1 \text{ GeV}/c$, while pions and protons must have p larger than $2 \text{ GeV}/c$. The Λ candidate must be well separated from the Λ_b^0 decay vertex and have p_T larger than $1 \text{ GeV}/c$. The χ^2 of the Λ vertex fit must be less than 25 and $m(p\pi^-)$ must be within $6 \text{ MeV}/c^2$ of the known Λ mass [44]. For subsequent stages of the selection, $m(p\pi^-)$ is constrained to the known Λ mass.

The invariant mass, $m(J/\psi \Lambda)$, of the J/ψ and Λ candidate combination must be in the range $[5470, 5770] \text{ MeV}/c^2$. The χ_{DTF}^2 of the fit, which has 6 degrees of freedom, is required to be less than 30. Multiple Λ_b^0 candidates are found in less than 0.5% of selected events.

4 Dependence of efficiencies on decay time

Section 3 described the reconstruction and selection criteria of the $H_b \rightarrow J/\psi X$ decays and various techniques that have been used to minimise the dependence of selection efficiencies upon the decay time. After these steps, there remain two effects that distort the b -hadron

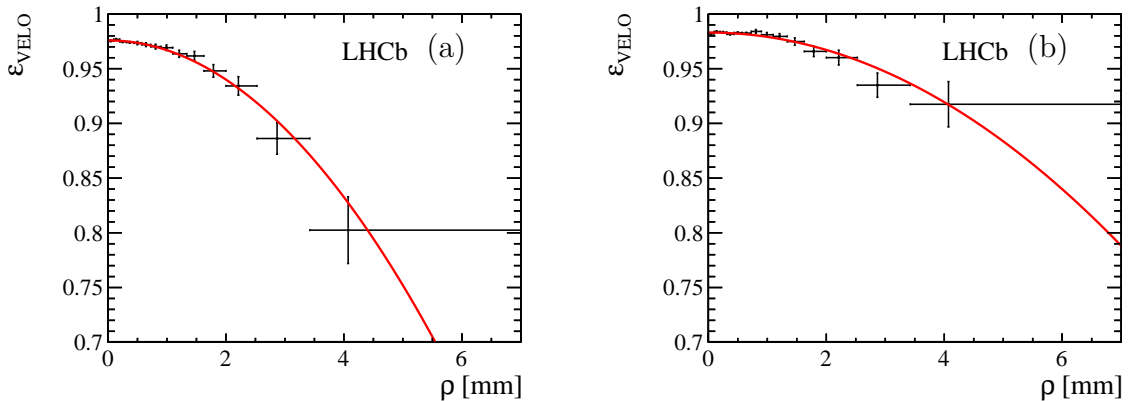


Figure 3: VELO-track reconstruction efficiency for kaon tracks reconstructed using the (a) online and (b) offline algorithms as a function of the kaon ρ , as defined in Eq. (3). The red solid lines show the result of an unbinned maximum likelihood fit using the parameterisation in Eq. (4) to the background subtracted data (black points).

decay time distribution. These are caused by the VELO-track reconstruction efficiency, $\varepsilon_{\text{VELO}}$, and the combination of the trigger efficiency, $\varepsilon_{\text{trigger}}$, and offline selection efficiency, $\varepsilon_{\text{selection|trigger}}$. This section will describe these effects and the techniques that are used to evaluate the efficiencies from data control samples.

4.1 VELO-track reconstruction efficiency

The largest variation of the efficiency with the decay time is introduced by the track reconstruction in the VELO. The track finding procedure in the VELO assumes that tracks originate approximately from the interaction region [33,45]. In the case of long-lived b -hadron candidates this assumption is not well justified, leading to a loss of reconstruction efficiency for charged particle tracks from the b -hadron decay.

The distance of closest approach of the track to the z -axis is defined as

$$\rho \equiv \frac{|(\mathbf{d} - \mathbf{v}) \cdot (\mathbf{p} \times \hat{\mathbf{z}})|}{|\mathbf{p} \times \hat{\mathbf{z}}|}, \quad (3)$$

where \mathbf{p} is the momentum of the final-state track from a b -hadron candidate decaying at point \mathbf{d} , $\hat{\mathbf{z}}$ is a unit vector along the z -axis and \mathbf{v} is the origin of the VELO coordinate system. During data taking the position of the LHCb VELO is monitored as a function of time and is centred around the LHC beam line. Using a control sample of $B^+ \rightarrow J/\psi K^+$ candidates where the K^+ is reconstructed as a downstream track, the VELO-track reconstruction efficiency, $\varepsilon_{\text{VELO}}(\rho)$, is computed as the fraction of these tracks that are also reconstructed as long tracks. From samples of simulated b -hadron decays, it is observed that $\varepsilon_{\text{VELO}}(\rho)$ can be empirically parameterised by

$$\varepsilon_{\text{VELO}}(\rho) = a(1 + c\rho^2), \quad (4)$$

Table 3: VELO reconstruction efficiency in data for kaon tracks reconstructed with the online and offline algorithms. In both cases, the correlation coefficient between a and c is 0.2.

	a	c [mm ⁻²]
Online	0.9759 ± 0.0005	-0.0093 ± 0.0007
Offline	0.9831 ± 0.0004	-0.0041 ± 0.0005

where the parameters a and c are determined from a fit to the unbinned efficiency distribution.

Figure 3 shows the VELO-track reconstruction efficiency obtained using this method and Table 3 shows the corresponding fit results. Since different configurations of the VELO reconstruction algorithms are used within the LHCb software trigger (online) and during the subsequent processing (offline), it is necessary to evaluate two different efficiencies. The stronger dependence of the online efficiency as a function of ρ is due to the additional requirements used in the first stage of the software trigger such that it satisfies the required processing time.

Applying the same technique to a simulated sample of $B^+ \rightarrow J/\psi K^+$ decays yields qualitatively similar behaviour for $\varepsilon_{\text{VELO}}(\rho)$. Studies on simulated data show that the efficiency for kaons and pions from the decay of ϕ and K^{*0} mesons is smaller than for the kaon in $B^+ \rightarrow J/\psi K^+$ decays, due to the small opening between the particles in the ϕ and K^{*0} decays, as discussed in Sec. 3. In addition, there are kinematic differences between the calibration B^+ sample and the signal samples. Scaling factors on the efficiency parameters are derived from simulation to account for these effects, and have typical sizes in the range [1.04, 1.65], depending on the decay mode and final-state particle being considered.

The distortion to the b -hadron candidate decay time distribution caused by the VELO-track reconstruction is corrected for by weighting each b -hadron candidate by the inverse of the product of the per-track efficiencies. The systematic effect introduced by this weighting is tested using simulated samples of each channel. The chosen efficiency depends on whether the particle is reconstructed with the online or offline variant of the algorithm. Studies on simulated data show that tracks found by the online tracking algorithm are also found by the offline tracking efficiency. For example, the efficiency weight for each $B^0 \rightarrow J/\psi K^{*0}$ candidate takes the form

$$w_{B^0 \rightarrow J/\psi K^{*0}} = 1 / \left(\varepsilon_{\text{VELO,online}}^{\mu^+} \varepsilon_{\text{VELO,online}}^{\mu^-} \varepsilon_{\text{VELO,offline}}^{K^+} \varepsilon_{\text{VELO,offline}}^{\pi^-} \right), \quad (5)$$

since the two muons are required to be reconstructed online, while the kaons and the pions are reconstructed offline.

In the case of the $B^0 \rightarrow J/\psi K_s^0$ and $\Lambda_b^0 \rightarrow J/\psi \Lambda$ channels, since no VELO information is used when reconstructing the K_s^0 and Λ particles, the candidate weighting functions take the form $w = 1 / \left(\varepsilon_{\text{VELO,online}}^{\mu^+} \varepsilon_{\text{VELO,online}}^{\mu^-} \right)$.

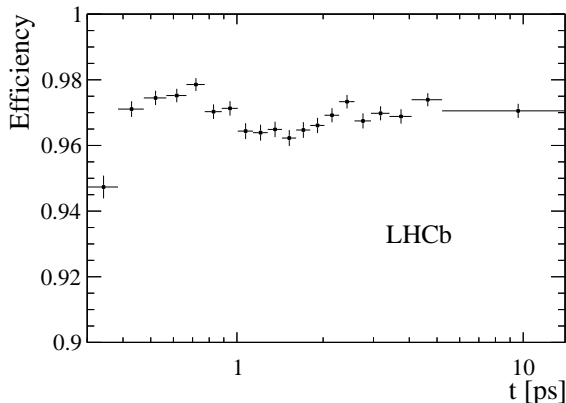


Figure 4: Combined trigger and selection efficiency, $\varepsilon_{\text{selection}}(t)$, for $B^+ \rightarrow J/\psi K^+$ candidates.

4.2 Trigger and selection efficiency

The efficiency of the second stage of the software trigger depends on the b -hadron decay time as it requires that the J/ψ meson is significantly displaced from the PV. A parameterisation of this efficiency, $\varepsilon_{\text{trigger}}(t)$, is obtained for each $b \rightarrow J/\psi X$ decay mode by exploiting a corresponding sample of $b \rightarrow J/\psi X$ candidates that are selected without any displacement requirement. For each channel, the control sample corresponds to approximately 40% of the total number of signal candidates. A maximum likelihood fit to the unbinned invariant mass distribution $m(J/\psi X)$ is performed to determine the fraction of signal decays that survive the decay-time biasing trigger requirements as a function of decay time.

The same technique is used to determine the decay time efficiency of the triggered candidates caused by the offline selection, $\varepsilon_{\text{selection|trigger}}(t)$, which is introduced by the requirement on the detachment of the J/ψ mesons in the sample used to reconstruct the b -hadron decays. The combined selection efficiency, $\varepsilon_{\text{selection}}(t)$, is given by the product of $\varepsilon_{\text{trigger}}(t)$ and $\varepsilon_{\text{selection|trigger}}(t)$.

Figure 4 shows $\varepsilon_{\text{selection}}(t)$ obtained for the $B^+ \rightarrow J/\psi K^+$ channel as a function of decay time. The efficiencies obtained for the other $H_b \rightarrow J/\psi X$ channels are qualitatively similar. Studies using simulated events show that the efficiency drop below 0.5 ps is caused by the J/ψ displacement requirement. The dip near 1.5 ps appears because the PV reconstruction in the software trigger is such that some final-state tracks of short-lived b -hadron decays may be used to reconstruct an additional fake PV close to the true b -hadron decay vertex. As a result the reconstructed J/ψ meson does not satisfy the displacement requirement, leading to a decrease in efficiency.

The efficiency parameterisation for each channel is used in the fit to measure the corresponding b -hadron lifetime. An exception is made for the $\Lambda_b^0 \rightarrow J/\psi \Lambda$ channel where, owing to its smaller event yield, $\varepsilon_{\text{selection}}(t)$ measured with $B^0 \rightarrow J/\psi K_s^0$ decays is used instead. The validity of this approach is checked using large samples of simulated events.

5 Maximum likelihood fit

For each channel, the lifetime is determined from a two-dimensional maximum likelihood fit to the unbinned $m(J/\psi X)$ and t distributions. The full probability density function (PDF) is constructed as $\mathcal{P} = f_s(\mathcal{S}_m \times \mathcal{S}_t) + (1 - f_s)(\mathcal{B}_m \times \mathcal{B}_t)$, where f_s is the signal fraction, determined in the fit, and $\mathcal{S}_m \times \mathcal{S}_t$ and $\mathcal{B}_m \times \mathcal{B}_t$ are the $(m(J/\psi X), t)$ PDFs for the signal and background components, respectively. A systematic uncertainty is assigned to the assumption that the PDFs factorise.

The signal mass PDF, \mathcal{S}_m , is modelled by the sum of two Gaussian functions. The free parameters in the fit are the common mean, the width of the narrower Gaussian function, the ratio of the second to the first Gaussian width and the fraction of the first Gaussian function. The background mass distribution, \mathcal{B}_m , is modelled by an exponential function with a single free parameter.

The signal b -hadron decay time distribution is described by an exponential function with decay constant given by the b -hadron lifetime, $\tau_{H_b \rightarrow J/\psi X}$. The signal decay time PDF, \mathcal{S}_t , is obtained by multiplying the exponential function by the combined t -dependent trigger and selection efficiency described in Sec. 4.2. From inspection of events in the sidebands of the b -hadron signal peak, the background decay time PDF, \mathcal{B}_t , is well modelled by a sum of three exponential functions with different decay constants that are free in the fit. These components originate from a combination of prompt candidates, where all tracks originate from the same PV, and long-lived candidates where tracks from the associated PV are combined with other tracks of long-lived particles. For each channel the exponential functions are convolved with a Gaussian resolution function with width σ and mean Δ , an offset of the order of a few femtoseconds that is fixed in the fit. Using a sample of prompt J/ψ background events, the decay time resolution for $H_b \rightarrow J/\psi X$ channels reconstructed using long tracks has been measured to be approximately 45 fs [46]. For $B^0 \rightarrow J/\psi K_s^0$ and $\Lambda_b^0 \rightarrow J/\psi \Lambda$ decays, which use downstream tracks to reconstruct the K_s^0 and Λ particles, a similar study of an event sample composed of prompt J/ψ mesons combined with two downstream tracks, reconstructed as either a K_s^0 or Λ , has determined the resolution to be 65 fs. The systematic uncertainties related to the choice of resolution model are discussed in Sec. 6.

The negative log-likelihood, constructed as

$$-\ln \mathcal{L} = -\alpha \sum_{\text{events } i} w_i \ln \mathcal{P}, \quad (6)$$

is minimised in the fit, where the weights w_i correspond to the per-candidate correction for the VELO reconstruction efficiency described in Sec. 4.1. The factor $\alpha = \sum_i w_i / \sum_i w_i^2$ is used to include the effect of the weights in the determination of the uncertainties [47]. Figures 1 and 2 show the result of fitting this model to the selected candidates for each channel, projected onto the corresponding $m(J/\psi X)$ and t distributions.

As a consistency check, an alternative fit procedure is developed where each event is given a signal weight, W_i , determined using the *sPlot* [48] method with $m(J/\psi X)$ as the discriminating variable and using the mass model described above. A weighted fit to the

decay time distribution using the signal PDF is then used to measure the b -hadron lifetime. In this case, the negative log-likelihood is given by Eq. (6) where w_i is replaced with $W_i w_i$ and $\alpha = \sum_i (W_i w_i) / \sum_i (W_i w_i)^2$. The difference between the results of the two fitting procedures is used to estimate the systematic uncertainty on the background description.

6 Systematic uncertainties

The systematic effects affecting the measurements reported here are discussed in the following and summarised in Tables 4 and 5.

The systematic uncertainty related to the VELO-track reconstruction efficiency can be split into two components. The first uncertainty is due to the finite size of the $B^+ \rightarrow J/\psi K^+$ sample, reconstructed using downstream kaon tracks, which is used to determine the per-candidate efficiency weights and leads to a statistical uncertainty on the $\varepsilon_{\text{VELO}}(\rho)$ parameterisation. The lifetime fits are repeated after varying the parameters by $\pm 1\sigma$ and the largest difference between the lifetimes is assigned as the uncertainty. The second uncertainty is due to the scaling factors, which are used to correct the efficiency for phase-space effects, obtained from simulated events. The fit is repeated using the unscaled efficiency and half of the variation in fit results is assigned as a systematic uncertainty. These contributions, of roughly the same size, are added in quadrature in Table 4.

A number of additional consistency checks are performed to investigate possible mismodelling of the VELO-track reconstruction efficiency. First, $\varepsilon_{\text{VELO}}(\rho)$ is evaluated in two track momentum and two track multiplicity bins and the event weights recalculated. Using both data and simulated events, no significant change in the lifetimes is observed after repeating the fit with the updated weights and, therefore, no systematic uncertainty is assigned. Secondly, to assess the sensitivity to the choice of parameterisation for $\varepsilon_{\text{VELO}}(\rho)$ (Eq. 4), the results are compared to those with linear model for the efficiency. The effect is found to be negligible and no systematic uncertainty is applied. Thirdly, the dependence of the VELO-track reconstruction efficiency on the azimuthal angle, ϕ , of each track is studied by independently evaluating the efficiency in four ϕ quadrants for both data and simulation. No dependence is observed. Finally, the efficiency is determined separately for both positive and negative kaons and found to be compatible.

The techniques described in Sec. 4 to correct the efficiency as a function of the decay time are validated on simulated data. The lifetime is fit in each simulated signal mode and the departure from the generated lifetime, $\Delta\tau$, is found to be compatible with zero within the statistical precision of each simulated sample. The measured lifetimes in the data sample are corrected by each $\Delta\tau$ and a corresponding systematic uncertainty is assigned, given by the size of the statistical uncertainty on the fitted lifetime for each simulated signal mode.

The assumption that $m(J/\psi X)$ is independent of the decay time is central to the validity of the likelihood fits used in this study. It is tested by re-evaluating the signal weights of the alternative fit in bins of decay time and then refitting the entire sample using the modified weights. The systematic uncertainty for each decay mode is evaluated

as the sum in quadrature of the lifetime variations, each weighted by the fraction of signal events in the corresponding bin.

For each signal decay mode, the effect of the limited size of the control sample used to estimate the combined trigger and selection efficiency is evaluated by repeating the fits with $\varepsilon_{\text{selection}}(t)$ randomly fluctuated within its statistical uncertainty. The standard deviation of the distribution of lifetimes obtained is assigned as the systematic uncertainty.

The alternative likelihood fit does not assume any model for the decay time distribution associated with the combinatorial background. Therefore, the systematic uncertainty associated to the modelling of this background is evaluated by taking the difference in lifetimes measured by the nominal and alternative fit methods.

The fit uses a double Gaussian function to describe the $m(J/\psi X)$ distribution of signal candidates. This assumption is tested by repeating the fit using a double-sided Apollonios function [49] where the mean and width parameters are varied in the fit and the remaining parameters are fixed to those from simulation. The differences in lifetime with respect to the default results are taken as systematic uncertainties.

As described in Sec. 5 the dominant background in each channel is combinatorial in nature. It is also possible for backgrounds to arise due to misreconstruction of b -hadron decays where the particle identification has failed. The presence of such backgrounds is checked by inspecting events in the sidebands of the signal and re-assigning the mass hypotheses of at least one of the final-state hadrons. The only contributions that have an impact are $\Lambda_b^0 \rightarrow J/\psi pK^-$ decays in the $B_s^0 \rightarrow J/\psi \phi$ channel where a proton is misidentified as a kaon and the cross-feed component between $B^0 \rightarrow J/\psi K_s^0$ and $\Lambda_b^0 \rightarrow J/\psi \Lambda$ decays where pion and protons are misidentified. In the case of $B_s^0 \rightarrow J/\psi \phi$ decays, the fit is repeated including a contribution of $\Lambda_b^0 \rightarrow J/\psi pK^-$ decays. The two-dimensional PDF is determined from simulation, while the yield is found to be 6% from the sidebands of the B_s^0 sample. This leads to the effective lifetime changing by 0.4 fs, which is assigned as a systematic uncertainty. A similar procedure is used to determine the invariant mass shape of the cross-feed background between $B^0 \rightarrow J/\psi K_s^0$ and $\Lambda_b^0 \rightarrow J/\psi \Lambda$ decays, while the decay time is modelled with the exponential distribution of the corresponding signal mode. A simultaneous fit to both data samples is performed in order to constrain the yield of the cross-feed and the resulting change in lifetime of -0.3 fs and $+1.1$ fs for B^0 and Λ_b^0 , respectively, is assigned as a systematic uncertainty.

Another potential source of background is the incorrect association of signal b hadrons to their PV, which results in an erroneous reconstruction of the decay time. Since the fitting procedure ignores this contribution, a systematic uncertainty is evaluated by repeating the fit after including in the background model a component describing the incorrectly associated candidates. The background distribution is determined by calculating the decay time for each $B^+ \rightarrow J/\psi K^+$ decay with respect to a randomly chosen PV from the previous selected event. In studies of simulated events the fraction of this background is less than 0.1%. Repeating the fit with a 1% contribution results in the lifetime changing by 0.1 fs and, therefore, no systematic uncertainty is assigned.

The measurement of the effective lifetime in the $B_s^0 \rightarrow J/\psi \phi$ channel is integrated over the angular distributions of the final-state particles and is, in the case of uniform angular

efficiency, insensitive to the different polarisations of the final state [46]. To check if the angular acceptance introduced by the detector geometry and event selection can affect the measured lifetime, the events are weighted by the inverse of the angular efficiency determined in Ref. [46]. Repeating the fit with the weighted dataset leads to a shift of the lifetime of -1.0 fs, the same as is observed in simulation. The final result is corrected by this shift, which is also assigned as a systematic uncertainty. The B_s^0 effective lifetime could also be biased due to a small CP -odd S-wave component from $B_s^0 \rightarrow J/\psi K^+ K^-$ decays that is ignored in the fit. For the $m(K^+ K^-)$ mass range used here (Sec. 3), Ref. [50] indicates that the S-wave contribution is 1.1%. The effect of ignoring such a component is evaluated by repeating the fit on simulated experiments with an additional 1% CP -odd component. A change in the lifetime of -1.2 fs is observed, which is used to correct the final lifetime and is also taken as a systematic uncertainty. Finally, as described in Sec. 3, only events with a decay time larger than 0.3 ps are considered in the nominal fit. This offset leads to a different relative contribution of the heavy and light mass eigenstates such that the lifetime extracted from the exponential fit does not correspond to the effective lifetime defined in Eq. (2). A correction of -0.3 fs is applied to account for this effect.

The presence of a production asymmetry between B^0 and \bar{B}^0 mesons could bias the measured $B^0 \rightarrow J/\psi K_s^0$ effective lifetime, and therefore $\Delta\Gamma_d/\Gamma_d$, by adding additional terms in Eq. (2). The production asymmetry is measured to be $A_P(B^0) = (0.6 \pm 0.9)\%$ [51], the uncertainty of which is used to estimate a corresponding systematic uncertainty on the $B^0 \rightarrow J/\psi K_s^0$ lifetime of 1.1 fs. No uncertainty is assigned to the $B^0 \rightarrow J/\psi K^{*0}$ lifetime since this decay mode is flavour-specific² and the production asymmetry cancels in the untagged decay rate. For the B_s^0 system, the rapid oscillations, due to the large value of $\Delta m_s = 17.768 \pm 0.024$ ps⁻¹ [52], reduce the effect of a production asymmetry, reported as $A_P(B_s^0) = (7 \pm 5)\%$ in Ref. [51], to a negligible level. Hence, no corresponding systematic uncertainty is assigned.

There is a 0.02% relative uncertainty on the lifetime measurements due to the uncertainty on the length scale of LHCb [52], which is mainly determined by the VELO modules z positions. These are evaluated by a survey, having an accuracy of 0.1 mm over the full length of the VELO (1000 mm), and refined through a track-based alignment. The alignment procedure is more precise for the first track hits, that are less affected by multiple scattering and whose distribution of z positions have an RMS of 100 mm. In this region, the differences between the module positions obtained from the survey and track-based alignment are within 0.02 mm, which is taken as systematic uncertainty. The systematic uncertainty related to the momentum scale calibration affects both the b hadron candidate mass and momentum and, therefore, cancels when computing the decay time.

The systematic uncertainty related to the choice of 45 fs for the width of the decay-time resolution function (65 fs in the case of $B^0 \rightarrow J/\psi K_s^0$ and $\Lambda_b^0 \rightarrow J/\psi \Lambda$) is evaluated by changing the width by ± 15 fs and repeating the fit. This change in width is larger than the estimated uncertainty on the resolution and leads to a negligible change in the fit

²Flavour-specific means that the final state is only accessible via the decay of a $B_{(s)}^0$ meson and accessible by a meson originally produced as a $\bar{B}_{(s)}^0$ only via oscillation.

Table 4: Statistical and systematic uncertainties (in femtoseconds) for the values of the b -hadron lifetimes. The total systematic uncertainty is obtained by combining the individual contributions in quadrature.

Source	$\tau_{B^+ \rightarrow J/\psi K^+}$	$\tau_{B^0 \rightarrow J/\psi K^{*0}}$	$\tau_{B^0 \rightarrow J/\psi K_S^0}$	$\tau_{\Lambda_b^0 \rightarrow J/\psi \Lambda}$	$\tau_{B_s^0 \rightarrow J/\psi \phi}$
Statistical uncertainty	3.5	6.1	12.8	26.5	11.4
VELO reconstruction	2.0	2.3	0.9	0.5	2.3
Simulation sample size	1.7	2.3	2.9	3.7	2.4
Mass-time correlation	1.4	1.8	2.1	3.0	0.7
Trigger and selection eff.	1.1	1.2	2.0	2.0	2.5
Background modelling	0.1	0.2	2.2	2.1	0.4
Mass modelling	0.1	0.2	0.4	0.2	0.5
Peaking background	–	–	0.3	1.1	0.4
Effective lifetime bias	–	–	–	–	1.6
B^0 production asym.	–	–	1.1	–	–
LHCb length scale	0.4	0.3	0.3	0.3	0.3
Total systematic	3.2	3.9	4.9	5.7	4.6

results. Consequently, no systematic uncertainty is assigned. Furthermore, to test the sensitivity of the lifetimes to potential mismodelling of the long tails in the resolution, the resolution model is changed from a single Gaussian function to a sum of two or three Gaussian functions with parameters fixed from simulation. Repeating the fit with the new resolution model causes no significant change to the lifetimes and no systematic uncertainty is assigned. The lifetimes are insensitive to the offset, Δ , in the resolution model.

Several consistency checks are performed to study the stability of the lifetimes, by comparing the results obtained using different subsets of the data in terms of magnet polarity, data taking period, b -hadron and track kinematic variables, number of PVs in the event and track multiplicity. In all cases, no trend is observed and all lifetimes are compatible with the nominal results.

The majority of the systematic uncertainties described above can be propagated to the lifetime ratio measurements in Table 7. However, some of the uncertainties are correlated between the individual lifetimes and cancel in the ratio. For the first set of ratios and for $\Delta\Gamma_d/\Gamma_d$, the systematic uncertainty from the VELO-reconstruction efficiency weights and the LHCb length scale are considered as fully correlated. For the second set of ratios, other systematic uncertainties, as indicated in Table 5, cancel, since the ratio is formed from lifetimes measured using the same decay mode. In contrast to the situation for the measurement of the B^0 lifetime in the $B^0 \rightarrow J/\psi K^{*0}$ mode, the B^0 production asymmetry does lead to a systematic uncertainty on the measurement of $\tau_{B^0 \rightarrow J/\psi K^{*0}}/\tau_{\bar{B}^0 \rightarrow J/\psi \bar{K}^{*0}}$ since terms like $A_P \cos(\Delta m_d t)$ do not cancel in the decay rates describing the decays of B^0 and \bar{B}^0 mesons to $J/\psi K^{*0}$ and $J/\psi \bar{K}^{*0}$ final states. The effect of candidates where the flavour, via the particle identification of the decay products, has not been correctly assigned is investigated and found to be negligible.

Table 5: Statistical and systematic uncertainties (in units of 10^{-3}) for the lifetime ratios and $\Delta\Gamma_d/\Gamma_d$. For brevity, τ_{B^0} ($\tau_{\bar{B}^0}$) corresponds to the measurement of $\tau_{B^0 \rightarrow J/\psi K^{*0}}$ ($\tau_{\bar{B}^0 \rightarrow J/\psi \bar{K}^{*0}}$). The total systematic uncertainty is obtained by combining the individual contributions in quadrature.

Source	τ_{B^+}/τ_{B^0}	$\tau_{B_s^0}/\tau_{B^0}$	$\tau_{\Lambda_b^0}/\tau_{B^0}$	τ_{B^+}/τ_{B^-}	$\tau_{\Lambda_b^0}/\tau_{\bar{\Lambda}_b^0}$	$\tau_{B^0}/\tau_{\bar{B}^0}$	$\Delta\Gamma_d/\Gamma_d$
Statistical uncertainty	5.0	8.5	18.0	4.0	35.0	8.0	25.0
VELO reconstruction	1.6	1.7	1.1	–	–	–	4.1
Simulation sample size	2.0	2.2	2.8	2.1	5.3	3.0	6.3
Mass-time correlation	1.6	1.2	2.3	–	–	–	4.7
Trigger and selection eff.	1.1	1.8	1.5	–	–	–	4.0
Background modelling	0.3	0.1	1.5	0.2	3.0	1.4	3.8
Mass modelling	0.2	0.4	0.2	0.1	0.2	0.2	0.8
Peaking background	–	0.3	0.7	–	–	–	0.5
Effective lifetime bias	–	1.0	–	–	–	–	–
B^0 production asym.	–	–	–	–	–	8.5	1.9
Total systematic	3.2	3.7	4.4	2.1	6.1	9.1	10.7

Table 6: Fit results for the B^+ , B^0 , B_s^0 mesons and Λ_b^0 baryon lifetimes. The first uncertainty is statistical and the second is systematic.

Lifetime	Value [ps]
$\tau_{B^+ \rightarrow J/\psi K^+}$	$1.637 \pm 0.004 \pm 0.003$
$\tau_{B^0 \rightarrow J/\psi K^{*0}}$	$1.524 \pm 0.006 \pm 0.004$
$\tau_{B^0 \rightarrow J/\psi K_s^0}$	$1.499 \pm 0.013 \pm 0.005$
$\tau_{\Lambda_b^0 \rightarrow J/\psi \Lambda}$	$1.415 \pm 0.027 \pm 0.006$
$\tau_{B_s^0 \rightarrow J/\psi \phi}$	$1.480 \pm 0.011 \pm 0.005$

7 Results and conclusions

The measured b -hadron lifetimes are reported in Table 6. All results are compatible with existing world averages [13]. The reported $\tau_{\Lambda_b^0 \rightarrow J/\psi \Lambda}$ is smaller by approximately 2σ than a previous measurements from LHCb [8]. With the exception of the $\Lambda_b^0 \rightarrow J/\psi \Lambda$ channel, these are the single most precise measurements of the b -hadron lifetimes. The B_s^0 meson effective lifetime is measured using the same data set as used in Ref. [46] for the measurement of the B_s^0 meson mixing parameters and polarisation amplitudes in $B_s^0 \rightarrow J/\psi \phi$ decays. The B_s^0 meson effective lifetime computed from these quantities is compatible with the lifetime reported in this paper and a combination of the two results is, therefore, inappropriate.

Table 7 reports the ratios of the B^+ , B_s^0 and Λ_b^0 lifetimes to the B^0 lifetime measured in the flavour-specific $B^0 \rightarrow J/\psi K^{*0}$ channel. This decay mode provides a better normalisation than the $B^0 \rightarrow J/\psi K_s^0$ channel due to the lower statistical uncertainty on the B^0 meson lifetime and due to the fact that the $B^0 \rightarrow J/\psi K^{*0}$ lifetime only depends quadratically on $\Delta\Gamma_d/\Gamma_d$, as shown in Eq. (7). The statistical and systematic uncertainties from

Table 7: Lifetime ratios for the B^+ , B^0 , B_s^0 mesons and Λ_b^0 baryon. The first uncertainty is statistical and the second is systematic.

Ratio	Value
$\tau_{B^+}/\tau_{B^0 \rightarrow J/\psi K^{*0}}$	$1.074 \pm 0.005 \pm 0.003$
$\tau_{B_s^0}/\tau_{B^0 \rightarrow J/\psi K^{*0}}$	$0.971 \pm 0.009 \pm 0.004$
$\tau_{\Lambda_b^0}/\tau_{B^0 \rightarrow J/\psi K^{*0}}$	$0.929 \pm 0.018 \pm 0.004$
τ_{B^+}/τ_{B^-}	$1.002 \pm 0.004 \pm 0.002$
$\tau_{\Lambda_b^0}/\tau_{\bar{\Lambda}_b^0}$	$0.940 \pm 0.035 \pm 0.006$
$\tau_{B^0 \rightarrow J/\psi K^{*0}}/\tau_{\bar{B}^0 \rightarrow J/\psi \bar{K}^{*0}}$	$1.000 \pm 0.008 \pm 0.009$

the absolute lifetime measurements are propagated to the ratios, taking into account the correlations between the systematic uncertainties. All ratios are consistent with SM predictions [15, 22–25, 30–32] and with previous measurements [13]. Furthermore, the ratios τ_{B^+}/τ_{B^-} , $\tau_{\Lambda_b^0}/\tau_{\bar{\Lambda}_b^0}$ and $\tau_{B^0 \rightarrow J/\psi K^{*0}}/\tau_{\bar{B}^0 \rightarrow J/\psi \bar{K}^{*0}}$ are reported. Measuring any of these different from unity would indicate a violation of CPT invariance or, for $B^0 \rightarrow J/\psi K^{*0}$ decays, could also indicate that $\Delta\Gamma_d$ is non-zero and $B^0 \rightarrow J/\psi K^{*0}$ is not 100% flavour-specific. No deviation from unity of these ratios is observed.

The effective lifetimes of $B^0 \rightarrow J/\psi K^{*0}$ and $B^0 \rightarrow J/\psi K_s^0$ decays are used to measure $\Delta\Gamma_d/\Gamma_d$. Flavour-specific final states such as $B^0 \rightarrow J/\psi K^{*0}$ have $\mathcal{A}_{\Delta\Gamma_d}^{B^0 \rightarrow J/\psi K^{*0}} = 0$, while $\mathcal{A}_{\Delta\Gamma_d}^{B^0 \rightarrow J/\psi K_s^0} = \cos(2\beta)$ to a good approximation in the SM, where $\beta \equiv \arg[-(V_{cd}V_{cb}^*)/(V_{td}V_{tb}^*)]$ is one of the CKM unitarity triangle angles. Hence, the two effective lifetimes can be expressed as

$$\tau_{B^0 \rightarrow J/\psi K^{*0}} = \frac{1}{\Gamma_d} \frac{1}{1 - y_d^2} (1 + y_d^2), \quad (7)$$

$$\tau_{B^0 \rightarrow J/\psi K_s^0} = \frac{1}{\Gamma_d} \frac{1}{1 - y_d^2} \left(\frac{1 + 2 \cos(2\beta)y_d + y_d^2}{1 + \cos(2\beta)y_d} \right). \quad (8)$$

Using the effective lifetimes reported in Table 6 and $\beta = (21.5_{-0.7}^{+0.8})^\circ$ [13], a fit of $\Delta\Gamma_d$ and Γ_d to the expressions in Eq. (7) and Eq. (8) leads to

$$\Gamma_d = 0.656 \pm 0.003 \pm 0.002 \text{ ps}^{-1}, \quad (9)$$

$$\Delta\Gamma_d = -0.029 \pm 0.016 \pm 0.007 \text{ ps}^{-1}, \quad (10)$$

where the first uncertainty is statistical and the second is systematic. The correlation coefficient between $\Delta\Gamma_d$ and Γ_d is 0.43 when including statistical and systematic uncertainties. The combination gives

$$\frac{\Delta\Gamma_d}{\Gamma_d} = -0.044 \pm 0.025 \pm 0.011, \quad (11)$$

consistent with the SM expectation [14, 15] and the current world-average value [13].

Acknowledgements

We express our gratitude to our colleagues in the CERN accelerator departments for the excellent performance of the LHC. We thank the technical and administrative staff at the LHCb institutes. We acknowledge support from CERN and from the national agencies: CAPES, CNPq, FAPERJ and FINEP (Brazil); NSFC (China); CNRS/IN2P3 and Region Auvergne (France); BMBF, DFG, HGF and MPG (Germany); SFI (Ireland); INFN (Italy); FOM and NWO (The Netherlands); SCSR (Poland); MEN/IFA (Romania); MinES, Rosatom, RFBR and NRC “Kurchatov Institute” (Russia); MinECo, XuntaGal and GENCAT (Spain); SNSF and SER (Switzerland); NAS Ukraine (Ukraine); STFC (United Kingdom); NSF (USA). We also acknowledge the support received from the ERC under FP7. The Tier1 computing centres are supported by IN2P3 (France), KIT and BMBF (Germany), INFN (Italy), NWO and SURF (The Netherlands), PIC (Spain), GridPP (United Kingdom). We are indebted to the communities behind the multiple open source software packages we depend on. We are also thankful for the computing resources and the access to software R&D tools provided by Yandex LLC (Russia).

References

- [1] V. A. Khoze and M. A. Shifman, *Heavy quarks*, Sov. Phys. Usp. **26** (1983) 387.
- [2] M. A. Shifman and M. Voloshin, *Preasymptotic effects in inclusive weak decays of charmed particles*, Sov. J. Nucl. Phys. **41** (1985) 120.
- [3] M. A. Shifman and M. Voloshin, *Hierarchy of lifetimes of charmed and beautiful hadrons*, Sov. Phys. JETP **64** (1986) 698.
- [4] I. I. Bigi, N. Uraltsev, and A. Vainshtein, *Nonperturbative corrections to inclusive beauty and charm decays: QCD versus phenomenological models*, Phys. Lett. **B293** (1992) 430, arXiv: hep-ph/9207214.
- [5] I. I. Bigi, *The QCD perspective on lifetimes of heavy-flavor hadrons*, arXiv: hep-ph/9508408.
- [6] N. Uraltsev, *Heavy quark expansion in beauty and its decays*, arXiv: hep-ph/9804275.
- [7] M. Neubert, *B decays and the heavy-quark expansion*, Adv. Ser. Direct. High Energy Phys. **15** (1998) 239, arXiv: hep-ph/9702375.
- [8] LHCb collaboration, R. Aaij *et al.*, *Precision measurement of the Λ_b^0 baryon lifetime*, Phys. Rev. Lett. **111** (2013) 102003, arXiv: 1307.2476.
- [9] K. Hartkorn and H. Moser, *A new method of measuring $\Delta\Gamma/\Gamma$ in the B_s^0 anti- B_s^0 system*, Eur. Phys. J. **C8** (1999) 381.

- [10] I. Dunietz, R. Fleischer, and U. Nierste, *In pursuit of new physics with B_s decays*, Phys. Rev. **D63** (2001) 114015, arXiv: hep-ph/0012219.
- [11] R. Fleischer and R. Knegjens, *Effective lifetimes of B_s decays and their constraints on the B_s^0 - \bar{B}_s^0 mixing parameters*, Eur. Phys. J. **C71** (2011) 1789, arXiv: 1109.5115.
- [12] U. Nierste, *CP asymmetry in flavor-specific B decays*, arXiv: hep-ph/0406300.
- [13] Heavy Flavor Averaging Group, Y. Amhis *et al.*, *Averages of b-hadron, c-hadron, and τ -lepton properties as of early 2012*, arXiv: 1207.1158, updated results and plots available at: <http://www.slac.stanford.edu/xorg/hfag/>.
- [14] A. Lenz and U. Nierste, *Theoretical update of $B_s - \bar{B}_s$ mixing*, JHEP **06** (2007) 072, arXiv: hep-ph/0612167.
- [15] A. Lenz and U. Nierste, *Numerical updates of lifetimes and mixing parameters of B mesons*, arXiv: 1102.4274.
- [16] BaBar collaboration, B. Aubert *et al.*, *Limits on the decay-rate difference of neutral B mesons and on CP, T, and CPT violation in $B^0\bar{B}^0$ oscillations*, Phys. Rev. Lett. **92** (2004) 181801, arXiv: hep-ex/0311037.
- [17] BaBar collaboration, B. Aubert *et al.*, *Limits on the decay-rate difference of neutral B mesons and on CP, T, and CPT violation in $B^0\bar{B}^0$ oscillations*, Phys. Rev. **D70** (2004) 012007, arXiv: hep-ex/0403002.
- [18] Belle collaboration, T. Higuchi *et al.*, *Search for time-dependent CPT violation in hadronic and semileptonic B decays*, Phys. Rev. **D85** (2012) 071105, arXiv: 1203.0930.
- [19] G. Borissov and B. Hoeneisen, *Understanding the like-sign dimuon charge asymmetry in $p\bar{p}$ collisions*, Phys. Rev. **D87** (2013) 074020, arXiv: 1303.0175.
- [20] D0 collaboration, V. M. Abazov *et al.*, *Study of CP-violating charge asymmetries of single muons and like-sign dimuons in $p\bar{p}$ collisions*, Phys. Rev. **D89** (2014) 012002, arXiv: 1310.0447.
- [21] T. Gershon, *$\Delta\Gamma_d$: a forgotten null test of the standard model*, J. Phys. **G38** (2011) 015007, arXiv: 1007.5135.
- [22] M. Beneke *et al.*, *The $B^+ - B_d^0$ lifetime difference beyond leading logarithms*, Nucl. Phys. **B639** (2002) 389, arXiv: hep-ph/0202106.
- [23] E. Franco, V. Lubicz, F. Mescia, and C. Tarantino, *Lifetime ratios of beauty hadrons at the next-to-leading order in QCD*, Nucl. Phys. **B633** (2002) 212, arXiv: hep-ph/0203089.

- [24] M. Beneke, G. Buchalla, and I. Dunietz, *Width Difference in the $B_s - \bar{B}_s$ System*, Phys. Rev. **D54** (1996) 4419, arXiv: hep-ph/9605259.
- [25] Y.-Y. Keum and U. Nierste, *Probing penguin coefficients with the lifetime ratio $\tau(B_s)/\tau(B_d)$* , Phys. Rev. **D57** (1998) 4282, arXiv: hep-ph/9710512.
- [26] N. Uraltsev, *On the problem of boosting nonleptonic b baryon decays*, Phys. Lett. **B376** (1996) 303, arXiv: hep-ph/9602324.
- [27] I. I. Bigi, M. A. Shifman, and N. Uraltsev, *Aspects of heavy quark theory*, Ann. Rev. Nucl. Part. Sci. **47** (1997) 591, arXiv: hep-ph/9703290.
- [28] D. Pirjol and N. Uraltsev, *Four fermion heavy quark operators and light current amplitudes in heavy flavor hadrons*, Phys. Rev. **D59** (1999) 034012, arXiv: hep-ph/9805488.
- [29] M. Voloshin, *Reducing model dependence of spectator effects in inclusive decays of heavy baryons*, Phys. Rev. **D61** (2000) 074026, arXiv: hep-ph/9908455.
- [30] C. Tarantino, *Beauty hadron lifetimes and B meson CP violation parameters from lattice QCD*, Eur. Phys. J. **C33** (2004) S895, arXiv: hep-ph/0310241.
- [31] F. Gabbiani, A. I. Onishchenko, and A. A. Petrov, *Λ_b^0 lifetime puzzle in heavy quark expansion*, Phys. Rev. **D68** (2003) 114006, arXiv: hep-ph/0303235.
- [32] F. Gabbiani, A. I. Onishchenko, and A. A. Petrov, *Spectator effects and lifetimes of heavy hadrons*, Phys. Rev. **D70** (2004) 094031, arXiv: hep-ph/0407004.
- [33] LHCb collaboration, A. A. Alves Jr. *et al.*, *The LHCb detector at the LHC*, JINST **3** (2008) S08005.
- [34] M. Adinolfi *et al.*, *Performance of the LHCb RICH detector at the LHC*, Eur. Phys. J. **C73** (2013) 2431, arXiv: 1211.6759.
- [35] A. A. Alves Jr *et al.*, *Performance of the LHCb muon system*, JINST **8** (2013) P02022, arXiv: 1211.1346.
- [36] R. Aaij *et al.*, *The LHCb trigger and its performance in 2011*, JINST **8** (2013) P04022, arXiv: 1211.3055.
- [37] T. Sjöstrand, S. Mrenna, and P. Skands, *PYTHIA 6.4 physics and manual*, JHEP **05** (2006) 026, arXiv: hep-ph/0603175.
- [38] I. Belyaev *et al.*, *Handling of the generation of primary events in GAUSS, the LHCb simulation framework*, Nuclear Science Symposium Conference Record (NSS/MIC) **IEEE** (2010) 1155.

- [39] D. J. Lange, *The EVTGEN particle decay simulation package*, Nucl. Instrum. Meth. **A462** (2001) 152.
- [40] P. Golonka and Z. Was, *PHOTOS Monte Carlo: a precision tool for QED corrections in Z and W decays*, Eur. Phys. J. **C45** (2006) 97, arXiv: hep-ph/0506026.
- [41] GEANT4 collaboration, J. Allison *et al.*, *GEANT4 developments and applications*, IEEE Trans. Nucl. Sci. **53** (2006) 270; GEANT4 collaboration, S. Agostinelli *et al.*, *GEANT4: a simulation toolkit*, Nucl. Instrum. Meth. **A506** (2003) 250.
- [42] M. Clemencic *et al.*, *The LHCb simulation application, GAUSS: design, evolution and experience*, J. Phys.: Conf. Ser. **331** (2011) 032023.
- [43] W. D. Hulsbergen, *Decay chain fitting with a Kalman filter*, Nucl. Instrum. Meth. **A552** (2005) 566, arXiv: physics/0503191.
- [44] Particle Data Group, J. Beringer *et al.*, *Review of particle physics*, Phys. Rev. **D86** (2012) 010001, and 2013 partial update for the 2014 edition.
- [45] O. Callot, *FastVelo, a fast and efficient pattern recognition package for the Velo*, LHCb-PUB-2011-001.
- [46] LHCb collaboration, R. Aaij *et al.*, *Measurement of CP-violation and the B_s^0 -meson decay width difference with $B_s^0 \rightarrow J/\psi K^+ K^-$ and $B_s^0 \rightarrow J/\psi \pi^+ \pi^-$ decays*, Phys. Rev. **D87** (2013) 112010, arXiv: 1304.2600.
- [47] Y. Xie, *sFit: a method for background subtraction in maximum likelihood fit*, arXiv: 0905.0724.
- [48] M. Pivk and F. R. Le Diberder, *sPlot: a statistical tool to unfold data distributions*, Nucl. Instrum. Meth. **A555** (2005) 356, arXiv: physics/0402083.
- [49] D. M. Santos and F. Dupertuis, *Mass distributions marginalized over per-event errors*, submitted to Nucl. Instrum. Meth. A (2013) arXiv: 1312.5000.
- [50] LHCb collaboration, R. Aaij *et al.*, *Amplitude analysis and branching fraction measurement of $\bar{B}_s^0 \rightarrow J/\psi K^+ K^-$* , Phys. Rev. **D87** (2013) 072004, arXiv: 1302.1213.
- [51] LHCb collaboration, R. Aaij *et al.*, *First measurement of time-dependent CP violation in $B_s^0 \rightarrow K^+ K^-$ decays*, JHEP **10** (2013) 183, arXiv: 1308.1428.
- [52] LHCb collaboration, R. Aaij *et al.*, *Precision measurement of the $B_s^0 - \bar{B}_s^0$ oscillation frequency Δm_s in the decay $B_s^0 \rightarrow D_s^+ \pi^-$* , New J. Phys. **15** (2013) 053021, arXiv: 1304.4741.



Test of lepton universality with $\Lambda_b^0 \rightarrow pK^- \ell^+ \ell^-$ decays

LHCb collaboration[†]

Abstract

The ratio of branching fractions of the decays $\Lambda_b^0 \rightarrow pK^- e^+ e^-$ and $\Lambda_b^0 \rightarrow pK^- \mu^+ \mu^-$, R_{pK}^{-1} , is measured for the first time using proton-proton collision data corresponding to an integrated luminosity of 4.7 fb^{-1} recorded with the LHCb experiment at center-of-mass energies of 7, 8 and 13 TeV. In the dilepton mass-squared range $0.1 < q^2 < 6.0 \text{ GeV}^2/c^4$ and the pK^- mass range $m(pK^-) < 2600 \text{ MeV}/c^2$, the ratio of branching fractions is measured to be $R_{pK}^{-1} = 1.17_{-0.16}^{+0.18} \pm 0.07$, where the first uncertainty is statistical and the second systematic. This is the first test of lepton universality with b baryons and the first observation of the decay $\Lambda_b^0 \rightarrow pK^- e^+ e^-$.

Submitted to JHEP

© 2019 CERN for the benefit of the LHCb collaboration. CC-BY-4.0 licence.

[†]Authors are listed at the end of this paper.

1 Introduction

Decays involving $b \rightarrow s\ell^+\ell^-$ transitions, where ℓ^\pm represents a lepton, are mediated by flavour-changing neutral currents (FCNC). Since FCNCs are forbidden at tree level in the Standard Model (SM) and can only proceed through amplitudes involving electroweak loop (penguin and box) Feynman diagrams, these transitions are an ideal place to search for effects beyond the SM. The potential contributions of new particles to these processes can be manifested as modifications in the rate of particular decay modes, or changes in the angular distribution of the final-state particles. Hints for possible disagreement with the SM have been reported, for example in several measurements of angular observables [1–4] of rare $b \rightarrow s\ell^+\ell^-$ decays. The SM predictions of these quantities are affected by hadronic uncertainties and more precisely predicted observables are desirable.

In the SM, the electroweak couplings of the charged leptons are independent of their flavour. The properties of decays to leptons of different flavours are expected to be the same up to corrections related to the lepton mass. This property, referred to as Lepton Universality (LU), has already been tested in B -meson decays by measuring the ratio

$$R_H \equiv \frac{\int \frac{d\Gamma(B \rightarrow H\mu^+\mu^-)}{dq^2} dq^2}{\int \frac{d\Gamma(B \rightarrow He^+e^-)}{dq^2} dq^2}, \quad (1)$$

where H represents a hadron containing an s quark, such as a K or a K^* meson. The decay rate, Γ , is integrated over a range of the squared dilepton invariant masses, q^2 . The R_H ratios allow for very precise tests of LU, as hadronic uncertainties cancel in their theoretical predictions. In the SM, they are expected to be close to unity with $\mathcal{O}(1\%)$ precision [5].

At e^+e^- machines operating at the $\Upsilon(4S)$ resonance, the ratios $R_{K^{(*)}}$ have been measured to be consistent with unity with a precision between 20 and 50% [6–9]. The most precise measurements of R_K in the q^2 range between 1.1 and 6.0 GeV²/c⁴ and R_{K^*0} in the regions $0.045 < q^2 < 1.1$ GeV²/c⁴ and $1.1 < q^2 < 6.0$ GeV²/c⁴ have been performed by the LHCb collaboration and, depending on the theoretical prediction used, are respectively 2.5 [10], 2.1–2.3 and 2.4–2.5 [11] standard deviations below their SM expectations [5, 12–21]. Further tests of LU in other $b \rightarrow s\ell^+\ell^-$ transitions are therefore critical to improve the statistical significance of the measurement and to understand the origin of any discrepancies. At the LHC, Λ_b^0 baryons are produced abundantly and $b \rightarrow s\ell^+\ell^-$ transitions can also be studied in their decays. The full set of angular observables in $\Lambda_b^0 \rightarrow \Lambda\mu^+\mu^-$ decays has been measured in Ref. [22] and CP asymmetries have been determined using $\Lambda_b^0 \rightarrow pK^-\mu^+\mu^-$ decays [23].

This paper presents the first test of LU in the baryon sector, through the measurement of the ratio of branching fractions for $\Lambda_b^0 \rightarrow pK^-\mu^+\mu^-$ and $\Lambda_b^0 \rightarrow pK^-e^+e^-$ decays,¹ R_{pK} . Both the experimental signature of the decays and the large data sample available motivate the choice of $\Lambda_b^0 \rightarrow pK^-\ell^+\ell^-$ decays for this study. Similarly to other R_H ratios, R_{pK} is expected to be close to unity in the SM [24].

The complementarity between R_K and R_{K^*0} measurements in constraining different types of new physics scenarios is widely discussed in the literature, see for example Ref. [25]. The spin one-half of the Λ_b^0 baryon and the rich resonant structure of the pK^- hadronic system [23, 26] indicate a similar situation in $\Lambda_b^0 \rightarrow pK^-\ell^+\ell^-$ decays, where complementary

¹The inclusion of charge-conjugate processes is implied throughout this paper.

constraints could be derived once the pK^- resonant structures are analysed. Following the observations of Ref. [23] on the hadronic system, this analysis is restricted to invariant masses $m(pK^-) < 2.6 \text{ GeV}/c^2$, where most of the signal occurs. The analysis is performed in a wide q^2 region between $0.1 \text{ GeV}^2/c^4$ and $6.0 \text{ GeV}^2/c^4$. The lower boundary is chosen to be far enough from the dimuon kinematic threshold so that the effect of radiative corrections is negligible on the R_{pK} ratio, using similar arguments to those discussed in Ref. [5]. The upper boundary is set to reduce contamination from the radiative tail of the J/ψ resonance. Contamination from $\Lambda_b^0 \rightarrow pK^- \phi (\rightarrow \ell^+ \ell^-)$ decays is estimated to be negligible, therefore no veto around the ϕ mass is applied to the dilepton spectrum.

Relying on the well-tested LU in $J/\psi \rightarrow \ell^+ \ell^-$ decays [27], the measurement is performed as a double ratio of the branching fractions of the $\Lambda_b^0 \rightarrow pK^- \ell^+ \ell^-$ and $\Lambda_b^0 \rightarrow pK^- J/\psi (\rightarrow \ell^+ \ell^-)$ decays:

$$R_{pK}^{-1} = \frac{\mathcal{B}(\Lambda_b^0 \rightarrow pK^- e^+ e^-)}{\mathcal{B}(\Lambda_b^0 \rightarrow pK^- J/\psi (\rightarrow e^+ e^-))} \bigg/ \frac{\mathcal{B}(\Lambda_b^0 \rightarrow pK^- \mu^+ \mu^-)}{\mathcal{B}(\Lambda_b^0 \rightarrow pK^- J/\psi (\rightarrow \mu^+ \mu^-))}, \quad (2)$$

where the two decay channels are also referred to as the “nonresonant” and the “resonant” modes, respectively. Due to the similarity between the experimental effects on the nonresonant and resonant decay modes, many sources of systematic uncertainty are substantially reduced in the double ratio. This approach helps to mitigate the significant differences in reconstruction between decays with muons or electrons in the final state, which are mostly due to bremsstrahlung emission and the trigger response.

The experimental quantities relevant for the LU measurement are the yields and the reconstruction and selection efficiencies of the four decays entering the double ratio. The definition of R_{pK}^{-1} ensures that the smaller electron yields are placed in the numerator, granting a likelihood function with a more symmetrical distribution. In order to avoid experimental biases, a blind analysis is performed. In addition to the determination of the R_{pK}^{-1} ratio, this analysis provides the first measurement of the $\Lambda_b^0 \rightarrow pK^- \mu^+ \mu^-$ branching fraction and the first observation of the $\Lambda_b^0 \rightarrow pK^- e^+ e^-$ decay. Due to the lack of information on the exact resonant content in the pK^- spectrum, it is challenging to compute the expected branching fraction of these decays in the SM, for which no prediction has been found in the literature. Predictions for specific excited Λ resonances, Λ^* , in the decays $\Lambda_b^0 \rightarrow \Lambda^* \ell^+ \ell^-$ with $\Lambda^* \rightarrow pK^-$, have been computed [28, 29] but cannot be directly compared to this result.

This paper is organised as follows: Sec. 2 describes the LHCb detector, as well as the data and the simulation samples used in this analysis; the sources of background and selection procedure of the signal candidates are discussed in Sec. 3; Sec. 4 details how the simulation is corrected in order to improve the modelling of the signal and background distributions in data and the efficiency determination; the resonant mass fits and related cross-checks are outlined in Sec. 5; Sec. 6 summarises the fit procedure and the systematic uncertainties associated with the measurements are described in Sec. 7; the results are presented in Sec. 8; and Sec. 9 presents the conclusions of this paper.

2 Detector and data sets

The LHCb detector [30, 31] is a single-arm forward spectrometer covering the pseudorapidity range $2 < \eta < 5$, designed for the study of particles containing b or

c quarks. The detector includes a high-precision tracking system consisting of a silicon-strip vertex detector surrounding the pp interaction region, a large-area silicon-strip detector located upstream of a dipole magnet with a bending power of about 4 Tm, and three stations of silicon-strip detectors and straw drift tubes placed downstream of the magnet. The tracking system provides a measurement of the momentum, p , of charged particles with a relative uncertainty that varies from 0.5% at low momentum to 1.0% at 200 GeV/ c . The minimum distance of a track to a primary vertex (PV), the impact parameter (IP), is measured with a resolution of $(15 + 29/p_T) \mu\text{m}$, where p_T is the component of the momentum transverse to the beam, in GeV/ c . Different types of charged hadrons are distinguished using information from two ring-imaging Cherenkov detectors. Photons, electrons and hadrons are identified by a calorimeter system consisting of scintillating-pad and preshower detectors, an electromagnetic (ECAL) and a hadronic (HCAL) calorimeter. Muons are identified by a system composed of alternating layers of iron and multiwire proportional chambers. The trigger system consists of a hardware stage, based on information from the calorimeter and muon systems, followed by a software stage, which applies a full event reconstruction. The hardware muon trigger selects events containing at least one muon with significant p_T (with thresholds ranging from ~ 1.5 to ~ 1.8 GeV/ c , depending on the data-taking period). The hardware electron trigger requires the presence of a cluster in the ECAL with significant transverse energy, E_T , (from ~ 2.5 to ~ 3.0 GeV, depending on the data-taking period). The software trigger requires a two-, three- or four-track secondary vertex, with a significant displacement from any primary pp interaction vertex. At least one charged particle must have significant p_T and be inconsistent with originating from any PV. A multivariate algorithm [32] is used for the identification of secondary vertices consistent with the decay of a b hadron.

The analysis is performed using a data sample corresponding to 3 fb^{-1} of pp collision data collected with the LHCb detector at a centre-of-mass energy of 7 and 8 TeV (Run 1) and 1.7 fb^{-1} at a centre-of-mass energy of 13 TeV collected during 2016 (Run 2).

Samples of simulated $\Lambda_b^0 \rightarrow pK^-\mu^+\mu^-$, $\Lambda_b^0 \rightarrow pK^-e^+e^-$, $\Lambda_b^0 \rightarrow pK^-J/\psi(\rightarrow \mu^+\mu^-)$ and $\Lambda_b^0 \rightarrow pK^-J/\psi(\rightarrow e^+e^-)$ decays, generated according to the available phase space in the decays, are used to optimise the selection, determine the efficiency of triggers, reconstruction and signal event selection, as well as to model the shapes used in the fits to extract the signal yields. The simulation is corrected to match the distributions observed in data using the $\Lambda_b^0 \rightarrow pK^-J/\psi$ control modes, as detailed in Sec. 4. In addition, specific simulated samples are exploited to estimate the contribution from various background sources. The pp collisions are generated using PYTHIA [33] with a specific LHCb configuration [34]. Decays of hadronic particles are described by EVTGEN [35], in which final-state radiation (FSR) is generated using PHOTOS [36], which is observed to agree with a full QED calculation at the level of $\sim 1\%$ for the R_K and R_{K^*0} observables [5]. The interactions of the generated particles with the detector, and its response, are implemented using the GEANT4 toolkit [37] as described in Ref. [38].

3 Selection and backgrounds

The Λ_b^0 candidates are formed from a pair of well reconstructed oppositely charged particles identified as muons or electrons, combined with a pair of oppositely charged particles, which are identified as a proton and a kaon. The pK^- invariant mass is required to be

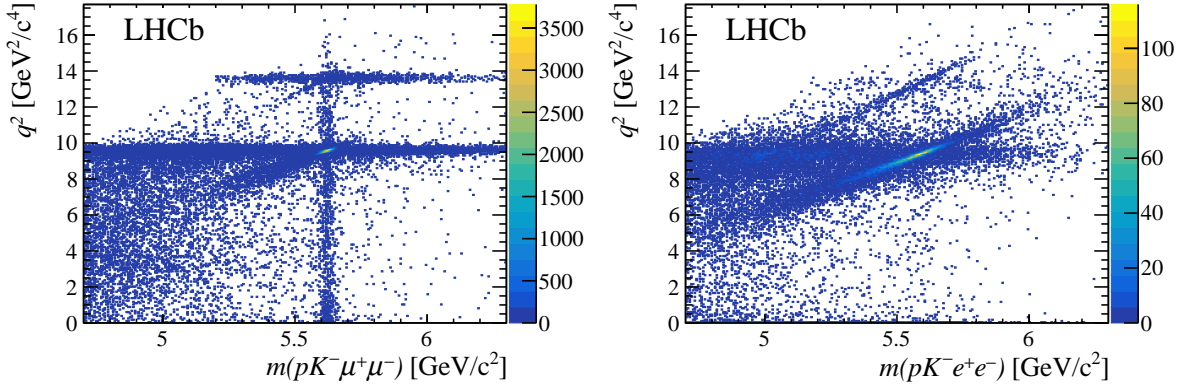


Figure 1: Distributions of dilepton invariant mass squared, q^2 , for Λ_b^0 candidates as a function of $pK^- \ell^+ \ell^-$ invariant mass, in data, for (left) $\ell = \mu$ and (right) $\ell = e$. The complete selection is applied to both distributions, except for q^2 and m_{corr} requirements, defined in Sec. 3.

smaller than $2600 \text{ MeV}/c^2$. Each particle is required to have a large momentum and p_T , and to not originate from any PV. In particular, for muon and electron candidates the p_T is required to be greater than $800 \text{ MeV}/c$ and $500 \text{ MeV}/c$, respectively. Kaon candidates must have a p_T larger than $250 \text{ MeV}/c^2$ and the proton p_T is required to be larger than $400 \text{ MeV}/c$ in Run 1, and $1000 \text{ MeV}/c$ in Run 2. All the particles must originate from a good-quality common vertex, which is displaced significantly from all reconstructed PVs in the event. When more than one PV is reconstructed, that with the smallest χ_{IP}^2 is selected (and referred to as the associated PV), where χ_{IP}^2 is the difference in χ^2 of a given PV reconstructed with and without tracks associated to the considered Λ_b^0 candidate. The momentum direction of the Λ_b^0 is required to be consistent with its direction of flight.

When interacting with the material of the detector, electrons radiate bremsstrahlung photons. If the photons are emitted upstream of the magnet, the photon and the electron deposit their energy in different ECAL cells, and the electron momentum measured by the tracking system is underestimated. A dedicated procedure, consisting in a search for neutral energy deposits in the ECAL compatible with being emitted by the electron, is applied to correct for this effect. The limitations of the recovery technique degrade the resolution of the reconstructed invariant masses of both the dielectron pair and the Λ_b^0 candidate [11].

The distribution of q^2 as a function of the four-body invariant mass for Λ_b^0 candidates is shown in Fig. 1 for both muon and electron final states. In each plot, the contributions due to the J/ψ and $\psi(2S)$ resonances are visible. Despite the recovery of bremsstrahlung photons, the e^+e^- invariant-mass distribution has a long radiative tail towards low values. Due to the correlation in the measurement of the q^2 and the $pK^- \ell^+ \ell^-$ invariant mass, the $\Lambda_b^0 \rightarrow pK^- J/\psi$ and $\Lambda_b^0 \rightarrow pK^- \psi(2S)$ contributions are visible as diagonal bands. Signal $\Lambda_b^0 \rightarrow pK^- \ell^+ \ell^-$ candidates form a vertical band, which is less prominent for the electron mode due to worse mass resolution and lower yield. The effect of the resolution motivates the choice of invariant-mass ranges considered for the analysis, which is presented in Table 1. The Λ_b^0 invariant-mass resolution and the signal and background contributions depend on the way in which the event was selected by the hardware trigger. The data sample of decay modes involving e^+e^- pairs is therefore divided into two mutually exclusive categories: candidates triggered by activity in the event which is not associated with any

Table 1: Resonant and nonresonant mode q^2 and $m(pK^-\ell^+\ell^-)$ ranges. The variables $m(pK^-\ell^+\ell^-)$ and $m_{J/\psi}(pK^-\ell^+\ell^-)$, corresponding to the four-body invariant mass and the four-body invariant mass computed with the J/ψ mass constraint on the dilepton system, are used for nonresonant and resonant Λ_b^0 decays, respectively.

Decay mode	q^2 [GeV ² /c ⁴]	$m_{(J/\psi)}(pK^-\ell^+\ell^-)$ [GeV/c ²]
nonresonant e^+e^-	0.1 – 6.0	4.80 – 6.32
resonant e^+e^-	6.0 – 11.0	5.30 – 6.20
nonresonant $\mu^+\mu^-$	0.1 – 6.0	5.10 – 6.10
resonant $\mu^+\mu^-$	8.41 – 10.24	5.30 – 5.95

of the signal decay particles (LOI), and candidates for which at least one of the electrons from the Λ_b^0 decay satisfies the hardware electron trigger and that are not selected by the previous requirement (LOE). For the decay modes involving a pair of muons, at least one of the two leptons must satisfy the requirements of the hardware muon trigger.

An important source of background arises from the misidentification of one or both of the final-state hadrons, denoted as hadron misidentification, which is common to both the resonant and nonresonant decays. All eight possible combinations of hadrons that can be misidentified as signal, namely K^+K^- , π^+K^- , $p\pi^-$, $p\bar{p}$, $K^+\bar{p}$, $K^+\pi^-$, $\pi^+\bar{p}$ and $\pi^+\pi^-$, are investigated using $\Lambda_b^0 \rightarrow pK^-J/\psi(\rightarrow \mu^+\mu^-)$ candidates in data. Contributions from misidentification of a single hadron are found to be dominant, namely $\bar{B}^0 \rightarrow \bar{K}^{*0}J/\psi(\rightarrow \ell^+\ell^-)$ with $\bar{K}^{*0} \rightarrow K^-\pi^+$, and $B_s^0 \rightarrow K^+K^-J/\psi(\rightarrow \ell^+\ell^-)$ decays, where a pion or a kaon is misidentified as a proton. A veto is applied to candidates with $m(K^+K^-)$ in a ± 12 MeV/c² mass window around the known ϕ mass in order to suppress the narrow ϕ contribution in misidentified $B_s^0 \rightarrow K^+K^-J/\psi(\rightarrow \ell^+\ell^-)$ and $B_s^0 \rightarrow K^+K^-\ell^+\ell^-$ decays. Finally, a double misidentification of the K and p hadrons, referred to as pK -swap, can occur. The particle identification (PID) requirements are optimised to suppress these backgrounds. Residual background contributions passing the candidate selection, namely $\bar{B}^0 \rightarrow \bar{K}^{*0}J/\psi(\rightarrow \ell^+\ell^-)$, $B_s^0 \rightarrow K^+K^-J/\psi(\rightarrow \ell^+\ell^-)$ and pK -swap, are included in the invariant-mass fits to the data described in Sec. 5.

For both the electron and muon resonant modes, a kinematic fit that constrains the dilepton invariant mass to the known mass of the J/ψ meson is used to compute the four-body invariant mass, $m_{J/\psi}(pK^-\ell^+\ell^-)$. A requirement on the four-body invariant mass $m_{J/\psi}(pK^-\ell^+\ell^-)$ for the resonant and $m(pK^-\mu^+\mu^-)$ for the nonresonant mode to be larger than 5100 MeV/c² excludes backgrounds due to partially reconstructed decays, of the type $\Lambda_b^0 \rightarrow pK^-\ell^+\ell^-X$, where one or more of the products of the Λ_b^0 decay, denoted X , are not reconstructed. These components can not be fully suppressed in the nonresonant electron mode and are taken into account in the fit. For the decay modes involving electrons, where a wider invariant-mass range is used, cascade backgrounds arising mainly from $\Lambda_b^0 \rightarrow \Lambda_c^+(\rightarrow pK^-\ell^+\bar{\nu}_\ell X)\ell^-\nu_\ell Y$, where potential additional particles X, Y are not reconstructed, are suppressed by a dedicated veto requiring $m(pK^-\ell^+) > 2320$ MeV/c². This requirement also allows the contamination from the hadronic decay $\Lambda_c^+ \rightarrow pK^-\pi^+$ to be removed. Additional vetoes are applied to suppress backgrounds from D^0 mesons and $\Lambda_b^0 \rightarrow pK^-J/\psi(\rightarrow \mu^+\mu^-)$ decays, where the identification of a muon and a kaon are swapped. Events in which the decay products of a $B^- \rightarrow K^-\ell^+\ell^-$ decay are combined with a random proton are suppressed by requiring $m(K^-\ell^+\ell^-) < 5200$ MeV/c². A two-

dimensional requirement based on the invariant mass of signal candidates calculated using the corrected dielectron momentum (m_{corr}) and the significance of the measured distance between the PV and the decay vertex is applied to reduce the partially reconstructed backgrounds. Following the procedure of Ref. [11], m_{corr} is computed by correcting the momentum of the dielectron pair by the ratio of the pK^- and the dielectron momentum components transverse to the Λ_b^0 direction of flight.

After all the selection procedures described above, the dominant remaining background is that originating from the combination of random tracks in the detector. This source is referred to as combinatorial background, and its properties vary between different q^2 regions. The separation between the signal and the combinatorial background is achieved using a Boosted Decision Tree (BDT) algorithm [39], which exploits the gradient boosting technique [40]. The classifier is constructed using variables such as transverse momenta, the quality of the vertex fit, the impact parameter χ^2 of the final-state particles, the angle between the direction of flight and the momentum of the Λ_b^0 candidate, and the minimum p_T of the hadron pair and of the lepton pair. For each run period, a single BDT classifier is trained for the resonant and nonresonant decays, where final states involving muons and electrons are treated separately. The classifiers are trained using simulated $\Lambda_b^0 \rightarrow pK^- \ell^+ \ell^-$ decays, which are corrected for known differences between data and simulation (see Sec. 4), to represent the signal, and candidates in data with $pK^- \ell^+ \ell^-$ invariant mass larger than $5825 \text{ MeV}/c^2$ are used to represent the background samples. To avoid potential biases and to fully exploit the size of the data sample for the training procedure, a k -folding technique [41] is adopted, with $k = 10$. For each decay mode and run period, the cut applied on the classifier is optimised using a figure of merit defined as $N_S/\sqrt{N_S + N_B}$, where N_S is the expected signal yield and N_B is the expected background yield, which is estimated by fitting the invariant mass sidebands in data. The BDT selection suppresses the combinatorial background by approximately 97% and retains 85% of the signal. The efficiency of each classifier is independent of $m(pK^- \ell^+ \ell^-)$ in the regions used to measure the signal yields. Once all the selection requirements are applied, less than 2.5% of the events contain multiple candidates. In these cases, one candidate per event is selected randomly and retained for further analysis. The effect of the multiple candidate removal cancels in the ratios measured in this analysis.

4 Corrections to the simulation and efficiencies

In order to optimise the selection criteria, model the invariant-mass shapes and accurately evaluate the efficiencies, a set of corrections to the simulation is determined from unbiased control samples selected from the data. These corrections are applied to the simulated samples of the nonresonant and resonant modes. The first correction accounts for the incorrect description of the hadronic structure of $\Lambda_b^0 \rightarrow pK^- \ell^+ \ell^-$ and $\Lambda_b^0 \rightarrow pK^- J/\psi(\rightarrow \ell^+ \ell^-)$ decays. The simulation of these decays for both the resonant and nonresonant modes relies on a simple phase-space model, while it is known from Ref. [26] that several resonances populate the pK^- invariant mass distribution of $\Lambda_b^0 \rightarrow pK^- J/\psi(\rightarrow \mu^+ \mu^-)$ decays. Corrections based on an amplitude analysis performed in Ref. [26] are applied to simulated $\Lambda_b^0 \rightarrow pK^- J/\psi(\rightarrow \ell^+ \ell^-)$ and $\Lambda_b^0 \rightarrow pK^- \ell^+ \ell^-$ decays. Differences between data and simulation in the kinematics of Λ_b^0 decays are accounted for using two-dimensional corrections derived from data as a function of the p_T and pseudorapidity, η , of the Λ_b^0

Table 2: Efficiency ratios between the nonresonant and resonant modes, $\epsilon(\Lambda_b^0 \rightarrow pK^- \ell^+ \ell^-) / \epsilon(\Lambda_b^0 \rightarrow pK^- J/\psi(\rightarrow \ell^+ \ell^-))$, for the muon final state and electron final state in the two trigger categories and data-taking periods. The uncertainties are statistical only.

Channel	Run 1	Run 2
$\mu^+ \mu^-$	0.756 ± 0.010	0.796 ± 0.013
$e^+ e^-$ (LOI)	0.862 ± 0.017	0.859 ± 0.018
$e^+ e^-$ (LOE)	0.630 ± 0.013	0.631 ± 0.013

candidate. The simulation samples used in this analysis were generated with a value of the Λ_b^0 lifetime that did not account for newer and more accurate measurements [27]; a correction is applied to account for this small discrepancy.

A correction is also applied to account for differences between the PID response in data and simulation [42]. Several high-purity control samples are employed to evaluate the PID efficiencies in data using a tag-and-probe technique. For kaons and protons, samples of $D^{*+} \rightarrow D^0(\rightarrow K^- \pi^+) \pi^+$ and $\Lambda_b^0 \rightarrow \Lambda_c^+(\rightarrow pK^- \pi^+) \pi^-$ are used, respectively. Finally, the electron and muon identification efficiencies are obtained from $B^+ \rightarrow K^+ J/\psi(\rightarrow \ell^+ \ell^-)$ decays. For each type of particle, the corrections are evaluated as a function of track momentum and pseudorapidity. Corrections obtained from the distributions of the number of reconstructed tracks per event, compared between data and simulation, are used to account for the mismodelling in the average event multiplicity. The simulated response of both the hardware and software triggers is corrected for using a tag-and-probe technique on $\Lambda_b^0 \rightarrow pK^- J/\psi(\rightarrow \ell^+ \ell^-)$ candidates. The corrections for the response of the leptonic hardware triggers are parametrised as a function of the cluster E_T or track p_T . For the software trigger, the corrections are determined as a function of the minimum p_T of the Λ_b^0 decay products. Once all the corrections are applied to the simulation, very good agreement between data and simulation is found.

The efficiency for selecting each decay mode, which enters the computation of R_{pK}^{-1} , is defined as the product of the geometrical acceptance of the detector, and the efficiency of the complete reconstruction of all tracks, the trigger requirements and the full set of kinematic, PID and background rejection requirements. It takes into account migration between bins of q^2 due to resolution, FSR and bremsstrahlung emission. The efficiency ratios between the nonresonant and the resonant modes, which directly enter the R_{pK}^{-1} computation, are reported in Table 2.

5 Mass fit to the resonant modes

The resonant yields are determined from unbinned extended maximum-likelihood fits to the $m_{J/\psi}(pK^- \ell^+ \ell^-)$ distributions separately for various data-taking periods. For the $\Lambda_b^0 \rightarrow pK^- J/\psi(\rightarrow \mu^+ \mu^-)$ decay, the probability density function (PDF) for the signal is modelled by a bifurcated Crystal Ball (CB) function [43], which consists of a Gaussian core with asymmetric power-law tails. The parameters describing the tails are fixed from a fit to simulated signal decays. However, in order to account for possible remaining discrepancies with data, the mean and the width of the function are allowed to vary freely in the fit. The invariant-mass distribution of $\Lambda_b^0 \rightarrow pK^- J/\psi(\rightarrow e^+ e^-)$ decays is fitted independently for the two trigger categories, since different relative amounts of

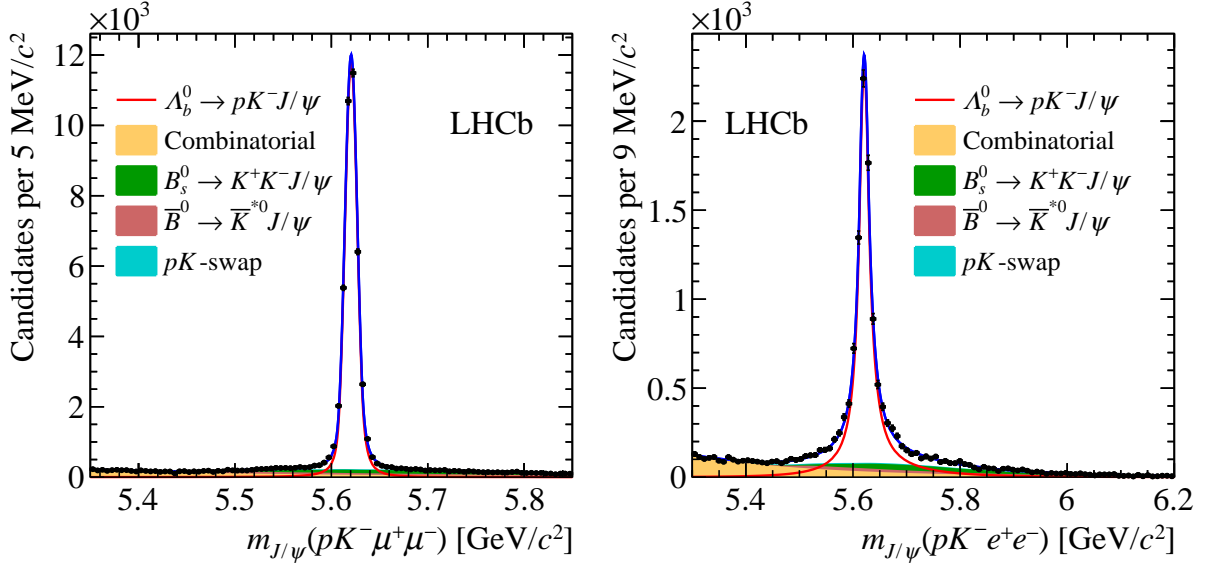


Figure 2: Invariant-mass distribution, with the J/ψ mass constraint applied, of $\Lambda_b^0 \rightarrow pK^- J/\psi(\rightarrow \mu^+ \mu^-)$ (left) and $\Lambda_b^0 \rightarrow pK^- J/\psi(\rightarrow e^+ e^-)$ (right) candidates, summed over trigger and data-taking categories. The black points represent the data, while the solid blue curve shows the result of the fit. The signal component is represented by the red curve and the shaded shapes are the background components, as detailed in the legend.

background and signal are expected. In each category, a sum of two bifurcated CB functions is used to model the signal shape. Similarly to the approach adopted for the muon mode, the parameters describing the tails of the signal distributions are fixed from the fits to simulated signal. In addition, the difference of the means of the two functions, and the ratio of their widths are also fixed according to the simulation. The mean and the width of one CB function are allowed to vary. For both electron and muon modes, the combinatorial background is parametrised using an exponential function with a free slope. Contributions from misidentified $\bar{B}^0 \rightarrow \bar{K}^{*0} J/\psi(\rightarrow \ell^+ \ell^-)$ and $B_s^0 \rightarrow K^+ K^- J/\psi(\rightarrow \ell^+ \ell^-)$ decays and from pK -swap are included in the fits. They are described separately for the electron and muon modes, using kernel estimation techniques [44] applied to simulated events. The signal yield, as well as the yields of the combinatorial background and \bar{B}^0 components are free parameters of the fit. The yields of the pK -swap component are related to the signal yields by a factor estimated from the $\Lambda_b^0 \rightarrow pK^- J/\psi(\rightarrow \mu^+ \mu^-)$ fit and propagated to the electron mode. The ratios between the B_s^0 and \bar{B}^0 background components are fixed from dedicated fits to the data. The results of the invariant-mass fits, including data from all the trigger categories and data-taking periods, are shown in Fig. 2. A total of $40\,980 \pm 220$ and $10\,180 \pm 140$ decays are found for the muon and electron resonant modes, respectively.

An important cross-check of the efficiencies is done using the ratio of branching fractions of the muon and electron resonant channels

$$r_{J/\psi}^{-1} = \frac{N(\Lambda_b^0 \rightarrow pK^- J/\psi(\rightarrow e^+ e^-))}{N(\Lambda_b^0 \rightarrow pK^- J/\psi(\rightarrow \mu^+ \mu^-))} \times \frac{\epsilon(\Lambda_b^0 \rightarrow pK^- J/\psi(\rightarrow \mu^+ \mu^-))}{\epsilon(\Lambda_b^0 \rightarrow pK^- J/\psi(\rightarrow e^+ e^-))}, \quad (3)$$

which is expected to be equal to unity [27]. The measurement of $r_{J/\psi}^{-1}$ is a very stringent test since, contrary to the double ratio R_{pK}^{-1} , it does not benefit from the cancellation

of the experimental systematic uncertainties related to the differences in the treatment of muons and electrons. This quantity is found to be $r_{J/\psi}^{-1} = 0.96 \pm 0.05$, where the uncertainty combines both statistical and systematic effects. Similar sources of systematic uncertainties to the R_{pK}^{-1} measurement are considered (see Sec. 7). The value of $r_{J/\psi}^{-1}$ is compatible with unity within one standard deviation. The $r_{J/\psi}^{-1}$ ratio is examined as a function of a number of kinematic variables such as p_T and η of the Λ_b^0 baryon, $m(pK^-)$, the final-state particle p_T and the BDT classifier response. In all of the cases the result is compatible with a flat distribution. The validity of the analysis is tested by measuring the double ratio $R_{\psi(2S)}^{-1}$, defined in Eq. 2 where $\Lambda_b^0 \rightarrow pK^- \psi(2S) (\rightarrow \ell^+ \ell^-)$ decays are used in place of $\Lambda_b^0 \rightarrow pK^- \ell^+ \ell^-$. The $R_{\psi(2S)}^{-1}$ ratio is found to be compatible with unity within statistical uncertainties. However its statistical power is limited by the reduced phase-space available in this high- q^2 region.

6 Mass fit to the nonresonant modes

An unbinned maximum-likelihood fit to the invariant-mass distribution of nonresonant $pK^- \ell^+ \ell^-$ -candidates is performed simultaneously to the muon and electron modes in all the trigger and data-taking categories to extract the observables of interest. For each category i , the nonresonant yields are expressed in terms of the parameters of interest

$$N^i(\Lambda_b^0 \rightarrow pK^- \mu^+ \mu^-) = r_{\mathcal{B}} \times \frac{N^i(\Lambda_b^0 \rightarrow pK^- J/\psi (\rightarrow \mu^+ \mu^-))}{\mathcal{B}(J/\psi \rightarrow \ell^+ \ell^-)} \times \frac{\epsilon^i(\Lambda_b^0 \rightarrow pK^- \mu^+ \mu^-)}{\epsilon^i(\Lambda_b^0 \rightarrow pK^- J/\psi (\rightarrow \mu^+ \mu^-))}, \quad (4)$$

$$N^i(\Lambda_b^0 \rightarrow pK^- e^+ e^-) = R_{pK}^{-1} \times r_{\mathcal{B}} \times \frac{N^i(\Lambda_b^0 \rightarrow pK^- J/\psi (\rightarrow e^+ e^-))}{\mathcal{B}(J/\psi \rightarrow \ell^+ \ell^-)} \times \frac{\epsilon^i(\Lambda_b^0 \rightarrow pK^- e^+ e^-)}{\epsilon^i(\Lambda_b^0 \rightarrow pK^- J/\psi (\rightarrow e^+ e^-))}, \quad (5)$$

where N^i is the event yield for the given decay in category i , ϵ^i the reconstruction and selection efficiency in that category, and $r_{\mathcal{B}} \equiv \mathcal{B}(\Lambda_b^0 \rightarrow pK^- \mu^+ \mu^-) / \mathcal{B}(\Lambda_b^0 \rightarrow pK^- J/\psi)$ and R_{pK}^{-1} the observables. The yields of the resonant modes are obtained from the fits described in Sec. 5, and the ratios of efficiencies are extracted from calibrated simulated samples and reported in Table 2. The branching fraction of the leptonic decay of the J/ψ meson is assumed to be flavour universal [27]. For the nonresonant decays, no constraint can be imposed on the dilepton mass, and the $pK^- \ell^+ \ell^-$ invariant-mass resolution is therefore worse than in the resonant case. For the electron final state, it is significantly degraded compared to the resolution in the muon case. The fit range is extended accordingly as summarised in Table 1. As a consequence, more sources of background have to be taken into account in the electron mode. Both models are described separately in the following.

The $\Lambda_b^0 \rightarrow pK^- \mu^+ \mu^-$ signal contribution is modelled by a bifurcated CB function, with the tail parameters determined on simulated data. The mean and the width of the distribution are allowed to vary freely in the fit to data. The combinatorial background is described with an exponential PDF with free slope and yield. The contamination from

misreconstructed $\bar{B}^0 \rightarrow \bar{K}^{*0} \mu^+ \mu^-$ and $B_s^0 \rightarrow K^+ K^- \mu^+ \mu^-$ decays is modelled by kernel estimation techniques applied to simulation. The $\bar{B}^0 \rightarrow \bar{K}^{*0} \mu^+ \mu^-$ yield is constrained to the value expected from simulation and the measured branching fraction [27] and the relative contributions of $B_s^0 \rightarrow K^+ K^- \mu^+ \mu^-$ and $\bar{B}^0 \rightarrow \bar{K}^{*0} \mu^+ \mu^-$ decays are constrained to the ratio observed in the corresponding J/ψ modes. An associated systematic uncertainty is added for this choice. The contamination from pK -swap candidates is found to be negligible for the nonresonant modes, so no component is added to the fit to account for it.

The $\Lambda_b^0 \rightarrow pK^- e^+ e^-$ signal component is modelled by the sum of three distributions, describing candidates where the electron candidates have no associated bremsstrahlung photon, have only one, or more than one. In the first case, the distribution presents a tail at low mass, due to unrecovered losses, but no tail at high mass and is thus modelled by a single CB function. The other two present a smaller tail at low mass, since energy losses are partially recovered, but also a tail at high mass, due to wrongly associated photons, and are modelled by the sum of two bifurcated CB functions. The tail parameters of these functions are fixed from fits to simulated signal. The proportions between the three cases are also obtained from simulation. Combinatorial and misidentified backgrounds are modelled in an analogous way to the muon mode. However, partially reconstructed backgrounds of the type $\Lambda_b^0 \rightarrow pK^- e^+ e^- \pi^0$, where the π^0 is not reconstructed, cannot be efficiently excluded in this case, due to the worse resolution and the wider invariant-mass range used in the electron mode fit. This background is modelled using kernel estimation techniques applied to simulated $\Lambda_b^0 \rightarrow pK^{*-} e^+ e^-$ events, with $K^{*-} \rightarrow K^- \pi^0$, since this is the most realistic physical background contributing to this type of decay. The yield of this component is free to vary in the fit to data. Finally, $\Lambda_b^0 \rightarrow pK^- J/\psi (\rightarrow e^+ e^-)$ decays that lose energy by bremsstrahlung can also pollute the nonresonant $\Lambda_b^0 \rightarrow pK^- e^+ e^-$ candidates in the low invariant-mass region. This contribution is modelled using simulated events. Its yield is constrained in the fit, based on the measured $\Lambda_b^0 \rightarrow pK^- J/\psi (\rightarrow e^+ e^-)$ yield and the probability of such q^2 migration determined using simulated samples. The stability of the fit is evaluated with a large number of pseudoexperiments before proceeding to the final fit to data. The moments of the pull distributions of the R_{pK}^{-1} and r_B parameters are examined and the estimators are observed to be unbiased.

The results of the fit to data, where candidates are accumulated over all the trigger and data-taking categories, are shown in Fig. 3. In total, 444 ± 23 $\Lambda_b^0 \rightarrow pK^- \mu^+ \mu^-$ and 122 ± 17 $\Lambda_b^0 \rightarrow pK^- e^+ e^-$ decays are observed.

7 Systematic uncertainties

Systematic uncertainties arise from the computation of efficiencies, the limited precision on the measurement of the resonant mode yields and the fit model. Uncertainties that are uncorrelated between different trigger and data-taking categories are taken into account as Gaussian constraints on the input parameters to the fit, so that they are accounted for by the uncertainty returned by the fit. Correlated uncertainties are accounted for by smearing the likelihood profile for the given parameter of interest.

The main systematic uncertainties on the ratio of branching fractions, r_B , come from the procedure used to correct the simulation for the imperfect description of the $\Lambda_b^0 \rightarrow pK^- \mu^+ \mu^-$ decay model and the detector response. The first one is evaluated

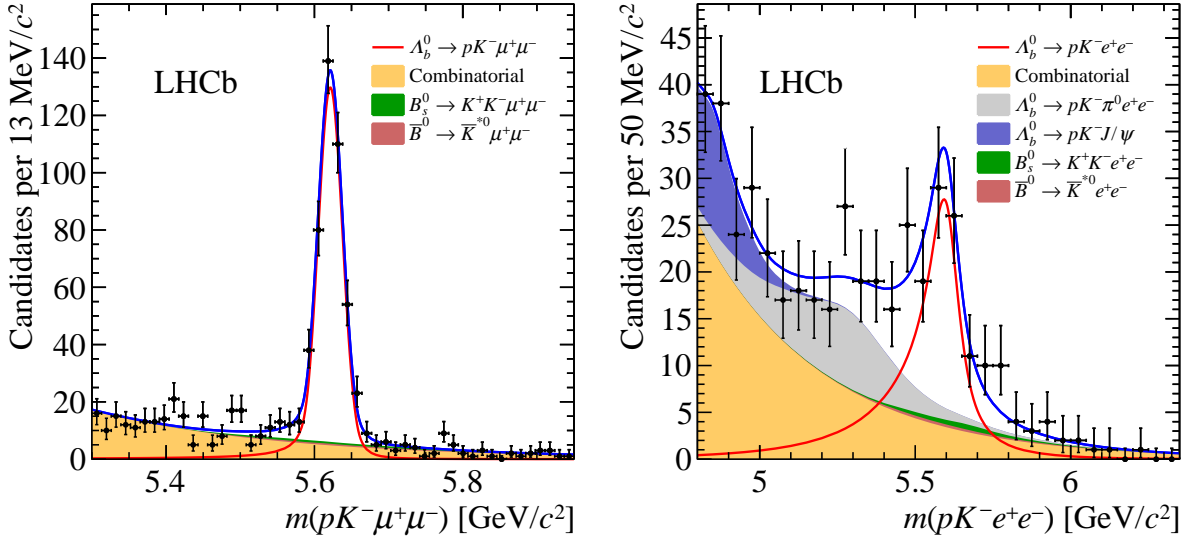


Figure 3: Invariant-mass distribution of (left) $\Lambda_b^0 \rightarrow pK^-\mu^+\mu^-$ and (right) $\Lambda_b^0 \rightarrow pK^-e^+e^-$ candidates summed over trigger and data-taking categories. The black points represent the data, while the solid blue curve shows the total PDF. The signal component is represented by the red curve and the combinatorial, $\bar{B}^0 \rightarrow \bar{K}^{*0}\ell^+\ell^-$ and $B_s^0 \rightarrow K^+K^-\ell^+\ell^-$ components by yellow, brown and green filled histograms. In the electron model, the grey and blue filled histograms represent the partially reconstructed and $\Lambda_b^0 \rightarrow pK^-J/\psi(\rightarrow e^+e^-)$ backgrounds.

by reweighting the distributions of $m(pK^-)$, q^2 and the helicity angles, $\cos\theta_K$ and $\cos\theta_\ell$, in the $\Lambda_b^0 \rightarrow pK^-\mu^+\mu^-$ simulation to match those observed in data, instead of the amplitude model of the $\Lambda_b^0 \rightarrow pK^-J/\psi(\rightarrow \mu^+\mu^-)$ decay explained in Sec. 4. The distributions of $m(pK^-)$, q^2 and the helicity angles are corrected separately and the systematic uncertainties are added in quadrature. Since this is a decay-model effect, it is correlated between different data-taking periods and trigger categories. For the other corrections applied to simulation, the systematic uncertainty is evaluated using an alternative parameterisation of the correction, as well as different control samples to determine the corrections. After all the corrections are applied, a small disagreement between data and simulation is seen in the proton momentum and impact parameter distributions. An associated systematic effect is estimated by correcting these distributions to match those observed in data.

A bootstrapping technique is used to evaluate the effect of the limited size of the simulated samples used to calculate the corrections. The systematic uncertainties accounting for data and simulation differences are computed separately for each data-taking period and trigger category and are thus uncorrelated. Systematic uncertainties associated with the fit model are estimated using pseudoexperiments and are fully correlated between data-taking periods. Different sets are generated with alternative $\bar{B}^0 \rightarrow \bar{K}^{*0}\mu^+\mu^-$ and $B_s^0 \rightarrow K^+K^-\mu^+\mu^-$ yields and different smearing parameters for the nonparametric shapes. Alternatively, possible contributions of partially reconstructed backgrounds with a missing π^0 meson or from cascade decays of the type $H_b \rightarrow H_c(\rightarrow K^-\mu^+\nu_\mu X)\mu^-\bar{\nu}_\mu Y$, where H denotes hadrons and the potential additional particles X and Y are not always reconstructed, are also included in the generated sets. These generated samples are fit with the default model and the difference obtained on r_B is assigned as a systematic uncertainty. Also,

Table 3: Systematic uncertainties in percent associated to the ratio of branching fractions, $r_{\mathcal{B}}$, for the different data taking periods. For uncertainties that are correlated between data taking periods, a single value is given.

Source	Run 1	Run 2	Correlated
Decay model	–	–	3.6
Other corrections	2.5	3.3	–
Normalisation mode	0.9	1.4	–
Fit model	–	–	1.4
Total uncorrelated	2.6	3.6	–
Total correlated	–	–	3.9

the uncertainties on the $\Lambda_b^0 \rightarrow pK^- J/\psi(\rightarrow \mu^+ \mu^-)$ yields are propagated to the systematic uncertainties of $r_{\mathcal{B}}$. The systematic uncertainties associated to the measurement of the ratio of branching fractions are summarised in Table 3.

The sources of systematic uncertainties described for $r_{\mathcal{B}}$ also affect the double ratio R_{pK}^{-1} , but their sizes are expected to be smaller due to cancellations in the ratios. However, some additional sources have to be considered, which are specific to the electron mode and are related to the worse resolution of the nonresonant decay compared to the resonant one. Signal decays that migrate in and out of the $0.1 < q^2 < 6 \text{ GeV}^2/c^4$ window due to resolution effects are taken into account in the efficiency determination. However, potential mismodelling of the q^2 resolution or its distribution in the simulation can introduce a systematic bias. The first effect is estimated by smearing the q^2 distribution of $\Lambda_b^0 \rightarrow pK^- e^+ e^-$ decays in simulation according to the differences observed between $\Lambda_b^0 \rightarrow pK^- J/\psi(\rightarrow e^+ e^-)$ data and simulated candidates. Similarly, the effect of an alternative q^2 model is estimated by weighting simulated $\Lambda_b^0 \rightarrow pK^- e^+ e^-$ events to match the q^2 distribution of $\bar{B}^0 \rightarrow \bar{K}^{*0} e^+ e^-$ decays generated with the model described in Ref. [45]. This uncertainty is taken to be fully correlated between trigger categories and data-taking periods. Potential disagreement between the resolution in simulation and data for the m_{corr} variable, which is only used in the selection of $\Lambda_b^0 \rightarrow pK^- e^+ e^-$ candidates, is studied with $\Lambda_b^0 \rightarrow pK^- J/\psi(\rightarrow e^+ e^-)$ candidates. A correction is obtained by comparing the distribution of this quantity for $\Lambda_b^0 \rightarrow pK^- J/\psi(\rightarrow e^+ e^-)$ candidates in data and simulation and is applied to the $\Lambda_b^0 \rightarrow pK^- e^+ e^-$ simulation. No significant variation on the efficiency is found but a systematic contribution corresponding to one half of its uncertainty is conservatively assigned and considered to be fully correlated between trigger categories and data-taking periods. Systematic uncertainties affecting the $\Lambda_b^0 \rightarrow pK^- e^+ e^-$ fit model are evaluated using pseudoexperiments. The scale factor of the signal width is varied by $\pm 5\%$, the kernel of the nonparametric models describing the $\bar{B}^0 \rightarrow \bar{K}^{*0} e^+ e^-$, $B_s^0 \rightarrow K^+ K^- e^+ e^-$, $\Lambda_b^0 \rightarrow pK^- e^+ e^- \pi^0$ and $\Lambda_b^0 \rightarrow pK^- J/\psi(\rightarrow e^+ e^-)$ backgrounds is varied and a component describing cascade $H_b \rightarrow H_c(\rightarrow K^- \ell^+ \nu_e X) \ell^- \bar{\nu}_e Y$ decays is added to the model. The largest effect comes from the limited knowledge of the $\Lambda_b^0 \rightarrow pK^- e^+ e^- \pi^0$ invariant-mass shape. It is alternatively obtained from simulated decays with an intermediate Δ resonance decaying to $p\pi^0$, decays with an intermediate $\Lambda(1810)$ resonance decaying to pK^{*-} , followed by $K^{*-} \rightarrow K^- \pi^0$, and from decays with no resonant structure. The latter approach gives the largest variation in the signal yield with respect to the default fit model, which is assigned as systematic uncertainty. Ignoring this

Table 4: Systematic uncertainties in percent associated to the measurement of R_{pK}^{-1} , for the different data taking periods and trigger categories. For uncertainties that are correlated between data taking periods and categories, a single value is given.

Source	Run 1 L0I	Run 1 L0E	Run 2 L0I	Run 2 L0E	Correlated
Decay model	–	–	–	–	1.9
Other corrections	3.4	3.6	3.6	3.2	–
m_{corr} cut efficiency	–	–	–	–	0.5
q^2 migration	–	–	–	–	2.0
Normalisation mode	3.7	3.7	3.5	2.7	–
Fit model	–	–	–	–	5.2
Total correlated	–	–	–	–	5.9
Total uncorrelated	5.0	5.2	5.0	4.2	–

background in the fit model is also considered, but provides a smaller difference in the signal yield. These uncertainties are treated as fully correlated between trigger categories and data-taking periods. The systematic uncertainties associated to the measurement of R_{pK}^{-1} are summarised in Table 4.

As a cross-check, the effect of all the corrections applied to the simulation is evaluated by removing them and estimating the change in the R_{pK}^{-1} value. A 8.5% effect is observed on the double ratio.

8 Results

The ratio of branching fractions $r_{\mathcal{B}} = \mathcal{B}(\Lambda_b^0 \rightarrow pK^- \mu^+ \mu^-) / \mathcal{B}(\Lambda_b^0 \rightarrow pK^- J/\psi (\rightarrow \mu^+ \mu^-))$ and the R_{pK}^{-1} observable in the range $0.1 < q^2 < 6 \text{ GeV}^2/c^4$ and $m(pK^-) < 2600 \text{ MeV}/c^2$ are obtained directly from the fit to data candidates. The result for the ratio of branching fractions is

$$\frac{\mathcal{B}(\Lambda_b^0 \rightarrow pK^- \mu^+ \mu^-)}{\mathcal{B}(\Lambda_b^0 \rightarrow pK^- J/\psi)} \Big|_{0.1 < q^2 < 6 \text{ GeV}^2/c^4} = (8.4 \pm 0.4 \pm 0.4) \times 10^{-4},$$

where the first uncertainty is statistical and the second systematic. The absolute branching fraction for the decay $\Lambda_b^0 \rightarrow pK^- \mu^+ \mu^-$ in the range $0.1 < q^2 < 6 \text{ GeV}^2/c^4$ and $m(pK^-) < 2600 \text{ MeV}/c^2$ is computed using the value of $\mathcal{B}(\Lambda_b^0 \rightarrow pK^- J/\psi)$ measured by LHCb [46]

$$\mathcal{B}(\Lambda_b^0 \rightarrow pK^- \mu^+ \mu^-) \Big|_{0.1 < q^2 < 6 \text{ GeV}^2/c^4} = (2.65 \pm 0.14 \pm 0.12 \pm 0.29_{-0.23}^{+0.38}) \times 10^{-7},$$

where the first uncertainty is statistical, the second is systematic and the third and fourth are due to the precision of the normalisation mode $\Lambda_b^0 \rightarrow pK^- J/\psi$, namely the knowledge of the $B^0 \rightarrow J/\psi K^{*0}$ branching fraction and the Λ_b^0 hadronisation fraction.

The result of the test of LU in $\Lambda_b^0 \rightarrow pK^- \ell^+ \ell^-$ decays, R_{pK}^{-1} , in the range $0.1 < q^2 < 6 \text{ GeV}^2/c^4$ and $m(pK^-) < 2600 \text{ MeV}/c^2$ is

$$R_{pK}^{-1} \Big|_{0.1 < q^2 < 6 \text{ GeV}^2/c^4} = 1.17_{-0.16}^{+0.18} \pm 0.07,$$

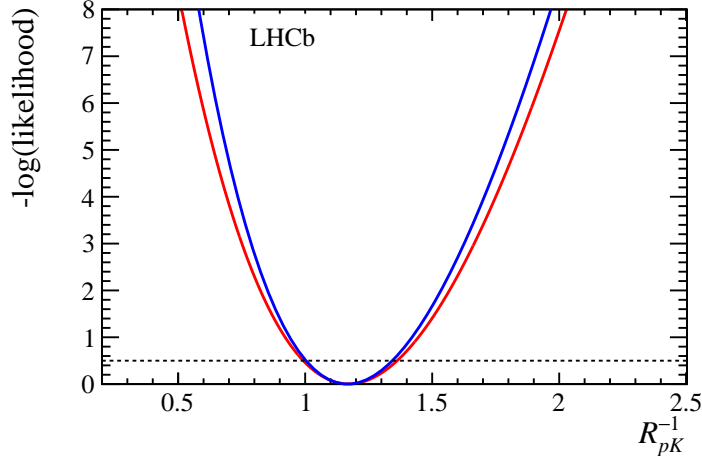


Figure 4: Logarithm of the profile likelihood of the R_{pK}^{-1} parameter in blue (red) including only statistical (total) uncertainty. The dashed line indicates the one standard deviation interval.

where the first uncertainty is statistical and the second systematic. The profile likelihood of the R_{pK}^{-1} parameter, including the smearing accounting for correlated systematic uncertainties, is shown in Fig. 4. The result is compatible with unity at the level of one standard deviation. For comparison with other LU tests, R_{pK} is computed from the R_{pK}^{-1} results by inverting the minimum and one standard deviation lower and upper bounds of the likelihood profile

$$R_{pK}|_{0.1 < q^2 < 6 \text{ GeV}^2/c^4} = 0.86_{-0.11}^{+0.14} \pm 0.05,$$

with a more asymmetric likelihood distribution in this case.

The first observation of the rare decay $\Lambda_b^0 \rightarrow pK^- e^+ e^-$ is also reported, with a significance greater than 7σ , accounting for systematic uncertainties. Combining the results obtained for $r_{\mathcal{B}}$ and R_{pK}^{-1} , and taking into account the correlations, the ratio of branching fractions for the dielectron final states is obtained

$$\frac{\mathcal{B}(\Lambda_b^0 \rightarrow pK^- e^+ e^-)}{\mathcal{B}(\Lambda_b^0 \rightarrow pK^- J/\psi)} \Big|_{0.1 < q^2 < 6 \text{ GeV}^2/c^4} = (9.8_{-1.3}^{+1.4} \pm 0.8) \times 10^{-4},$$

where the first uncertainty is statistical and the second systematic. Taking into account the measured value of $\mathcal{B}(\Lambda_b^0 \rightarrow pK^- J/\psi)$ [46], the branching fraction of the nonresonant electron mode is found to be

$$\mathcal{B}(\Lambda_b^0 \rightarrow pK^- e^+ e^-) \Big|_{0.1 < q^2 < 6 \text{ GeV}^2/c^4} = (3.1 \pm 0.4 \pm 0.2 \pm 0.3_{-0.3}^{+0.4}) \times 10^{-7},$$

where the first uncertainty is statistical, the second systematic and the third and fourth are due to the uncertainties on $\mathcal{B}(\Lambda_b^0 \rightarrow pK^- J/\psi)$.

9 Conclusions

A test of lepton universality is performed for the first time using rare b -baryon decays, namely $\Lambda_b^0 \rightarrow pK^- \ell^+ \ell^-$ with $\ell = e, \mu$. The measurement is performed in the

range $0.1 < q^2 < 6 \text{ GeV}^2/c^4$ and $m(pK^-) < 2600 \text{ MeV}/c^2$ and the result is found to be $R_{pK}^{-1} = 1.17_{-0.16}^{+0.18} \pm 0.07$, compatible with unity within one standard deviation. This result is also in agreement with the deviations observed in lepton-universality tests with B mesons [10, 11], denoted R_K and R_{K^*0} . More data is needed to confirm or exclude the presence of New Physics contributions in these decays. It should be noted that the current analysis is affected by different experimental uncertainties than those of lepton-universality tests performed with B mesons, such as the backgrounds that affect the extraction of the signal yields from data, or the control modes which are used to calibrate the simulation and measure the double ratio. Consequently, it provides an independent test of the SM.

The first measurement of the branching fraction of the rare muonic decay mode $\Lambda_b^0 \rightarrow pK^- \mu^+ \mu^-$ is also performed and its value is found to be $\mathcal{B}(\Lambda_b^0 \rightarrow pK^- \mu^+ \mu^-)|_{0.1 < q^2 < 6 \text{ GeV}^2/c^4} = (2.65 \pm 0.14 \pm 0.12 \pm 0.29_{-0.23}^{+0.38}) \times 10^{-7}$, where the uncertainty is dominated by the limited knowledge of the $\Lambda_b^0 \rightarrow pK^- J/\psi$ normalisation mode. This result is obtained in the range $m(pK^-) < 2600 \text{ MeV}/c^2$, which includes several resonant structures, and thus cannot be directly compared to the recent predictions computed for the exclusive decay $\Lambda_b^0 \rightarrow \Lambda(1520)\ell^+\ell^-$ [29].

Finally, the electron mode $\Lambda_b^0 \rightarrow pK^- e^+ e^-$ is observed for the first time with a significance larger than 7σ including systematic uncertainties, and its branching fraction is determined by combining the results of R_{pK}^{-1} and $\mathcal{B}(\Lambda_b^0 \rightarrow pK^- \mu^+ \mu^-)/\mathcal{B}(\Lambda_b^0 \rightarrow pK^- J/\psi)$, $\mathcal{B}(\Lambda_b^0 \rightarrow pK^- e^+ e^-)|_{0.1 < q^2 < 6 \text{ GeV}^2/c^4} = (3.1 \pm 0.4 \pm 0.2 \pm 0.3_{-0.3}^{+0.4}) \times 10^{-7}$. This is the first observation of a rare b -baryon decay with electrons in the final state and it opens the door to further tests of lepton universality in baryon decays.

Acknowledgements

We express our gratitude to our colleagues in the CERN accelerator departments for the excellent performance of the LHC. We thank the technical and administrative staff at the LHCb institutes. We acknowledge support from CERN and from the national agencies: CAPES, CNPq, FAPERJ and FINEP (Brazil); MOST and NSFC (China); CNRS/IN2P3 (France); BMBF, DFG and MPG (Germany); INFN (Italy); NWO (Netherlands); MNiSW and NCN (Poland); MEN/IFA (Romania); MSHE (Russia); MinECa (Spain); SNSF and SER (Switzerland); NASU (Ukraine); STFC (United Kingdom); DOE NP and NSF (USA). We acknowledge the computing resources that are provided by CERN, IN2P3 (France), KIT and DESY (Germany), INFN (Italy), SURF (Netherlands), PIC (Spain), GridPP (United Kingdom), RRCKI and Yandex LLC (Russia), CSCS (Switzerland), IFIN-HH (Romania), CBPF (Brazil), PL-GRID (Poland) and OSC (USA). We are indebted to the communities behind the multiple open-source software packages on which we depend. Individual groups or members have received support from AvH Foundation (Germany); EPLANET, Marie Skłodowska-Curie Actions and ERC (European Union); ANR, Labex P2IO and OCEVU, and Région Auvergne-Rhône-Alpes (France); Key Research Program of Frontier Sciences of CAS, CAS PIFI, and the Thousand Talents Program (China); RFBR, RSF and Yandex LLC (Russia); GVA, XuntaGal and GENCAT (Spain); the Royal Society and the Leverhulme Trust (United Kingdom).

References

- [1] LHCb collaboration, R. Aaij *et al.*, *Angular analysis of the $B^0 \rightarrow K^{*0} \mu^+ \mu^-$ decay using 3 fb^{-1} of integrated luminosity*, JHEP **02** (2016) 104, arXiv: 1512.04442.
- [2] Belle collaboration, S. Wehle *et al.*, *Lepton-flavor-dependent angular analysis of $B \rightarrow K^* \ell^+ \ell^-$* , Phys. Rev. Lett. **118** (2017) 111801, arXiv: 1612.05014.
- [3] ATLAS collaboration, M. Aaboud *et al.*, *Angular analysis of $B_d^0 \rightarrow K^* \mu^+ \mu^-$ decays in pp collisions at $\sqrt{s} = 8 \text{ TeV}$ with the ATLAS detector*, JHEP **10** (2018) 047, arXiv: 1805.04000.
- [4] CMS collaboration, A. M. Sirunyan *et al.*, *Measurement of angular parameters from the decay $B^0 \rightarrow K^{*0} \mu^+ \mu^-$ in proton-proton collisions at $\sqrt{s} = 8 \text{ TeV}$* , Phys. Lett. **B781** (2018) 517, arXiv: 1710.02846.
- [5] M. Bordone, G. Isidori, and A. Pattori, *On the Standard Model predictions for R_K and R_{K^*}* , Eur. Phys. J. **C76** (2016) 440, arXiv: 1605.07633.
- [6] BaBar collaboration, J. P. Lees *et al.*, *Measurement of branching fractions and rate asymmetries in the rare decays $B \rightarrow K^{(*)} \ell^+ \ell^-$* , Phys. Rev. **D86** (2012) 032012, arXiv: 1204.3933.
- [7] Belle collaboration, J.-T. Wei *et al.*, *Measurement of the differential branching fraction and forward-backward asymmetry for $B \rightarrow K^{(*)} \ell^+ \ell^-$* , Phys. Rev. Lett. **103** (2009) 171801, arXiv: 0904.0770.
- [8] Belle collaboration, A. Abdesselam *et al.*, *Test of lepton flavor universality in $B \rightarrow K^* \ell^+ \ell^-$ decays at Belle*, arXiv: 1904.02440.
- [9] Belle collaboration, A. Abdesselam *et al.*, *Test of lepton flavor universality in $B \rightarrow K \ell^+ \ell^-$ decays*, arXiv: 1908.01848.
- [10] LHCb collaboration, R. Aaij *et al.*, *Search for lepton-universality violation in $B^+ \rightarrow K^+ \ell^+ \ell^-$ decays*, Phys. Rev. Lett. **122** (2019) 191801, arXiv: 1903.09252.
- [11] LHCb collaboration, R. Aaij *et al.*, *Test of lepton universality with $B^0 \rightarrow K^{*0} \ell^+ \ell^-$ decays*, JHEP **08** (2017) 055, arXiv: 1705.05802.
- [12] S. Descotes-Genon, L. Hofer, J. Matias, and J. Virto, *Global analysis of $b \rightarrow s \ell \ell$ anomalies*, JHEP **06** (2016) 092, arXiv: 1510.04239.
- [13] C. Bobeth, G. Hiller, and G. Piranishvili, *Angular distributions of $\bar{B} \rightarrow \bar{K} \ell \ell$ decays*, JHEP **12** (2007) 040, arXiv: 0709.4174.
- [14] B. Capdevila, S. Descotes-Genon, J. Matias, and J. Virto, *Assessing lepton-flavour non-universality from $B \rightarrow K^* \ell \ell$ angular analyses*, JHEP **10** (2016) 075, arXiv: 1605.03156.
- [15] B. Capdevila, S. Descotes-Genon, L. Hofer, and J. Matias, *Hadronic uncertainties in $B \rightarrow K^* \mu^+ \mu^-$: a state-of-the-art analysis*, JHEP **04** (2017) 016, arXiv: 1701.08672.

- [16] N. Serra, R. Silva Coutinho, and D. van Dyk, *Measuring the breaking of lepton flavour universality in $B \rightarrow K^* \ell^+ \ell^-$* , Phys. Rev. **D95** (2017) 035029, arXiv: 1610.08761.
- [17] D. van Dyk *et al.*, *EOS — A HEP program for flavor observables*, <https://eos.github.io>.
- [18] A. Bharucha, D. M. Straub, and R. Zwicky, *$B \rightarrow V \ell^+ \ell^-$ in the Standard Model from light-cone sum rules*, JHEP **08** (2016) 098, arXiv: 1503.05534.
- [19] D. M. Straub, *flavio: a python package for flavour and precision phenomenology in the Standard Model and beyond*, arXiv: 1810.08132.
- [20] W. Altmannshofer, C. Niehoff, P. Stangl, and D. M. Straub, *Status of the $B \rightarrow K^* \mu^+ \mu^-$ anomaly after Moriond 2017*, arXiv: 1703.09189.
- [21] S. Jäger and J. Martin Camalich, *Reassessing the discovery potential of the $B \rightarrow K^* \ell^+ \ell^-$ decays in the large-recoil region: SM challenges and BSM opportunities*, Phys. Rev. **D93** (2016) 014028, arXiv: 1412.3183.
- [22] LHCb collaboration, R. Aaij *et al.*, *Angular moments of the decay $\Lambda_b^0 \rightarrow \Lambda \mu^+ \mu^-$* , JHEP **09** (2018) 146, arXiv: 1808.00264.
- [23] LHCb collaboration, R. Aaij *et al.*, *Observation of the decay $\Lambda_b^0 \rightarrow p K^- \mu^+ \mu^-$ and search for CP violation*, JHEP **06** (2017) 108, arXiv: 1703.00256.
- [24] J. Fuentes-Martín, G. Isidori, J. Pagès, and K. Yamamoto, *With or without $U(2)$? Probing non-standard flavor and helicity structures in semileptonic B decays*, arXiv: 1909.02519.
- [25] G. Hiller and M. Schmaltz, *Diagnosing lepton-nonuniversality in $b \rightarrow s \ell \ell$* , JHEP **02** (2015) 055, arXiv: 1411.4773.
- [26] LHCb collaboration, R. Aaij *et al.*, *Observation of $J/\psi p$ resonances consistent with pentaquark states in $\Lambda_b^0 \rightarrow J/\psi p K^-$ decays*, Phys. Rev. Lett. **115** (2015) 072001, arXiv: 1507.03414.
- [27] Particle Data Group, M. Tanabashi *et al.*, *Review of particle physics*, Phys. Rev. **D98** (2018) 030001.
- [28] L. Mott and W. Roberts, *Rare dileptonic decays of Λ_b^0 in a quark model*, Int. J. Mod. Phys. **A27** (2012) 1250016, arXiv: 1108.6129.
- [29] S. Descotes-Genon and M. Novoa Brunet, *Angular analysis of the rare decay $\Lambda_b^0 \rightarrow \Lambda(1520)(\rightarrow NK) \ell^+ \ell^-$* , JHEP **06** (2019) 136, arXiv: 1903.00448.
- [30] LHCb collaboration, A. A. Alves Jr. *et al.*, *The LHCb detector at the LHC*, JINST **3** (2008) S08005.
- [31] LHCb collaboration, R. Aaij *et al.*, *LHCb detector performance*, Int. J. Mod. Phys. **A30** (2015) 1530022, arXiv: 1412.6352.
- [32] V. V. Gligorov and M. Williams, *Efficient, reliable and fast high-level triggering using a bonsai boosted decision tree*, JINST **8** (2013) P02013, arXiv: 1210.6861.

- [33] T. Sjöstrand, S. Mrenna, and P. Skands, *PYTHIA 6.4 physics and manual*, JHEP **05** (2006) 026, arXiv: hep-ph/0603175; T. Sjöstrand, S. Mrenna, and P. Skands, *A brief introduction to PYTHIA 8.1*, Comput. Phys. Commun. **178** (2008) 852, arXiv: 0710.3820.
- [34] I. Belyaev *et al.*, *Handling of the generation of primary events in Gauss, the LHCb simulation framework*, J. Phys. Conf. Ser. **331** (2011) 032047.
- [35] D. J. Lange, *The EvtGen particle decay simulation package*, Nucl. Instrum. Meth. **A462** (2001) 152.
- [36] P. Golonka and Z. Was, *PHOTOS Monte Carlo: A precision tool for QED corrections in Z and W decays*, Eur. Phys. J. **C45** (2006) 97, arXiv: hep-ph/0506026.
- [37] Geant4 collaboration, J. Allison *et al.*, *Geant4 developments and applications*, IEEE Trans. Nucl. Sci. **53** (2006) 270; Geant4 collaboration, S. Agostinelli *et al.*, *Geant4: A simulation toolkit*, Nucl. Instrum. Meth. **A506** (2003) 250.
- [38] M. Clemencic *et al.*, *The LHCb simulation application, Gauss: Design, evolution and experience*, J. Phys. Conf. Ser. **331** (2011) 032023.
- [39] L. Breiman, J. H. Friedman, R. A. Olshen, and C. J. Stone, *Classification and regression trees*, Wadsworth international group, Belmont, California, USA, 1984.
- [40] P. J. Huber, *Robust estimation of a location parameter*, The Annals of Mathematical Statistics **35** (1964) 73.
- [41] A. Blum *et al.*, *Beating the hold-out: Bounds for k-fold and progressive cross-validation, in Proceedings of the Twelfth Annual Conference on Computational Learning Theory, in COLT*, 203, 1999.
- [42] R. Aaij *et al.*, *Selection and processing of calibration samples to measure the particle identification performance of the LHCb experiment in Run 2*, Eur. Phys. J. Tech. Instr. **6** (2018) 1, arXiv: 1803.00824.
- [43] T. Skwarnicki, *A study of the radiative cascade transitions between the Upsilon-prime and Upsilon resonances*, PhD thesis, Institute of Nuclear Physics, Krakow, 1986, DESY-F31-86-02.
- [44] K. S. Cranmer, *Kernel estimation in high-energy physics*, Comput. Phys. Commun. **136** (2001) 198, arXiv: hep-ex/0011057.
- [45] P. Ball and R. Zwicky, *$B_{d,s} \rightarrow \rho, \omega, K^*, \phi$ decay form-factors from light-cone sum rules revisited*, Phys. Rev. **D71** (2005) 014029, arXiv: hep-ph/0412079.
- [46] LHCb collaboration, R. Aaij *et al.*, *Study of the productions of Λ_b^0 and \bar{B}^0 hadrons in pp collisions and first measurement of the $\Lambda_b^0 \rightarrow J/\psi p K^-$ branching fraction*, Chin. Phys. C **40** (2016) 011001, arXiv: 1509.00292.

LHCb collaboration

R. Aaij³¹, C. Abellán Beteta⁴⁹, T. Ackernley⁵⁹, B. Adeva⁴⁵, M. Adinolfi⁵³, H. Afsharnia⁹, C.A. Aidala⁸⁰, S. Aiola²⁵, Z. Ajaltouni⁹, S. Akar⁶⁶, P. Albicocco²², J. Albrecht¹⁴, F. Alessio⁴⁷, M. Alexander⁵⁸, A. Alfonso Alberó⁴⁴, G. Alkhazov³⁷, P. Alvarez Cartelle⁶⁰, A.A. Alves Jr⁴⁵, S. Amato², Y. Amhis¹¹, L. An²¹, L. Anderlini²¹, G. Andreassi⁴⁸, M. Andreotti²⁰, F. Archilli¹⁶, J. Arnau Romeu¹⁰, A. Artamonov⁴³, M. Artuso⁶⁷, K. Arzymatov⁴¹, E. Aslanides¹⁰, M. Atzeni⁴⁹, B. Audurier²⁶, S. Bachmann¹⁶, J.J. Back⁵⁵, S. Baker⁶⁰, V. Balagura^{11,b}, W. Baldini^{20,47}, A. Baranov⁴¹, R.J. Barlow⁶¹, S. Barsuk¹¹, W. Barter⁶⁰, M. Bartolini^{23,47,h}, F. Baryshnikov⁷⁷, G. Bassi²⁸, V. Batozskaya³⁵, B. Batsukh⁶⁷, A. Battig¹⁴, A. Bay⁴⁸, M. Becker¹⁴, F. Bedeschi²⁸, I. Bediaga¹, A. Beiter⁶⁷, L.J. Bel³¹, V. Belavin⁴¹, S. Belin²⁶, N. Belyi⁵, V. Bellec⁴⁸, K. Belous⁴³, I. Belyaev³⁸, G. Bencivenni²², E. Ben-Haim¹², S. Benson³¹, S. Beranek¹³, A. Berezhnoy³⁹, R. Bernet⁴⁹, D. Berninghoff¹⁶, H.C. Bernstein⁶⁷, C. Bertella⁴⁷, E. Bertholet¹², A. Bertolin²⁷, C. Betancourt⁴⁹, F. Betti^{19,e}, M.O. Bettler⁵⁴, I.a. Bezshyiko⁴⁹, S. Bhasin⁵³, J. Bhom³³, M.S. Bieker¹⁴, S. Bifani⁵², P. Billoir¹², A. Bizzeti^{21,u}, M. Bjørn⁶², M.P. Blago⁴⁷, T. Blake⁵⁵, F. Blanc⁴⁸, S. Blusk⁶⁷, D. Bobulska⁵⁸, V. Bocci³⁰, O. Boente Garcia⁴⁵, T. Boettcher⁶³, A. Boldyrev⁷⁸, A. Bondar^{42,x}, N. Bondar³⁷, S. Borghi^{61,47}, M. Borisyak⁴¹, M. Borsato¹⁶, J.T. Borsuk³³, T.J.V. Bowcock⁵⁹, C. Bozzi²⁰, M.J. Bradley⁶⁰, S. Braun¹⁶, A. Brea Rodriguez⁴⁵, M. Brodski⁴⁷, J. Brodzicka³³, A. Brossa Gonzalo⁵⁵, D. Brundu²⁶, E. Buchanan⁵³, A. Buonauro⁴⁹, C. Burr⁴⁷, A. Bursche²⁶, J.S. Butter³¹, J. Buytaert⁴⁷, W. Byczynski⁴⁷, S. Cadeddu²⁶, H. Cai⁷², R. Calabrese^{20,g}, L. Calero Diaz²², S. Cali²², R. Calladine⁵², M. Calvi^{24,i}, M. Calvo Gomez^{44,m}, P. Camargo Magalhaes⁵³, A. Camboni^{44,m}, P. Campana²², D.H. Campora Perez³¹, L. Capriotti^{19,e}, A. Carbone^{19,e}, G. Carboni²⁹, R. Cardinale^{23,h}, A. Cardini²⁶, P. Carniti^{24,i}, K. Carvalho Akiba³¹, A. Casais Vidal⁴⁵, G. Casse⁵⁹, M. Cattaneo⁴⁷, G. Cavallero⁴⁷, S. Celani⁴⁸, R. Cenci^{28,p}, J. Cerasoli¹⁰, M.G. Chapman⁵³, M. Charles^{12,47}, Ph. Charpentier⁴⁷, G. Chatzikonstantinidis⁵², M. Chefdeville⁸, V. Chekalina⁴¹, C. Chen³, S. Chen²⁶, A. Chernov³³, S.-G. Chitic⁴⁷, V. Chobanova⁴⁵, M. Chruszcz³³, A. Chubykin³⁷, P. Ciambriano²², M.F. Cicala⁵⁵, X. Cid Vidal⁴⁵, G. Ciezarek⁴⁷, F. Cindolo¹⁹, P.E.L. Clarke⁵⁷, M. Clemencic⁴⁷, H.V. Cliff⁵⁴, J. Closier⁴⁷, J.L. Cobbledick⁶¹, V. Coco⁴⁷, J.A.B. Coelho¹¹, J. Cogan¹⁰, E. Cogneras⁹, L. Cojocariu³⁶, P. Collins⁴⁷, T. Colombo⁴⁷, A. Comerma-Montells¹⁶, A. Contu²⁶, N. Cooke⁵², G. Coombs⁵⁸, S. Coquereau⁴⁴, G. Corti⁴⁷, C.M. Costa Sobral⁵⁵, B. Couturier⁴⁷, D.C. Craik⁶³, J. Crkowska⁶⁶, A. Crocombe⁵⁵, M. Cruz Torres^{1,ab}, R. Currie⁵⁷, C.L. Da Silva⁶⁶, E. Dall'Occo¹⁴, J. Dalseno^{45,53}, C. D'Ambrosio⁴⁷, A. Danilina³⁸, P. d'Argent¹⁶, A. Davis⁶¹, O. De Aguiar Francisco⁴⁷, K. De Bruyn⁴⁷, S. De Capua⁶¹, M. De Cian⁴⁸, J.M. De Miranda¹, L. De Paula², M. De Serio^{18,d}, P. De Simone²², J.A. de Vries³¹, C.T. Dean⁶⁶, W. Dean⁸⁰, D. Decamp⁸, L. Del Buono¹², B. Delaney⁵⁴, H.-P. Dembinski¹⁵, M. Demmer¹⁴, A. Dendek³⁴, V. Denysenko⁴⁹, D. Derkach⁷⁸, O. Deschamps⁹, F. Desse¹¹, F. Dettori^{26,f}, B. Dey⁷, A. Di Canto⁴⁷, P. Di Nezza²², S. Didenko⁷⁷, H. Dijkstra⁴⁷, V. Dobishuk⁵¹, F. Dordei²⁶, M. Dorigo^{28,y}, A.C. dos Reis¹, L. Douglas⁵⁸, A. Dovbnya⁵⁰, K. Dreimanis⁵⁹, M.W. Dudek³³, L. Dufour⁴⁷, G. Dujany¹², P. Durante⁴⁷, J.M. Durham⁶⁶, D. Dutta⁶¹, M. Dziewiecki¹⁶, A. Dziurda³³, A. Dzyuba³⁷, S. Easo⁵⁶, U. Egede⁶⁹, V. Egorychev³⁸, S. Eidelman^{42,x}, S. Eisenhardt⁵⁷, R. Ekelhof¹⁴, S. Ek-In⁴⁸, L. Eklund⁵⁸, S. Ely⁶⁷, A. Ene³⁶, E. Eppe⁶⁶, S. Escher¹³, S. Esen³¹, T. Evans⁴⁷, A. Falabella¹⁹, J. Fan³, N. Farley⁵², S. Farry⁵⁹, D. Fazzini¹¹, P. Fedin³⁸, M. Féo⁴⁷, P. Fernandez Declara⁴⁷, A. Fernandez Prieto⁴⁵, F. Ferrari^{19,e}, L. Ferreira Lopes⁴⁸, F. Ferreira Rodrigues², S. Ferreres Sole³¹, M. Ferrillo⁴⁹, M. Ferro-Luzzi⁴⁷, S. Filippov⁴⁰, R.A. Fini¹⁸, M. Fiorini^{20,g}, M. Firlej³⁴, K.M. Fischer⁶², C. Fitzpatrick⁴⁷, T. Fiutowski³⁴, F. Fleuret^{11,b}, M. Fontana⁴⁷, F. Fontanelli^{23,h}, R. Forty⁴⁷, V. Franco Lima⁵⁹, M. Franco Sevilla⁶⁵, M. Frank⁴⁷, C. Frei⁴⁷, D.A. Friday⁵⁸, J. Fu^{25,q}, M. Fuehring¹⁴, W. Funk⁴⁷, E. Gabriel⁵⁷, A. Gallas Torreira⁴⁵, D. Galli^{19,e}, S. Gallorini²⁷, S. Gambetta⁵⁷, Y. Gan³, M. Gandelman², P. Gandini²⁵, Y. Gao⁴, L.M. Garcia Martin⁴⁶, J. García Pardiñas⁴⁹,

B. Garcia Plana⁴⁵, F.A. Garcia Rosales¹¹, J. Garra Tico⁵⁴, L. Garrido⁴⁴, D. Gascon⁴⁴,
 C. Gaspar⁴⁷, D. Gerick¹⁶, E. Gersabeck⁶¹, M. Gersabeck⁶¹, T. Gershon⁵⁵, D. Gerstel¹⁰,
 Ph. Ghez⁸, V. Gibson⁵⁴, A. Gioventù⁴⁵, O.G. Girard⁴⁸, P. Gironella Gironell⁴⁴, L. Giubega³⁶,
 C. Giugliano²⁰, K. Gizdov⁵⁷, V.V. Gligorov¹², C. Göbel⁷⁰, D. Golubkov³⁸, A. Golutvin^{60,77},
 A. Gomes^{1,a}, P. Gorbounov^{38,6}, I.V. Gorelov³⁹, C. Gotti^{24,i}, E. Govorkova³¹, J.P. Grabowski¹⁶,
 R. Graciani Diaz⁴⁴, T. Grammatico¹², L.A. Granado Cardoso⁴⁷, E. Graugés⁴⁴, E. Graverini⁴⁸,
 G. Graziani²¹, A. Grecu³⁶, R. Greim³¹, P. Griffith²⁰, L. Grillo⁶¹, L. Gruber⁴⁷,
 B.R. Gruberg Cazon⁶², C. Gu³, E. Gushchin⁴⁰, A. Guth¹³, Yu. Guz^{43,47}, T. Gys⁴⁷, P.
 A. Gnther¹⁶, T. Hadavizadeh⁶², G. Haefeli⁴⁸, C. Haen⁴⁷, S.C. Haines⁵⁴, P.M. Hamilton⁶⁵,
 Q. Han⁷, X. Han¹⁶, T.H. Hancock⁶², S. Hansmann-Menzemer¹⁶, N. Harnew⁶², T. Harrison⁵⁹,
 R. Hart³¹, C. Hasse⁴⁷, M. Hatch⁴⁷, J. He⁵, M. Hecker⁶⁰, K. Heijhoff³¹, K. Heinicke¹⁴,
 A. Heister¹⁴, A.M. Hennequin⁴⁷, K. Hennessy⁵⁹, L. Henry⁴⁶, J. Heuel¹³, A. Hicheur⁶⁸, D. Hill⁶²,
 M. Hilton⁶¹, P.H. Hopchev⁴⁸, J. Hu¹⁶, W. Hu⁷, W. Huang⁵, W. Hulsbergen³¹, T. Humair⁶⁰,
 R.J. Hunter⁵⁵, M. Hushchyn⁷⁸, D. Hutchcroft⁵⁹, D. Hynds³¹, P. Ibis¹⁴, M. Idzik³⁴, P. Ilten⁵²,
 A. Inglese³⁷, A. Inyakin⁴³, K. Ivshin³⁷, R. Jacobsson⁴⁷, S. Jakobsen⁴⁷, E. Jans³¹, B.K. Jashal⁴⁶,
 A. Jawahery⁶⁵, V. Jevtic¹⁴, F. Jiang³, M. John⁶², D. Johnson⁴⁷, C.R. Jones⁵⁴, B. Jost⁴⁷,
 N. Jurik⁶², S. Kandybei⁵⁰, M. Karacson⁴⁷, J.M. Kariuki⁵³, N. Kazeev⁷⁸, M. Kecke¹⁶,
 F. Keizer^{54,47}, M. Kelsey⁶⁷, M. Kenzie⁵⁵, T. Ketel³², B. Khanji⁴⁷, A. Kharisova⁷⁹, K.E. Kim⁶⁷,
 T. Kirn¹³, V.S. Kirsebom⁴⁸, S. Klaver²², K. Klimaszewski³⁵, S. Koliiev⁵¹, A. Kondybayeva⁷⁷,
 A. Konoplyannikov³⁸, P. Kopciewicz³⁴, R. Kopečna¹⁶, P. Koppenburg³¹, I. Kostiuk^{31,51},
 O. Kot⁵¹, S. Kotriakhova³⁷, L. Kravchuk⁴⁰, R.D. Krawczyk⁴⁷, M. Kreps⁵⁵, F. Kress⁶⁰,
 S. Kretschmar¹³, P. Krokovny^{42,x}, W. Krupa³⁴, W. Krzemien³⁵, W. Kucewicz^{33,l},
 M. Kucharczyk³³, V. Kudryavtsev^{42,x}, H.S. Kuindersma³¹, G.J. Kunde⁶⁶, T. Kvaratskheliya³⁸,
 D. Lacarrere⁴⁷, G. Lafferty⁶¹, A. Lai²⁶, D. Lancierini⁴⁹, J.J. Lane⁶¹, G. Lanfranchi²²,
 C. Langenbruch¹³, O. Lantwin⁴⁹, T. Latham⁵⁵, F. Lazzari^{28,v}, C. Lazzeroni⁵², R. Le Gac¹⁰,
 R. Lefèvre⁹, A. Leflat³⁹, O. Leroy¹⁰, T. Lesiak³³, B. Leverington¹⁶, H. Li⁷¹, X. Li⁶⁶, Y. Li⁶,
 Z. Li⁶⁷, X. Liang⁶⁷, R. Lindner⁴⁷, V. Lisovskyi¹⁴, G. Liu⁷¹, X. Liu³, D. Loh⁵⁵, A. Loi²⁶,
 J. Lomba Castro⁴⁵, I. Longstaff⁵⁸, J.H. Lopes², G. Loustau⁴⁹, G.H. Lovell⁵⁴, Y. Lu⁶,
 D. Lucchesi^{27,o}, M. Lucio Martinez³¹, Y. Luo³, A. Lupato²⁷, E. Luppi^{20,g}, O. Lupton⁵⁵,
 A. Lusiani^{28,t}, X. Lyu⁵, S. Maccolini^{19,e}, F. Machefer¹¹, F. Maciuc³⁶, V. Macko⁴⁸,
 P. Mackowiak¹⁴, S. Maddrell-Mander⁵³, L.R. Madhan Mohan⁵³, O. Maev^{37,47}, A. Maevskiy⁷⁸,
 D. Maisuzenko³⁷, M.W. Majewski³⁴, S. Malde⁶², B. Malecki⁴⁷, A. Malinin⁷⁶, T. Maltsev^{42,x},
 H. Malygina¹⁶, G. Manca^{26,f}, G. Mancinelli¹⁰, R. Manera Escalero⁴⁴, D. Manuzzi^{19,e},
 D. Marangotto^{25,q}, J. Maratas^{9,w}, J.F. Marchand⁸, U. Marconi¹⁹, S. Mariani²¹,
 C. Marin Benito¹¹, M. Marinangeli⁴⁸, P. Marino⁴⁸, J. Marks¹⁶, P.J. Marshall⁵⁹, G. Martellotti³⁰,
 L. Martinazzoli⁴⁷, M. Martinelli^{24,i}, D. Martinez Santos⁴⁵, F. Martinez Vidal⁴⁶, A. Massafferri¹,
 M. Materok¹³, R. Matev⁴⁷, A. Mathad⁴⁹, Z. Mathe⁴⁷, V. Matiunin³⁸, C. Matteuzzi²⁴,
 K.R. Mattioli⁸⁰, A. Mauri⁴⁹, E. Maurice^{11,b}, M. McCann⁶⁰, L. McConnell¹⁷, A. McNab⁶¹,
 R. McNulty¹⁷, J.V. Mead⁵⁹, B. Meadows⁶⁴, C. Meaux¹⁰, G. Meier¹⁴, N. Meinert⁷⁴,
 D. Melnychuk³⁵, S. Meloni^{24,i}, M. Merk³¹, A. Merli²⁵, M. Mikhasenko⁴⁷, D.A. Milanese⁷³,
 E. Millard⁵⁵, M.-N. Minard⁸, O. Mineev³⁸, L. Minzoni^{20,g}, S.E. Mitchell⁵⁷, B. Mitreska⁶¹,
 D.S. Mitzel⁴⁷, A. Mödden¹⁴, A. Mogini¹², R.D. Moise⁶⁰, T. Mombächer¹⁴, I.A. Monroy⁷³,
 S. Monteil⁹, M. Morandin²⁷, G. Morello²², M.J. Morello^{28,t}, J. Moron³⁴, A.B. Morris¹⁰,
 A.G. Morris⁵⁵, R. Mountain⁶⁷, H. Mu³, F. Muheim⁵⁷, M. Mukherjee⁷, M. Mulder³¹,
 D. Müller⁴⁷, K. Müller⁴⁹, V. Müller¹⁴, C.H. Murphy⁶², D. Murray⁶¹, P. Muzzetto²⁶, P. Naik⁵³,
 T. Nakada⁴⁸, R. Nandakumar⁵⁶, A. Nandi⁶², T. Nanut⁴⁸, I. Nasteva², M. Needham⁵⁷,
 N. Neri^{25,q}, S. Neubert¹⁶, N. Neufeld⁴⁷, R. Newcombe⁶⁰, T.D. Nguyen⁴⁸, C. Nguyen-Mau^{48,n},
 E.M. Niel¹¹, S. Nieswand¹³, N. Nikitin³⁹, N.S. Nolte⁴⁷, C. Nunez⁸⁰, A. Oblakowska-Mucha³⁴,
 V. Obraztsov⁴³, S. Ogilvy⁵⁸, D.P. O’Hanlon¹⁹, R. Oldeman^{26,f}, C.J.G. Onderwater⁷⁵, J.
 D. Osborn⁸⁰, A. Ossowska³³, J.M. Otalora Goicochea², T. Ovsiannikova³⁸, P. Owen⁴⁹,

Bibliography

- [1] M. Tanabashi et al. Review of Particle Physics. *Phys. Rev.*, D98(3):030001, 2018.
- [2] P. A. R. Ade et al. Planck 2015 results. XIII. Cosmological parameters. *Astron. Astrophys.*, 594:A13, 2016.
- [3] Georges Aad et al. Measurements of the Higgs boson production and decay rates and constraints on its couplings from a combined ATLAS and CMS analysis of the LHC pp collision data at $\sqrt{s} = 7$ and 8 TeV. *JHEP*, 08:045, 2016.
- [4] Javier Fuentes-Martín, Gino Isidori, Julie Pagès, and Kei Yamamoto. With or without U(2)? Probing non-standard flavor and helicity structures in semileptonic B decays. 2019.
- [5] Damir Bečirević, Ilja Doršner, Svjetlana Fajfer, Nejc Košnik, Darius A. Faroughy, and Olcyr Sumensari. Scalar leptoquarks from grand unified theories to accommodate the B -physics anomalies. *Phys. Rev.*, D98(5):055003, 2018.
- [6] Antonio Pich. Effective field theory: Course. In *Probing the standard model of particle interactions. Proceedings, Summer School in Theoretical Physics, NATO Advanced Study Institute, 68th session, Les Houches, France, July 28-September 5, 1997. Pt. 1, 2*, pages 949–1049, 1998.
- [7] Matthias Neubert. Heavy quark effective theory. *Subnucl. Ser.*, 34:98–165, 1997.
- [8] Andrzej J. Buras. Weak Hamiltonian, CP violation and rare decays. In *Probing the standard model of particle interactions. Proceedings, Summer School in Theoretical Physics, NATO Advanced Study Institute, 68th session, Les Houches, France, July 28-September 5, 1997. Pt. 1, 2*, pages 281–539, 1998.
- [9] Luca Silvestrini. Effective Theories for Quark Flavour Physics. In *Les Houches summer school: EFT in Particle Physics and Cosmology Les Houches, Chamonix Valley, France, July 3-28, 2017*, 2019.
- [10] M. Tanabashi et al. [Review of particle physics](#). *Phys. Rev.*, D98:030001, 2018.
- [11] Pietro Colangelo and Alexander Khodjamirian. QCD sum rules, a modern perspective. pages 1495–1576, 2000.
- [12] Nilmani Mathur, Randy Lewis, and R.M. Woloshyn. Charmed and bottom baryons from lattice NRQCD. *Phys. Rev.*, D66:014502, 2002.
- [13] M. Karliner, B. Keren-Zur, H.J. Lipkin, and J.L. Rosner. The quark model and b baryons. *Annals Phys.*, 342:2–15, 2009.

- [14] Elizabeth Ellen Jenkins. Model-independent bottom baryon mass predictions in the $1/N_c$ expansion. *Phys. Rev.*, D77:034012, 2008.
- [15] D. Ebert, R.N. Faustov, and V.O. Galkin. Masses of heavy baryons in the relativistic quark model. *Phys. Rev.*, D72:034026, 2005.
- [16] Xiang Liu, Hua-Xing Chen, Yan-Rui Liu, Atsushi Hosaka, and Shi-Lin Zhu. Bottom baryons. *Phys. Rev.*, D77:014031, 2008.
- [17] Jian-Rong Zhang and Ming-Qiu Huang. Heavy baryon spectroscopy in QCD. *Phys. Rev.*, D78:094015, 2008.
- [18] Randy Lewis and R.M. Woloshyn. Bottom baryons from a dynamical lattice QCD simulation. *Phys. Rev.*, D79:014502, 2009.
- [19] Alexander Lenz. Lifetimes and heavy quark expansion. *Int. J. Mod. Phys.*, A30(10):1543005, 2015. [63(2014)].
- [20] Ikaros I. Y. Bigi. The QCD perspective on lifetimes of heavy flavor hadrons. 1995.
- [21] Hai-Yang Cheng. A Phenomenological analysis of heavy hadron lifetimes. *Phys. Rev.*, D56:2783–2798, 1997.
- [22] Toshiaki Ito, Masahisa Matsuda, and Yoshimitsu Matsui. New possibility of solving the problem of lifetime ratio $\tau(\Lambda_b)/\tau(B_d)$. *Prog. Theor. Phys.*, 99:271–280, 1998.
- [23] C. Aubin, C. Bernard, C. DeTar, M. DiPierro, A. El-Khadra, Steven Gottlieb, E. B. Gregory, U. M. Heller, J. Hetrick, A. S. Kronfeld, P. B. Mackenzie, D. Menscher, M. Nobes, M. Okamoto, M. B. Oktay, J. Osborn, J. Simone, R. Sugar, D. Toussaint, and H. D. Trottier. Semileptonic decays of d mesons in three-flavor lattice qcd. *Phys. Rev. Lett.*, 94:011601, Jan 2005.
- [24] Christoph Bobeth, Mikolaj Misiak, and Jorg Urban. Photonic penguins at two loops and m_t dependence of $BR[B \rightarrow X_s l^+ l^-]$. *Nucl. Phys.*, B574:291–330, 2000.
- [25] Marzia Bordone, Gino Isidori, and Andrea Pattori. On the Standard Model predictions for R_K and R_{K^*} . *Eur. Phys. J.*, C76(8):440, 2016.
- [26] Yasmine Sara Amhis et al. Averages of b -hadron, c -hadron, and τ -lepton properties as of 2018. 2019.
- [27] Roel Aaij et al. Search for lepton-universality violation in $B^+ \rightarrow K^+ \ell^+ \ell^-$ decays. *Phys. Rev. Lett.*, 122(19):191801, 2019.
- [28] R. Aaij et al. Test of lepton universality with $B^0 \rightarrow K^{*0} \ell^+ \ell^-$ decays. 2017.
- [29] Roel Aaij et al. Angular analysis and differential branching fraction of the decay $B_s^0 \rightarrow \phi \mu^+ \mu^-$. *JHEP*, 09:179, 2015.
- [30] R. Aaij et al. Differential branching fractions and isospin asymmetries of $B \rightarrow K^{(*)} \mu^+ \mu^-$ decays. *JHEP*, 06:133, 2014.
- [31] Marco Ciuchini, Antonio M. Coutinho, Marco Fedele, Enrico Franco, Ayan Paul, Luca Silvestrini, and Mauro Valli. Hadronic uncertainties in semileptonic $B \rightarrow K^* \mu^+ \mu^-$ decays. *POs*, BEAUTY2018:044, 2018.

- [32] Jason Aebischer, Wolfgang Altmannshofer, Diego Guadagnoli, M eril Reboud, Peter Stangl, and David M. Straub. B-decay discrepancies after Moriond 2019. 2019.
- [33] Luca Di Luzio, Admir Greljo, and Marco Nardecchia. Gauge leptoquark as the origin of B-physics anomalies. *Phys. Rev.*, D96(11):115011, 2017.
- [34] Lorenzo Calibbi, Andreas Crivellin, and Tianjun Li. Model of vector leptoquarks in view of the B-physics anomalies. *Phys. Rev.*, D98(11):115002, 2018.
- [35] Marzia Bordone, Claudia Cornella, Javier Fuentes-Martin, and Gino Isidori. A three-site gauge model for flavor hierarchies and flavor anomalies. *Phys. Lett.*, B779:317–323, 2018.
- [36] Riccardo Barbieri and Andrea Tesi. B-decay anomalies in Pati-Salam SU(4). *Eur. Phys. J.*, C78(3):193, 2018.
- [37] Andreas Crivellin, Dario M uller, and Toshihiko Ota. Simultaneous explanation of $R_{D^{(*)}}$ and $b \rightarrow s\mu^+\mu^-$: the last scalar leptoquarks standing. *JHEP*, 09:040, 2017.
- [38] Dario Buttazzo, Admir Greljo, Gino Isidori, and David Marzocca. B-physics anomalies: a guide to combined explanations. *JHEP*, 11:044, 2017.
- [39] David Marzocca. Addressing the B-physics anomalies in a fundamental Composite Higgs Model. *JHEP*, 07:121, 2018.
- [40] A. Angelescu, Damir Be cirevi c, D. A. Faroughy, and O. Sumensari. Closing the window on single leptoquark solutions to the B-physics anomalies. *JHEP*, 10:183, 2018.
- [41] Miguel Crispim Romao, Stephen F. King, and George K. Leontaris. Non-universal Z' from fluxed GUTs. *Phys. Lett.*, B782:353–361, 2018.
- [42] Damir Becirevic and Olcyr Sumensari. A leptoquark model to accommodate $R_K^{\text{exp}} < R_K^{\text{SM}}$ and $R_{K^*}^{\text{exp}} < R_{K^*}^{\text{SM}}$. 2017.
- [43] Pere Arnau, Andreas Crivellin, Marco Fedele, and Federico Mescia. Generic loop effects of new scalars and fermions in $b \rightarrow s\ell^+\ell^-$ and a vector-like 4th generation. *JHEP*, 06:118, 2019.
- [44] Roel Aaij et al. LHCb Detector Performance. *Int. J. Mod. Phys.*, A30(07):1530022, 2015.
- [45] Aaij, Roel and others. LHCb Detector Performance. *Int. J. Mod. Phys. A*, 30(LHCB-DP-2014-002. CERN-PH-EP-2014-290. LHCB-DP-2014-002. CERN-LHCB-DP-2014-002):1530022. 73 p, Dec 2014.
- [46] I Bediaga et al. Framework TDR for the LHCb Upgrade: Technical Design Report. Technical Report CERN-LHCC-2012-007. LHCb-TDR-12, Apr 2012.
- [47] LHCb Collaboration. LHCb VELO Upgrade Technical Design Report. Technical Report CERN-LHCC-2013-021. LHCB-TDR-013, Nov 2013.
- [48] Renato Quagliani. Study of double charm B decays with the LHCb experiment at CERN and track reconstruction for the LHCb upgrade, Oct 2017. Presented 06 Oct 2017.
- [49] LHCb Collaboration. LHCb Tracker Upgrade Technical Design Report. Technical Report CERN-LHCC-2014-001. LHCB-TDR-015, Feb 2014.
- [50] S Amato et al. *LHCb calorimeters: Technical Design Report*. Technical Design Report LHCb. CERN, Geneva, 2000.

- [51] C. Albajar et al. First observation of the beauty baryon Λ_b in the decay channel $\Lambda_b \rightarrow J/\psi\Lambda$ at the CERN proton - anti-proton collider. *Phys. Lett.*, B273:540–548, 1991. [,249(1992)].
- [52] Roel Aaij et al. Measurement of b hadron fractions in 13 TeV pp collisions. *Phys. Rev.*, D100:031102, 2019.
- [53] R Aaij et al. Measurement of the Λ_b^0 , Ξ_b^- and Ω_b^- baryon masses. *Phys. Rev. Lett.*, 110(18):182001, 2013.
- [54] Marek Karliner, Boaz Keren-Zur, Harry J. Lipkin, and Jonathan L. Rosner. The Quark Model and b Baryons. *Annals Phys.*, 324:2–15, 2009.
- [55] Georges Aad et al. Measurement of the Λ_b^0 lifetime and mass in the ATLAS experiment. 2012.
- [56] T. Aaltonen et al. Observation of the Ω_b^- baryon and measurement of the properties of the Ξ_b^- and Ω_b^- baryons. *Phys. Rev.*, D80:072003, 2009.
- [57] D. Acosta et al. Measurement of b hadron masses in exclusive J/ψ decays with the CDF detector. *Phys. Rev. Lett.*, 96:202001, 2006.
- [58] V.M. Abazov et al. Observation of the doubly strange b baryon Ω_b^- . *Phys. Rev. Lett.*, 101:232002, 2008.
- [59] V.M. Abazov et al. Direct observation of the strange b baryon Ξ_b^- . *Phys. Rev. Lett.*, 99:052001, 2007.
- [60] J. Beringer et al. [Review of particle physics](#). *Phys. Rev.*, D86:010001, 2012.
- [61] Roel Aaij et al. Measurement of the mass and lifetime of the Ω_b^- baryon. *Phys. Rev.*, D93(9):092007, 2016.
- [62] Roel Aaij et al. First observation of excited Ω_b^- states. *Phys. Rev. Lett.*, 124(8):082002, 2020.
- [63] Roel Aaij et al. Measurements of the B^+ , B^0 , B_s^0 meson and Λ_b^0 baryon lifetimes. *JHEP*, 04:114, 2014.
- [64] Muriel Pivk and Francois R. Le Diberder. sPlot: a statistical tool to unfold data distributions. *Nucl.Instrum.Meth.*, A555:356–369, 2005.
- [65] Fabrizio Gabbiani, Andrei I. Onishchenko, and Alexey A. Petrov. Spectator effects and lifetimes of heavy hadrons. *Phys. Rev.*, D70:094031, 2004.
- [66] Guido Altarelli, G. Martinelli, S. Petrarca, and F. Rapuano. Failure of local duality in inclusive nonleptonic heavy flavor decays. *Phys. Lett.*, B382:409–414, 1996.
- [67] Tim Gershon. $\Delta\Gamma_d$: a forgotten null test of the standard model. *J.Phys.*, G38:015007, 2011.
- [68] Alexander Lenz and Ulrich Nierste. Theoretical update of $B_s - \bar{B}_s$ mixing. *JHEP*, 06:072, 2007.
- [69] Alexander Lenz and Ulrich Nierste. Numerical updates of lifetimes and mixing parameters of B mesons. 2011.
- [70] Roel Aaij et al. Test of lepton universality with $\Lambda_b^0 \rightarrow pK^- \ell^+ \ell^-$ decays. 2019.
- [71] Vitalii Lisovskyi. Study of rare b -baryon decays and test of lepton universality at LHCb, 2019. Presented 09 Sep 2019.

- [72] S. Schael et al. Precision electroweak measurements on the Z resonance. *Phys. Rept.*, 427:257–454, 2006.
- [73] Morad Aaboud et al. Precision measurement and interpretation of inclusive W^+ , W^- and Z/γ^* production cross sections with the ATLAS detector. *Eur. Phys. J.*, C77(6):367, 2017.
- [74] Simone Bifani, Sébastien Descotes-Genon, Antonio Romero Vidal, and Marie-Hélène Schune. Review of Lepton Universality tests in B decays. *J. Phys.*, G46(2):023001, 2019.
- [75] R. Aaij et al. Observation of the decay $\Lambda_b^0 \rightarrow pK^-\mu^+\mu^-$ a search for CP violation. *JHEP*, 06:1, 2017.
- [76] R. Aaij et al. Study of the productions of Λ_b^0 and \bar{B}^0 hadrons in pp collisions and first measurement of the $\Lambda_b^0 \rightarrow J/\psi pK^-$ branching fraction. *Chin. Phys. C*, 40:011001, 2016.
- [77] R. Aaij et al. Observation of $\Lambda_b^0 \rightarrow \psi(2S)pK^-$ and $\Lambda_b^0 \rightarrow J/\psi \pi^+\pi^-pK^-$ decays and a measurement of the Λ_b^0 baryon mass. *JHEP*, 05:132, 2016.
- [78] R. Aaij et al. Observation of $J/\psi p$ resonances consistent with pentaquark states in $\Lambda_b^0 \rightarrow J/\psi pK^-$ decays. *Phys. Rev. Lett.*, 115:072001, 2015.
- [79] Roel Aaij et al. Physics case for an LHCb Upgrade II - Opportunities in flavour physics, and beyond, in the HL-LHC era. Technical Report LHCb-PUB-2018-009. LHCC-G-171, CERN, Geneva, Aug 2018. ISBN 978-92-9083-494-6.
- [80] F. Pedregosa, G. Varoquaux, A. Gramfort, V. Michel, B. Thirion, O. Grisel, M. Blondel, P. Prettenhofer, R. Weiss, V. Dubourg, J. Vanderplas, A. Passos, D. Cournapeau, M. Brucher, M. Perrot, and E. Duchesnay. Scikit-learn: Machine learning in Python. *Journal of Machine Learning Research*, 12:2825–2830, 2011.
- [81] David M. Straub. flavio: a python package for flavour and precision phenomenology in the Standard Model and beyond. 2018.

Acknowledgements

from village import *